

NORTHWESTERN UNIVERSITY

Nonlocal Coherence in Normal Metal-Superconductor Nanostructures

A DISSERTATION

SUBMITTED TO THE GRADUATE SCHOOL
IN PARTIAL FULFILLMENT OF THE REQUIREMENTS

for the degree

DOCTOR OF PHILOSOPHY

Field of Physics & Astronomy

By

Paul Cadden-Zimansky

EVANSTON, ILLINOIS

December 2008

© Copyright by Paul Cadden-Zimansky 2008

All Rights Reserved

ABSTRACT

Nonlocal Coherence in Normal Metal-Superconductor Nanostructures

Paul Cadden-Zimansky

One of the central features of the now half-century old theory of the microscopic origins of superconductivity in elemental materials is the correlations between pairs of electrons with opposite spin and momentum. The constituent electrons of these Cooper pairs have the unusual property that their mean spatial separation is much larger than atomic length scales, extending hundreds of nanometers in some materials. The central question motivating this thesis is whether one can see effects of these electronic correlations by placing normal metal probes on a superconductor within this length scale of each other. In particular we search for empirical evidence of two predicted processes, crossed Andreev reflection and elastic cotunneling, in which the Cooper pairs in a superconductor coherently couple electrons in two normal metal probes. We present results showing that such coupling does indeed occur and its observed behavior is consistent with the predicted processes. Specifically, we show that signals can be sent between normal metal probes which are nonlocal, phase coherent, and decay on the order of the Cooper pair correlation length.

In addition, our data give new insights into the interaction between normal electrons and Cooper pairs when they coexist in a normal metal.

Acknowledgements

This document owes its existence to the patient and persistent tutelage of Venkat Chandrasekhar, who has overseen not only my development as a physicist, but the development and construction of Northwestern's Mesoscopic Physics Lab into a playground for nanoscale investigations.

While the work described herein rests partially on the toils of all prior and present denizens of this Lab, two individuals deserve explicit commendation for the assistance they afforded me: Zhigang Jiang, who taught me all the basics of fabrication, refrigeration, and measurement, and answered my many queries with care and clarity; and Jian Wei, who counterbalanced my short-sighted ways with an organizational eye towards the needs of posterity and acted as an able interlocutor as we mutually explored the mysteries of coherent devices.

Gratitude is due to the sage Sam Bader who offered me a year's sanctuary at Argonne National Laboratory. My work there would not have been possible without assistance from the imperturbable Sam Jiang, the irrepressible Anand Bhattacharya, and the indispensable John Pearson.

My thanks to those members of the Northwestern Physics Department – Jim Sauls, Anupam Garg, and John Ketterson in particular – who showed great patience in entertaining an idle condensed matter question when I arrived unannounced at their office doors.

I'm indebted to Bill Halperin and his senior ultra-low temperature students, Hyungsoon Choi, John Davis, and Johannes Pollanen, for their cryo-knowledge, machining advice, and liberal tool-lending policies.

Funding for my research has been supplied by Northwestern University, the National Science Foundation, and the Department of Energy. I would particularly like to recognize President Henry Bienen, Dean Andrew Wachtel, Associate Dean Simon Greenwold, Pat Mann and Mary Pat Doyle of the graduate school, and the other Northwestern Presidential Fellows for their financial and intellectual support over the past two years.

Vicki Eckstein, Marsha Coffey, Lurleen Flores, Grant Darktower, and the rest of the Physics department staff past and present have been invaluable in helping me to navigate through graduate school life.

To my parents, whose union of the Platonic and Peripatetic is a testament to the possibility of wedding theory and experiment, I give my love and enduring respect.

Finally, to Carol Braun, for being the best.

Table of Contents

ABSTRACT	3
Acknowledgements	5
List of Tables	9
List of Figures	10
Chapter 1. Introduction	13
Chapter 2. Theoretical Background	16
2.1. Cooper's Pairs	16
2.2. BCS	20
2.3. Charge Imbalance	28
2.4. The Josephson Effect	31
2.5. Andreev Reflection	36
2.6. BTK	38
2.7. Green's Functions	41
Chapter 3. Crossed Andreev Reflection and Elastic Cotunneling	45
3.1. Early Theory	45
3.2. Prior Experimental Work	53
3.3. Recent Theory	59

Chapter 4. Experimental Fabrication and Measurement	65
4.1. Substrates	66
4.2. Photolithography	66
4.3. Electron Beam Lithography	71
4.4. Thermal Evaporation	81
4.5. Preparing Samples for Cooldown	83
4.6. Dilution Refrigerator	84
4.7. Measurement Set-up and Techniques	87
Chapter 5. Experimental Results	92
5.1. Charge Imbalance	92
5.2. Nonlocal Signals	98
5.3. Nonlocal Coherence	103
5.4. Thermoelectric Oscillations	121
5.5. Coexistence of Normal and Superconducting Current	128
Chapter 6. Conclusion and Future Directions	140
References	143

List of Tables

4.1	Typical E-Beam Exposure Parameters	79
-----	------------------------------------	----

List of Figures

2.1	BCS Occupation Probabilities	23
2.2	BCS Rearrangement of the Fermi Surface	25
2.3	BCS Energy Excitation Spectrum	26
2.4	Charge Imbalance	29
2.5	Andreev Reflection	37
2.6	BTK Transport Across a Normal Metal-Superconducting Interface	40
3.1	Crossed Andreev Reflection and Elastic Cotunneling	47
3.2	Calculated Nonlocal Conductance of Byers and Flatté	49
3.3	Beckmann <i>et. al.</i> Ferromagnet-Superconductor-Ferromagnet Experiment	55
3.4	Russo <i>et. al.</i> Tunnel Barrier Experiment	57
3.5	Mélin and Feinberg Nonlocal Conductance Predictions	60
3.6	Morten <i>et. al.</i> Circuit Theory Model of Nonlocal Conductance	62
4.1	Standard Photolithographic Pattern	67
4.2	Photo and Electron Beam Lithography Process	72
4.3	Center of an E-beam Patterned Photopad	76

		11
4.4	E-beam Lithography Overshoot	80
4.5	Filter and Feedthrough Box for the Oxford MX100 Dilution Refrigerator	85
4.6	Wiring for the Oxford MX100 Dilution Unit	86
4.7	Nuclear Orientation Thermometer Temperature Measurement	88
4.8	Sample Measurement Schematic	90
5.1	Charge Imbalance at a Ferromagnetic-Superconductor Interface	94
5.2	Normal Metal-Superconductor Cross	97
5.3	Normal Metal-Superconductor Nonlocal Sample	99
5.4	Differential Resistance Measurements of the Nonlocal Sample	101
5.5	Incoherent Nonlocal Sample	104
5.6	Local and Nonlocal Differential Resistance of the Incoherent Nonlocal Sample	105
5.7	Incoherent Nonlocal Sample Differential Resistance Scaling	107
5.8	Weak Localization Measurements of Au Wires	108
5.9	Single-Lead Nonlocal Coherence Sample and Measurement Configurations	110
5.10	Local Measurements of Single-Lead Nonlocal Coherence Sample	112
5.11	Nonlocal Oscillations in Single-Lead Nonlocal Coherence Sample	114
5.12	Decay of Nonlocal Coherent Signal	116
5.13	Local Measurements of Multiple-Lead Nonlocal Coherence Sample	117
5.14	Multiple-Lead Nonlocal Coherence Measurement Configuration	119

5.15	Thermoelectric Oscillations in the Multiple-Lead Nonlocal Coherence Sample	120
5.16	Alternate Measurement Configurations of the Multiple-Lead Nonlocal Coherence Sample	122
5.17	Amplitude of Corner Lead Thermoelectric Oscillations in the Multiple-Lead Nonlocal Coherence Sample	125
5.18	Temperature Dependence of a Superconductor-Normal Metal-Superconductor Wire	130
5.19	SNS Resistor Model	132
5.20	Critical Current Paradox	134
5.21	SNS IV Curves	136

CHAPTER 1

Introduction

A signature exhibit in demonstrating the peculiarity and power of quantum mechanics is the entangled quantum object, wherein two or more apparently spatially distinct entities are bound in a state that intertwines the probabilities of their individual behavior. The exploitation of this entanglement is at the heart of a number of recently developed subfields in physics – quantum computation, quantum information, quantum cryptography, etc. – with many proposed schemes for finding or creating entangled objects to control.

Perhaps the simplest entangled object, from a conceptual and pedagogical perspective, is two electrons with opposite magnetic spins bound in a singlet state. In addition to providing a toy model for a number of entangled processes, these objects can be created in abundance with very little effort. Many elements, when cooled to low enough temperatures, become superconducting, a transition which is now understood to be driven on the microscopic scale by the formation of bound pairs of electrons in a singlet state. An intriguing aspect of these pairs is that they can often have a very large spatial extent compared with atomic size scales. For some superconductors the mean separation between the constituent electrons is hundreds of nanometers. Since creating devices on this length scale is now routine using modern nanofabrication techniques, this thesis asks the following question: If two probes separated by this distance are placed on a superconductor, is it possible to observe effects between them governed by the properties of the bound pairs?

We shall not go so far as to demonstrate that we can use the electron pairs to produce effects indicative of quantum entanglement, but we will demonstrate two other effects that are signatures of quantum behavior. First, we will show that the bound pairs allow us to send nonlocal signals between the two probes. Second, we will show that these pairs can couple the quantum mechanical phases of the electrons on the two probes. These effects provide evidence of two recently predicted processes that use the superconducting pairs to mediate signals between nanoscale probes: elastic cotunneling and crossed Andreev reflection. In the first process, the pairs facilitate a long-range transfer of electrons from one probe to the other. In the second, the pairs themselves break up, with one constituent electron entering one probe and one the other.

This thesis is organized as follows:

Chapter 2 introduces some of the basics of superconductivity and the physics that arises when other materials, e. g. normal metals, are used as probes of superconductors. Concepts such as charge imbalance, Andreev reflection, and the DC Josephson effect are reviewed in a fairly self-contained presentation, intended for the educated layperson with a passing knowledge of the second-quantized formulation of quantum mechanics. Those readers who are superconductor-savvy may wish to skip this chapter.

Chapter 3 describes the basics of crossed Andreev reflection and elastic cotunneling, and proceeds to review many of the theoretical models and experimental data of other investigations into these processes.

Chapter 4 describes the experimental procedures and techniques used to produce the data of the subsequent chapter. Many of the included details are intended for future residents of Northwestern's Mesoscopic Research Lab.

Chapter 5 is the heart of the thesis, where the results of a series of experiments probing superconductors on the pair length scale are presented and interpreted.

Chapter 6 offers a summary of our findings and some ideas for future experiments.

CHAPTER 2

Theoretical Background

As this thesis concerns probing superconductors on small length scales, we first present an overview of some fundamental theoretical concepts concerning superconductivity and mesoscopic physics. Much of the material covered can be found in introductory texts on these two fields [1, 2, 3, 4, 5]. We here highlight the ideas necessary for understanding the phenomena of crossed Andreev reflection and elastic cotunneling discussed in the subsequent chapters, along with additional processes that are present in our experiments.

2.1. Cooper's Pairs

While the discovery of perfect conductivity in metals at low temperatures by Heike Kamerlingh Onnes occurred in 1911 [6], not until the middle of the twentieth century did a suitable model for the microscopic behavior of electrons in superconductors appear. Though there was speculation at the time that superconductivity was due to a Bose-Einstein condensation of charge carriers [7], it took an examination of the highly degenerate states at the Fermi surface of an electron gas by Leon Cooper to identify a suitable bosonic candidate. Cooper noticed certain symmetries in the matrix describing the Fermi surface that allowed him to break the problem into submatrices between two electrons [8]. This two electron problem can be tackled as follows:

First, begin by constructing a two-electron wavefunction using a superposition of plane wave states with zero net momentum

$$(2.1) \quad \psi(\mathbf{r}_1, \sigma_1; \mathbf{r}_2, \sigma_2) = \sum_{\mathbf{k}} g_{\mathbf{k}} e^{i\mathbf{k} \cdot (\mathbf{r}_1 - \mathbf{r}_2)} \chi(\sigma_1, \sigma_2).$$

This wavefunction must satisfy the antisymmetric property of fermions

$$(2.2) \quad \psi(\mathbf{r}_1, \sigma_1; \mathbf{r}_2, \sigma_2) = -\psi(\mathbf{r}_2, \sigma_2; \mathbf{r}_1, \sigma_1),$$

which we do by using the singlet spin state,

$$(2.3) \quad \chi(\sigma_1, \sigma_2) = \sigma_{\uparrow} \sigma_{\downarrow} - \sigma_{\downarrow} \sigma_{\uparrow},$$

and leaving the spatial part symmetric under particle exchange. This spin state will turn out to be the appropriate choice for the elemental superconductors we study.

Putting the two-particle wavefunction into the Schödinger equation

$$(2.4) \quad -\frac{\hbar^2}{2m} (\nabla_1^2 + \nabla_2^2) \psi(\mathbf{r}_1, \mathbf{r}_2) + V(\mathbf{r}_1, \mathbf{r}_2) \psi(\mathbf{r}_1, \mathbf{r}_2) = E \psi(\mathbf{r}_1, \mathbf{r}_2),$$

we restrict ourselves to the case where the potential is translationally invariant, $V(\mathbf{r}_1, \mathbf{r}_2) = V(\mathbf{r})$ where $\mathbf{r} \equiv \mathbf{r}_1 - \mathbf{r}_2$. Letting $\epsilon_{\mathbf{k}} \equiv \frac{\hbar^2 k^2}{2m}$, and putting Eq. 2.1 into Eq. 2.4 yields

$$(2.5) \quad \sum_{\mathbf{k}} g_{\mathbf{k}} e^{i\mathbf{k} \cdot \mathbf{r}} (E - 2\epsilon_{\mathbf{k}} - V(\mathbf{r})) = 0.$$

To isolate the individual $g_{\mathbf{k}}$ expansion parameters, we multiply through by $e^{-i\mathbf{k}' \cdot \mathbf{r}} / L^3$ (L^3 being the volume of the superconductor, necessary for normalization) and integrate

over \mathbf{r}

$$(2.6) \quad g_{\mathbf{k}'}(E - 2\epsilon_{\mathbf{k}'}) - \sum_{\mathbf{k}} g_{\mathbf{k}} V_{\mathbf{k}\mathbf{k}'} = 0 \implies g_{\mathbf{k}'} = \frac{\sum_{\mathbf{k}} g_{\mathbf{k}} V_{\mathbf{k}\mathbf{k}'}}{E - 2\epsilon_{\mathbf{k}'}} ,$$

where we use the completeness of the plane wave states and

$$(2.7) \quad V_{\mathbf{k}\mathbf{k}'} \equiv \int V(\mathbf{r}) e^{i(\mathbf{k}-\mathbf{k}')\cdot\mathbf{r}} d\mathbf{r}.$$

$V_{\mathbf{k}\mathbf{k}'}$ is the scattering amplitude for transitioning from a pair state indexed by \mathbf{k}' to \mathbf{k} . In the simplest model $V_{\mathbf{k}\mathbf{k}'}$ is taken to be a constant V for all these transitions. We can then sum Eq. 2.7 over \mathbf{k}' and cancel the $g_{\mathbf{k}}$ sums on both sides leaving

$$(2.8) \quad 1 = V \sum \frac{1}{E - 2\epsilon_{\mathbf{k}'}} \implies 1 = V \int_a^b \frac{N(\epsilon_{\mathbf{k}'})}{E - 2\epsilon_{\mathbf{k}'}} d\epsilon_{\mathbf{k}'}$$

We have here converted the sum into an integral using the density of states per spin $N(\epsilon_{\mathbf{k}})$, and placed limits on the integration. While we have not yet restricted these limits from integrating over all energies, we can see from Eq. 2.8 that the integral will logarithmically diverge if we do not do so, implying only trivial $g_{\mathbf{k}} \equiv 0$ solutions of Eq. 2.7. These limits must come from a revision to our model based on physical considerations. For limits in the vicinity of the Fermi energy, though, we can evaluate the integral using the approximation that $N(\epsilon_{\mathbf{k}})$ is a constant $N(0)$ in this range

$$(2.9) \quad 1 = \frac{-1}{2N(0)V} \ln \frac{E - 2b}{E - 2a}.$$

The energy $2a$ is the lowest two-electron kinetic energy that is summed over to create our two particle state, so it is enlightening to compare it to the energy E for this new

state. Rearranging Eq. 2.9 yields

$$(2.10) \quad E - 2a = \frac{2b - 2a}{1 - e^{-2/N(0)V}}.$$

From this equation we can see that for any positive potential V the pair state has an energy higher than the lowest kinetic energy of the plane wave states used to create it. However, for a negative, attractive potential, no matter how small, the energy of the pair state is *lower* than these bare kinetic energies of the states used to create it.

To make this picture more concrete we can use the limits a and b invoked by Cooper. For the upper limit, the integral is cut off by identifying the attractive potential with electron-phonon interactions which should be energetically confined to a region within roughly $\hbar\omega_D$ of the Fermi energy, where ω_D is the Debye frequency of the crystal lattice. We note that $\hbar\omega_D$ is several orders of magnitude lower than E_F which justifies our $N(\epsilon_{\mathbf{k}}) \approx N(0)$ assumption. For the lower limit, Cooper noted that the initial sum over plane wave states in Eq. 2.1 should be limited to those states outside of the filled Fermi sea by the Pauli exclusion principle, identifying the Fermi energy E_F as our bound a . Thus, despite being a superposition of single electron states with bare kinetic energies above the Fermi surface, Eq. 2.10 shows this Cooper pair state has an energy lower than two free electrons at the Fermi surface. Using the $a = E_F$ and $b = \hbar\omega_D + E_F$ limits in Eq. 2.10 we can explicitly calculate the amount Δ by which the energy is lowered for the physically reasonable limit of $N(0)V \ll 1$:

$$(2.11) \quad \Delta = 2\hbar\omega_D e^{-2/N(0)V}.$$

The Bosonic character of this two-electron state allows it to become occupied with multiple pairs of electrons. However, a paradox quickly arises. As paired electrons at the Fermi surface can now occupy this lower energy state, the surface will disappear, which will lower the Pauli exclusion bound a in Eq. 2.8 and alter both the bound state energy Δ and the wavefunction for the paired state. This process should continue until the energy of the paired state is no longer energetically favorable or, perhaps, until we hit a lower limit of $E_F - \hbar\omega_D$ where the phonon interaction is no longer present. In order to account for this rearranging of the electrons around the Fermi surface it is necessary to use a full, many-body theoretical treatment.

2.2. BCS

Such a treatment was realized by Cooper and his colleagues John Bardeen and J. Robert Schrieffer in the months after Cooper's initial insight [10, 11]. Known as the BCS theory after its authors' surnames, perhaps the central breakthrough into constructing a tractable many-body wavefunction for the superconducting ground state was the conjecture that even in the ground state of the system, the single electron states might only be probabilistically occupied. Thus, instead of using the plane wave operators $\hat{c}_{\mathbf{k}\sigma}$ to construct a wavefunction like the Fermi gas at zero temperature

$$(2.12) \quad |FS\rangle = \prod_{|\mathbf{k}| < k_F} \left(\hat{c}_{\mathbf{k}\uparrow}^\dagger \hat{c}_{-\mathbf{k}\downarrow}^\dagger \right) |0\rangle$$

where each electronic state with energy below E_F is definitely occupied while those above E_F in energy are definitely empty, BCS posited that the ground state could be written as

$$(2.13) \quad |BCS\rangle = \prod_{\mathbf{k}} \left(u_{\mathbf{k}} + v_{\mathbf{k}} \hat{c}_{\mathbf{k}\uparrow}^\dagger \hat{c}_{-\mathbf{k}\downarrow}^\dagger \right) |0\rangle$$

where for each zero-momentum pair of electrons there is a probability amplitude for whether the state will or will not be occupied. These $u_{\mathbf{k}}$ and $v_{\mathbf{k}}$ amplitudes, which for the moment we take to be real, are known as coherence factors and imply that for each pair indexed by \mathbf{k} , there is a $v_{\mathbf{k}}^2$ probability that the pair is occupied and a $u_{\mathbf{k}}^2$ probability that it is unoccupied. From these probabilities we conclude

$$(2.14) \quad u_{\mathbf{k}}^2 + v_{\mathbf{k}}^2 = 1,$$

which also serves to normalize the $|BCS\rangle$ wavefunction.

The use of coherence factors has the perverse consequence that the many body wavefunction describing a superconductor does not have a definite number of electrons. Though \hat{N} is no longer a good quantum number, it turns out that its expectation value

$$(2.15) \quad \langle \hat{N} \rangle = \sum_{\mathbf{k}} 2v_{\mathbf{k}}^2$$

(where we used the fact that each pair has a $v_{\mathbf{k}}^2$ chance of being present) is sharply peaked about a value N that is nearly equivalent to the electron number in the normal state described by Eq. 2.12.

In the many-body treatment, the Cooper pair state, with an energy Δ below the Fermi energy and described by Eq. 2.1, is still a superposition of plane wave functions, however it

can now be composed of any number of zero-momentum pairs forming a macroscopically occupied condensate. To find this state we utilize the many-body field operators expanded in the plane wave basis,

$$(2.16) \quad \hat{\Psi}_\uparrow(\mathbf{r}) = \sum_{\mathbf{k}} \frac{e^{i\mathbf{k}\cdot\mathbf{r}}}{L^{3/2}} \hat{c}_{\mathbf{k}\uparrow} \quad \hat{\Psi}_\downarrow(\mathbf{r}) = \sum_{\mathbf{k}} \frac{e^{i\mathbf{k}\cdot\mathbf{r}}}{L^{3/2}} \hat{c}_{\mathbf{k}\downarrow},$$

and the anticommutation relations

$$(2.17) \quad [\hat{c}_{\mathbf{k}\sigma}, \hat{c}_{\mathbf{k}'\sigma'}]_+ = 0 \quad [\hat{c}_{\mathbf{k}\sigma}^\dagger, \hat{c}_{\mathbf{k}'\sigma'}^\dagger]_+ = 0 \quad [\hat{c}_{\mathbf{k}\sigma}^\dagger, \hat{c}_{\mathbf{k}'\sigma'}]_+ = \delta_{\mathbf{k},\mathbf{k}'} \delta_{\sigma,\sigma'}.$$

Knowing the singlet character of the bound electrons, we can use the field operators to calculate the spatial form of the condensate wavefunction:

$$(2.18) \quad \begin{aligned} & \langle BCS | \hat{\Psi}_\downarrow(\mathbf{r}_1) \hat{\Psi}_\uparrow(\mathbf{r}_2) - \hat{\Psi}_\uparrow(\mathbf{r}_2) \hat{\Psi}_\downarrow(\mathbf{r}_1) | BCS \rangle \\ &= \sum_{\mathbf{k}_1, \mathbf{k}_2} \frac{e^{i(\mathbf{k}_1 \cdot \mathbf{r}_1 + \mathbf{k}_2 \cdot \mathbf{r}_2)}}{L^3} (\langle BCS | \hat{c}_{\mathbf{k}_1\downarrow} \hat{c}_{\mathbf{k}_2\uparrow} | BCS \rangle - \langle BCS | \hat{c}_{\mathbf{k}_2\uparrow} \hat{c}_{\mathbf{k}_1\downarrow} | BCS \rangle) \\ &= \sum_{\mathbf{k}} \frac{e^{i\mathbf{k}\cdot(\mathbf{r}_1 - \mathbf{r}_2)}}{L^3} (u_{\mathbf{k}} v_{\mathbf{k}} - (-u_{\mathbf{k}} v_{\mathbf{k}})) \\ &= \sum_{\mathbf{k}} (2u_{\mathbf{k}} v_{\mathbf{k}}) \frac{e^{i\mathbf{k}\cdot\mathbf{r}}}{L^3}, \end{aligned}$$

where $\mathbf{r} \equiv \mathbf{r}_1 - \mathbf{r}_2$ as before. Extending our interpretation of the many-body state in terms of zero-momentum pairs, we see from this expansion that each pair contributes to the condensate with probability $2u_{\mathbf{k}}v_{\mathbf{k}}$.

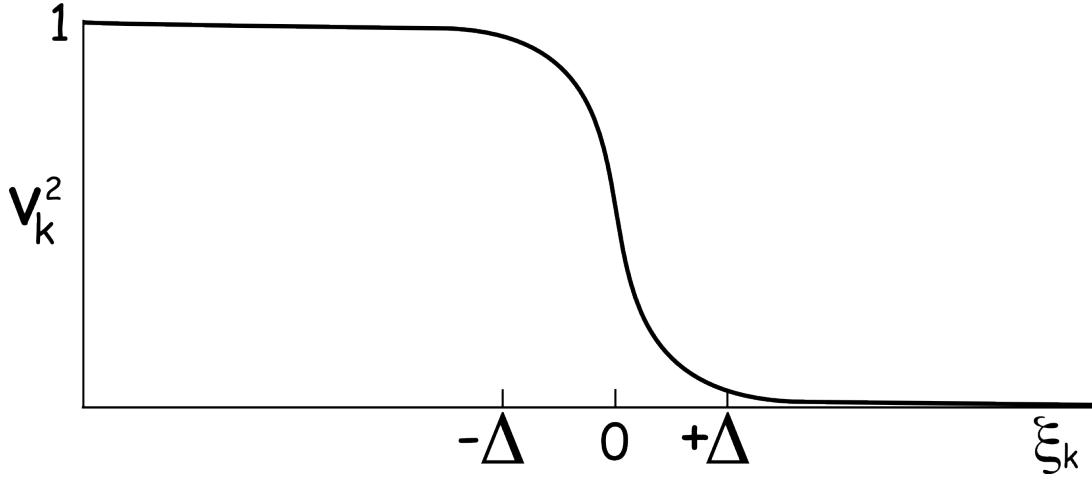


Figure 2.1. Graph of the occupation probability $v_{\mathbf{k}}^2$ for the BCS ground state.

With this probability in hand we can now write down the total energy $\langle \hat{H} \rangle$ of the $|BCS\rangle$ state by inspection

$$(2.19) \quad \langle \hat{H} \rangle = \sum_{\mathbf{k}} (2\epsilon_{\mathbf{k}} v_{\mathbf{k}}^2 - 2u_{\mathbf{k}} v_{\mathbf{k}} \Delta)$$

i. e. for each pair index \mathbf{k} there is a $v_{\mathbf{k}}^2$ probability of its occupation contributing $2\epsilon_{\mathbf{k}}$ to the kinetic energy and a $2u_{\mathbf{k}}v_{\mathbf{k}}$ probability of its participation in the condensate state that lowers the energy by an amount Δ . To find explicit forms for the coherence factors we should minimize the energy. However, since the particle number of the state is no longer fixed, the correct thermodynamic quantity to minimize is $\langle \hat{H} - \mu \hat{N} \rangle$. While the chemical potential μ is lowered slightly by the formation of the condensate, this is a small correction compared with its $\mu = E_F$ value in the normal state. Using this approximation along with Eq. 2.15 and 2.19 we set out to minimize:

$$(2.20) \quad \langle \hat{H} - \mu \hat{N} \rangle = 2 \sum_{\mathbf{k}} (\xi_{\mathbf{k}} v_{\mathbf{k}}^2 - u_{\mathbf{k}} v_{\mathbf{k}} \Delta)$$

with respect to $u_{\mathbf{k}}$ and $v_{\mathbf{k}}$. We have introduced the notation $\xi_{\mathbf{k}} = \epsilon_{\mathbf{k}} - E_F$, which measures the kinetic energy with respect to the Fermi energy and has the advantage of being linear with $|\mathbf{k}|$ near this energy: $\xi_{\mathbf{k}} \approx \hbar v_F (|\mathbf{k}| - k_F)$ (v_F and k_F are the Fermi velocity and wavevector respectively). Minimizing Eq. 2.20 with respect to $v_{\mathbf{k}}$ gives

$$(2.21) \quad \frac{\partial \langle \hat{H} - \mu \hat{N} \rangle}{\partial v_{\mathbf{k}}} = 4\xi_{\mathbf{k}}v_{\mathbf{k}} - 2\Delta u_{\mathbf{k}} - 2\Delta \frac{\partial u_{\mathbf{k}}}{\partial v_{\mathbf{k}}} = 0.$$

We can eliminate terms with $u_{\mathbf{k}}$ by using the normalization relation Eq. 2.14 to derive

$$(2.22) \quad u_{\mathbf{k}} = (1 - v_{\mathbf{k}}^2)^{1/2} \quad \frac{\partial u_{\mathbf{k}}}{\partial v_{\mathbf{k}}} = \frac{-v_{\mathbf{k}}}{(1 - v_{\mathbf{k}}^2)^{1/2}}.$$

Substituting these relations into Eq. 2.21 and solving for the probability $v_{\mathbf{k}}^2$ gives

$$(2.23) \quad v_{\mathbf{k}}^2 = \frac{1}{2} \left(1 - \frac{\xi_{\mathbf{k}}}{(\xi_{\mathbf{k}}^2 + \Delta^2)^{1/2}} \right).$$

From this formula and its graph (Fig. 2.1) we can see that pairs of states with $\xi_{\mathbf{k}} \lesssim -\Delta$ are almost entirely occupied, while those with $\xi_{\mathbf{k}} \gtrsim \Delta$ are almost entirely unoccupied. Only within a range Δ of the Fermi energy does the peculiar uncertainty concerning whether pairs of electrons are present arise. Substituting Eq. 2.23 into Eq. 2.22 shows

$$(2.24) \quad u_{\mathbf{k}}^2 = \frac{1}{2} \left(1 + \frac{\xi_{\mathbf{k}}}{(\xi_{\mathbf{k}}^2 + \Delta^2)^{1/2}} \right),$$

which, together with Eq. 2.23, we can use these to calculate the other important probability

$$(2.25) \quad 2u_{\mathbf{k}}v_{\mathbf{k}} = \frac{\Delta}{(\xi_{\mathbf{k}}^2 + \Delta^2)^{1/2}}.$$

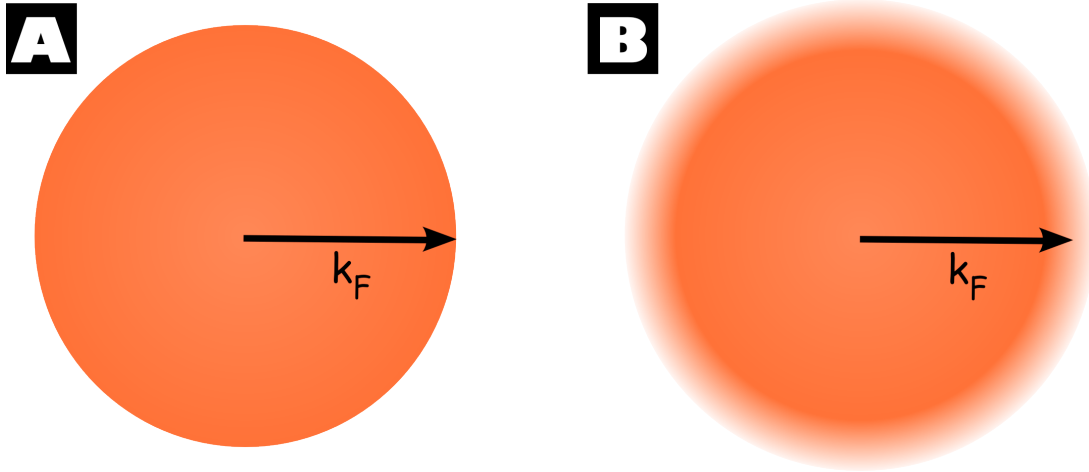


Figure 2.2. When a small attractive potential is present between electrons, the ground state of a Fermi gas **(A)** rearranges itself to create a new state with energy Δ below the Fermi Surface. **(B)** In the BCS theory this rearrangement causes single electron states to become probabilistically occupied around the original Fermi surface.

Examining this equation in conjunction with the spatial form of our condensate wavefunction, Eq. 2.18, we see that the components of our plane wave expansion decay out over an energy scale of $\sim \Delta$, a wavevector scale of $\sim \Delta/\hbar v_F$, and a hence a position scale of $\sim \hbar v_F/\Delta$. Since this position \mathbf{r} is the difference between the \mathbf{r}_1 and \mathbf{r}_2 positions of the two components for each Cooper pair that participates in the condensate, this length scale represents the effective size over which spin \uparrow and spin \downarrow electrons are highly correlated in the superconductor. Known as the BCS coherence length ξ_0 , textbook values [12] of Δ and v_F for a material such as aluminum indicate it can be many microns for a pure material. For the diffusive (“dirty”) materials studied in Chapter 5, the mean free path of an electron l_e is much shorter than this, tens of nanometers, which limits the coherence length to $\xi_S \sim (\xi_0 l_e)^{1/2}$, on the order of several hundred nanometers. Looking for effects

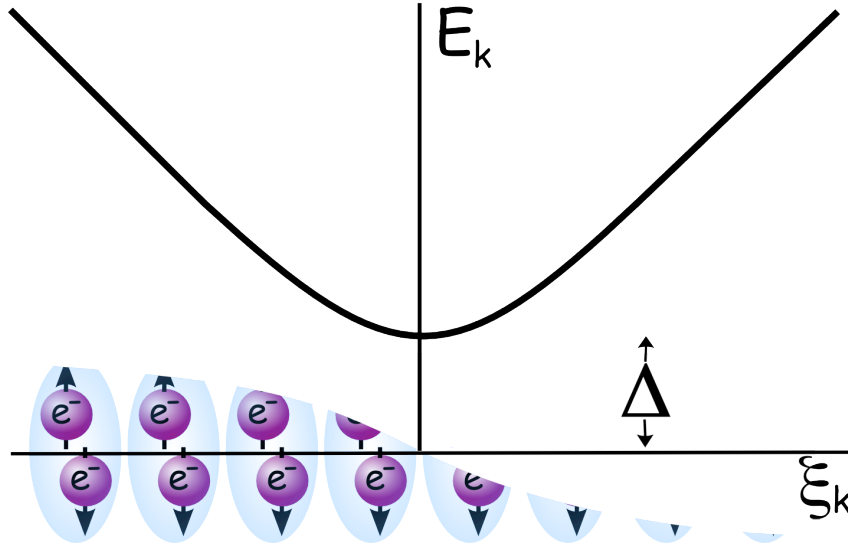


Figure 2.3. Energy excitation spectrum in the BCS formalism. The minimum energy excitation lies at an energy Δ above the condensate, which is schematically represented as partially occupied pairs reflecting the probability curve of Fig. 2.1.

between probes placed on a superconductor within this length scale of each other will be the central focus of this thesis.

Having established some properties of the ground state, we now turn to examining higher energy excitations of the BCS wavefunction. To create the simplest excitation we return to Eq. 2.13 and remove the ambiguity of whether or not a single zero momentum pair state is occupied by definitively placing an electron in that state:

$$(2.26) \quad |BCS\rangle = \prod_{\mathbf{k}} \left(u_{\mathbf{k}} + v_{\mathbf{k}} \hat{c}_{\mathbf{k}\uparrow}^\dagger \hat{c}_{-\mathbf{k}\downarrow}^\dagger \right) |0\rangle \quad \longrightarrow \quad \hat{c}_{\mathbf{p}\uparrow}^\dagger \prod_{\mathbf{k} \neq \mathbf{p}} \left(u_{\mathbf{k}} + v_{\mathbf{k}} \hat{c}_{\mathbf{k}\uparrow}^\dagger \hat{c}_{-\mathbf{k}\downarrow}^\dagger \right) |0\rangle.$$

It can be seen by inspection that this excitation can be accomplished using the operator

$$(2.27) \quad \gamma_{\mathbf{k}\uparrow}^\dagger = u_{\mathbf{k}} \hat{c}_{\mathbf{k}\uparrow}^\dagger - v_{\mathbf{k}} \hat{c}_{-\mathbf{k}\downarrow},$$

so that

$$(2.28) \quad \gamma_{\mathbf{p}\uparrow}^\dagger |BCS\rangle = \hat{c}_{\mathbf{p}\uparrow}^\dagger \prod_{\mathbf{k} \neq \mathbf{p}} \left(u_{\mathbf{k}} + v_{\mathbf{k}} \hat{c}_{\mathbf{k}\uparrow}^\dagger \hat{c}_{-\mathbf{k}\downarrow}^\dagger \right) |0\rangle.$$

There is a second operator

$$(2.29) \quad \gamma_{\mathbf{k}\downarrow}^\dagger = u_{\mathbf{k}} \hat{c}_{-\mathbf{k}\downarrow}^\dagger + v_{\mathbf{k}} \hat{c}_{\mathbf{k}\uparrow}$$

that can be used to definitively place a spin \downarrow electron into the BCS state. These quasi-particle creation operators obey the usual anticommutation relations for fermions,

$$(2.30) \quad [\hat{\gamma}_{\mathbf{k}\sigma}, \hat{\gamma}_{\mathbf{k}'\sigma'}]_+ = 0 \quad [\hat{\gamma}_{\mathbf{k}\sigma}^\dagger, \hat{\gamma}_{\mathbf{k}'\sigma'}^\dagger]_+ = 0 \quad [\hat{\gamma}_{\mathbf{k}\sigma}^\dagger, \hat{\gamma}_{\mathbf{k}'\sigma'}]_+ = \delta_{\mathbf{k},\mathbf{k}'} \delta_{\sigma,\sigma'}.$$

In creating these excitations we alter the condensate by removing a term from our plane wave expansion, and consequently increase the energy level of this state. However, for a small number of excitations we can take Δ to be constant and in so doing can simplify the calculation of the excitation energies. Since an excitation using $\hat{\gamma}_{\mathbf{k}}$ has changed the probable number of particles in the full many-body state by an amount $1 - 2v_{\mathbf{k}}^2$, the kinetic energy of the system may increase or decrease. But removing the pair contribution to the condensate will always result in a $2u_{\mathbf{k}}v_{\mathbf{k}}\Delta$ energy increase. The total energy of an excitation is seen to be

$$(2.31) \quad \begin{aligned} E_{\mathbf{k}} &= (1 - 2v_{\mathbf{k}}^2)\xi_{\mathbf{k}} + 2u_{\mathbf{k}}v_{\mathbf{k}}\Delta \\ &= (\xi_{\mathbf{k}}^2 + \Delta^2), \end{aligned}$$

where we have used Eq. 2.23 and 2.25. The excitation spectrum of the quasiparticles is shown in Fig. 2.3. Since Δ is the minimum energy required to produce a quasiparticle excitation it is referred to as the superconducting gap energy.

2.3. Charge Imbalance

One peculiarity of the quasiparticle excitations is that the expectation value of \hat{N} , and hence the expectation value of the charge of the system, is not necessarily conserved. The $1 - 2v_{\mathbf{k}}^2 = \xi_{\mathbf{k}}/E_{\mathbf{k}} = (E_{\mathbf{k}}^2 - \Delta^2)^{1/2}/E_{\mathbf{k}}$ change to the number of electrons in the system means that excitations with indices \mathbf{k} greater in magnitude than k_F will be “electron-like”, while those with indices \mathbf{k} smaller in magnitude than k_F are “hole-like”. These two types of quasiparticles are shown in Fig. 2.4(A) & (B) respectively. If the excited state of the superconductor is in equilibrium, such as when its temperature is raised, the symmetry in energy between the electron-like branch and hole-like branch dictate that excitations should be balanced about k_F (Fig. 2.4(C)). In this case the occupation probability for an excitation $E_{\mathbf{k}}$ is given by the usual Fermi-Dirac distribution,

$$(2.32) \quad f_0(E_{\mathbf{k}}) = \frac{1}{1 + e^{(-E_{\mathbf{k}} - \mu\hat{N})/k_B T}},$$

where k_B is Boltzmann’s constant.

For a non-equilibrium situation it is possible that one type of excitation could be favored over the other, as shown in Fig. 2.4(D). The resulting distribution can be accounted for using a general quasiparticle occupation probability $f(E_{\mathbf{k}}) = f_0(E_{\mathbf{k}}) + \delta f(E_{\mathbf{k}})$. When the occupation number of electron-like quasiparticles $n(E_{\mathbf{k}})$ differs from the number of hole-like ones $p(E_{\mathbf{k}})$ the system is said to have a branch imbalance. It is then useful to

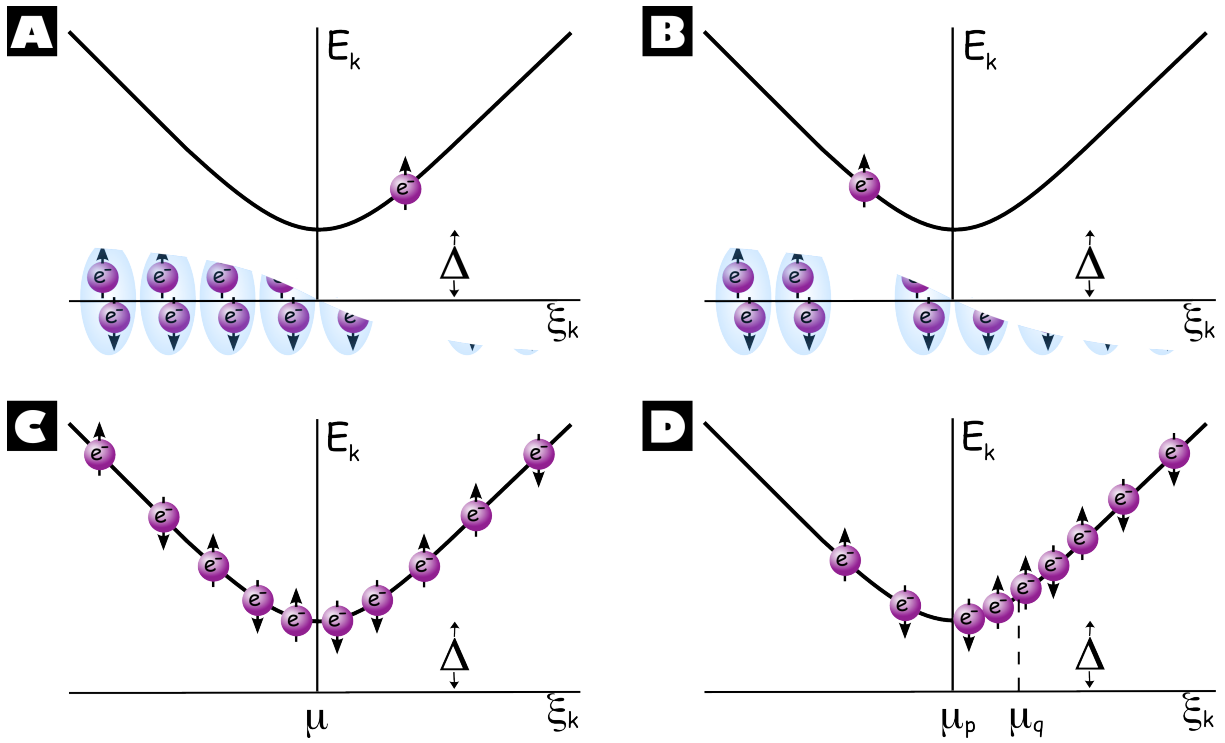


Figure 2.4. In the single electron picture of the BCS ground state, each electron state has a probabilistic occupation $2v_{\mathbf{k}}^2$ for a given wavenumber \mathbf{k} . Quasiparticle excitations out of the ground state definitively place a single electron at this wavenumber which alters the expected number of electrons in the superconductor by $(1-2v_{\mathbf{k}}^2)$. (A) Excitations with $|\mathbf{k}| > k_F$ increase the expected number of electrons and are “electron-like”. (B) Excitations with $|\mathbf{k}| < k_F$ decrease the expected number of electrons and are “hole-like”. (C) If the excitations are in equilibrium, such as when the temperature of the superconductor is increased, the net charge of the system and its chemical potential μ is not altered. (D) If the superconductor is not in equilibrium, the quasiparticle excitations can result in a net charge imbalance. In this circumstance the chemical potential of these excitations μ_q is different than the Cooper pair condensate potential μ_p . [Figure after [17]]

define a distribution function $f_-(E_{\mathbf{k}}) \equiv n(E_{\mathbf{k}}) - p(E_{\mathbf{k}})$, which is non-zero if and only if there is a branch imbalance. This function is variously called the “transverse”, “odd”, or “anti-symmetric” distribution function and comprises all or part of $\delta f(E_{\mathbf{k}})$.¹

Weighting this transverse component of the non-equilibrium distribution by the effective charge of each quasiparticle gives an expression

$$(2.33) \quad Q^* \equiv \sum_{E_{\mathbf{k}}} e f_-(E_{\mathbf{k}}) \frac{(E_{\mathbf{k}}^2 - \Delta^2)^{1/2}}{E_{\mathbf{k}}}$$

for the total charge imbalance of the system. As shown in Fig. 2.4(D) this charge imbalance results in the chemical potential of the quasiparticles μ_q shifting away from the chemical potential of the pair condensate μ_p . The simplest way to create this nonequilibrium charge imbalance is to inject a current into the superconductor from a normal metal, as discussed below in the BTK model. The current flow will be conserved by the condensate supercurrent, while the created quasiparticles will pool near the normal metal interface, diffusing in the superconductor until they reequilibrate with the pair potential. This reequilibration will take place over a characteristic time scale τ_{Q^*} and length scale λ_{Q^*} . Thus there will be a volume within $\sim \lambda_{Q^*}$ of the interface where it is possible to probe the charge imbalance. If a normal metal probe is placed on the superconductor within this volume it can equilibrate with the imbalanced μ_q quasiparticle potential which can be compared to the differing equilibrium potential of a superconducting probe. Such an experiment was first performed by J. Clarke [16] and explained in a manner that we

¹The definition of this function and its “longitudinal”, “even”, or “symmetric” counterpart can differ from author to author, compare, e. g., [13, 14, 15].

have echoed here by M. Tinkham and J. Clarke [17]. Subsequent experiments examining the temperature, current, and spatial dependence of the charge imbalance voltages [18, 19, 20, 21, 22, 23, 24, 25, 26] in conjunction with models of quasiparticle relaxation processes [27, 28] yielded τ_{Q^*} relaxation times on the order of nanoseconds and λ_{Q^*} lengths on the order of microns for a variety of different superconductors.

2.4. The Josephson Effect

As with any wavefunction, the condensate state of Eq. 2.18 may have a phase factor $e^{i\phi}$ which is relevant only when it is interacting with itself or other quantum objects. To produce this phase factor in the spatial wavefunction, one can alter the BCS many-body state as follows:

$$(2.34) \quad |BCS_\phi\rangle = \prod_{\mathbf{k}} \left(u_{\mathbf{k}} + e^{i\phi} v_{\mathbf{k}} \hat{c}_{\mathbf{k}\uparrow}^\dagger \hat{c}_{-\mathbf{k}\downarrow}^\dagger \right) |0\rangle.$$

It was noted by P. W. Anderson [29] that this phase factor allows one to write down a useful relation between the BCS state and states $|N\rangle$ that have a *definite* number of electron pairs. Since in expanding the product of $|BCS_\phi\rangle$ each term with N creation operators contains a $e^{iN\phi/2}$ phase factor, we can write the expansion

$$(2.35) \quad |BCS_\phi\rangle = \sum_N A_N e^{iN\phi/2} |N\rangle,$$

from which follows the useful relation when working with states that have definite phases

$$(2.36) \quad \hat{N}|BCS_\phi\rangle = \sum_N N A_N e^{iN\phi/2} |N\rangle = (-2i \frac{\partial}{\partial \phi}) \sum_N A_N e^{iN\phi/2} |N\rangle = (-2i \frac{\partial}{\partial \phi}) |BCS_\phi\rangle$$

or

$$(2.37) \quad \hat{N} = -2i \frac{\partial}{\partial \phi}.$$

An effect of this electron number-phase relation was uncovered by B. D. Josephson for the case of two superconductors separated by a barrier that allows them to have different phases [30]. We can derive this effect by first writing down a hamiltonian for tunneling electrons from one superconductor to the other

$$(2.38) \quad \hat{H}_T = \sum_{\mathbf{k}, \mathbf{q}} T_{\mathbf{k}, \mathbf{q}} \hat{c}_{\mathbf{k}}^\dagger \hat{c}_{\mathbf{q}} + T_{\mathbf{k}, \mathbf{q}}^\dagger \hat{c}_{\mathbf{q}}^\dagger \hat{c}_{\mathbf{k}}$$

where the \mathbf{k} indices are for the superconductor with phase ϕ_1 and the \mathbf{q} indices are for the superconductor with phase ϕ_2 . Writing the BCS wavefunctions according to their phases, the first order correction to their ground state energy E_0 will be

$$(2.39) \quad E_1 = \langle \phi_1, \phi_2 | \hat{H}_T | \phi_1, \phi_2 \rangle.$$

However, since the terms of the tunneling hamiltonian change the BCS state to a superposition of states with *odd* numbers of electrons, this correction is zero. Moving to the second order correction

$$(2.40) \quad E_2 = \sum_M \frac{\langle \phi_1, \phi_2 | \hat{H}_T | M \rangle \langle M | \hat{H}_T | \phi_1, \phi_2 \rangle}{E_0 - E_M},$$

where $|M\rangle$ is an intermediate state, we can gain some insight into its phase dependence by using the expansion of Eq. 2.35 to get

$$(2.41) \quad \sum_{M, N_1, N'_1, N_2, N'_2} A_{N_1} A_{N'_1} A_{N_2} A_{N'_2} \frac{\langle N'_1, N'_2 | \hat{H}_T | M \rangle \langle M | \hat{H}_T | N_1, N_2 \rangle}{E_0 - E_I} e^{-i(N'_1 \phi_1 + N'_2 \phi_2)} e^{i(N_1 \phi_1 + N_2 \phi_2)}.$$

In order for the numerator to be non-zero, the intermediate state must contain terms with $|N_A \pm 1, N_B \mp 1\rangle$ and $|N'_A \pm 1, N'_B \mp 1\rangle$, so that either $N_A = N'_A$ and $N_B = N'_B$ or $N_A - N'_A = N'_B - N_B = \pm 2$. The first choice leads to a phase independent contribution to the energy which we can absorb into E_0 , the second choice gives a sum over terms with phase factors $e^{i\delta\phi}$ and $e^{-i\delta\phi}$ (where $\delta\phi \equiv \phi_1 - \phi_2$). Since the energy is real, the amplitudes for the terms with conjugate phase factors must be equal and the total energy of the system can then be written

$$(2.42) \quad E = E_0 + E_2 \cos \delta\phi.$$

Typically E_2 will be negative and the two superconductors will minimize the total energy by having no phase difference. However, since there is a complementary relation between phase and particle number, a phase difference between the superconductors can be related to particle flow. Starting from Eq. 2.37, we note that

$$(2.43) \quad \delta\hat{N} \equiv \hat{N}_1 - \hat{N}_2 = -2i \left(\frac{\partial}{\partial\phi_1} - \frac{\partial}{\partial\phi_2} \right) = -2i \frac{\partial}{\partial(\delta\phi)},$$

which, along with the definition $|\delta\phi\rangle \equiv |\phi_1, \phi_2\rangle$, we can use to calculate the current from the first superconductor to the second:

$$\begin{aligned}
(2.44) \quad I &= e \frac{\partial}{\partial t} \langle \delta\phi | \delta \hat{N} | \delta\phi \rangle \\
&= e \langle \delta\phi | \frac{i}{\hbar} [\hat{H}, \delta \hat{N}] | \delta\phi \rangle \\
&= \frac{ie}{\hbar} \left(E \langle \delta\phi | \left(-2i \frac{\partial}{\partial(\delta\phi)} \right) | \delta\phi \rangle - \langle \delta\phi | \left(-2i \frac{\partial}{\partial(\delta\phi)} \right) E | \delta\phi \rangle \right) \\
&= \frac{ie}{\hbar} \left(2i \frac{\partial}{\partial(\delta\phi)} \right) E \\
&= \frac{-2e}{\hbar} \frac{\partial E}{\partial(\delta\phi)}.
\end{aligned}$$

This expression for the current along with Eq. 2.42 yields

$$(2.45) \quad I = \frac{2e}{\hbar} E_0 \sin \delta\phi,$$

the formula for the DC Josephson current. Thus, a dissipationless current arises when the two superconductors have different phases, or, conversely and more frequently, a phase difference between the two superconductors is produced by sending a current between them.

While the first experiments to observe this effect used insulating barriers between the two superconductors [31], the transmission coefficients $T_{\mathbf{k},\mathbf{q}}$ of the tunneling hamiltonian are substantial only if this barrier is less than or comparable to k_F^{-1} , i. e. Ångstroms to a few nm. If the barrier is composed of a normal metal, which offers conductive states for Cooper pairs to travel through (although it provides no phonon potential to preserve their pairing), the tunneling supercurrent can exist provided the energy of its carriers is not significantly altered. The quantum mechanical phase $e^{iEt/\hbar}$ sets a threshold of

$(\delta E)t \sim \hbar$ for the allowable energy change δE over time t before the coherent carriers undergo dephasing. For a normal barrier of length L greater than the electron mean free path l_e , the average time it takes to traverse the barrier is $t = L^2/D$, where D is the diffusion constant of the metal. Thus the crossover from phasing to dephasing over the length of the barrier is set by the energy scale

$$(2.46) \quad E_c = \frac{\hbar D}{L^2},$$

a scale known as the correlation or Thouless energy [32]. While a number of inelastic scattering mechanisms can cause this energy change, an inherent limiting factor will be the temperature of the normal metal barrier, which gives a thermal length scale $L_T = \sqrt{\hbar D/k_B T}$ over which the supercurrent dephasing must occur. For a $D \approx 100 \text{ cm}^2\cdot\text{sec}$ diffusion constant (comparable to the normal metals we use) and a $\sim 100 \text{ mK}$ temperature, this length scale indicates the possibility of observing Josephson currents across normal metal barriers of over a micron at low temperatures. Though the general relation of Eq. 2.44 is still valid for such junctions, the junction energy dictated by our tunneling hamiltonian is no longer applicable, leading to possible modifications of Eq. 2.45. For SNS junctions a wide array of current-phase relations can be realized [33], however for the diffusive junctions with barrier lengths greater than ξ_S and transparent interfaces that we will have occasion to examine in Chapter 5, the sinusoidal dependence of Eq. 2.45 should still hold [34].

2.5. Andreev Reflection

To understand the interaction between a normal metal (N) and a superconductor (S) at their interface more fully we can use a hamiltonian of similar form to our Josephson tunneling hamiltonian,

$$(2.47) \quad \hat{H}_{NS} = \sum_{\mathbf{k}, \alpha, \mathbf{q}, \beta} T_{\mathbf{k}\alpha, \mathbf{q}\beta} \hat{c}_{\mathbf{k}\alpha}^\dagger \hat{c}_{\mathbf{q}\beta} + T_{\mathbf{k}\alpha, \mathbf{q}\beta}^\dagger \hat{c}_{\mathbf{q}\beta}^\dagger \hat{c}_{\mathbf{k}\alpha},$$

but where operators with subscripts \mathbf{q} now refer to electronic states inside the normal metal. When considering currents between the two materials it is often useful to express the $\hat{c}_{\mathbf{k}}$ operators in terms of the superconducting quasiparticle creation operators $\hat{\gamma}_{\mathbf{k}}$ by inverting Eq. 2.27 and 2.29 to get

$$(2.48) \quad \hat{c}_{\mathbf{k}\uparrow}^\dagger = u_{\mathbf{k}} \gamma_{\mathbf{k}\uparrow} + v_{\mathbf{k}} \gamma_{\mathbf{k}\downarrow}^\dagger$$

$$(2.49) \quad \hat{c}_{-\mathbf{k}\downarrow}^\dagger = u_{\mathbf{k}} \gamma_{\mathbf{k}\downarrow}^\dagger - v_{\mathbf{k}} \gamma_{\mathbf{k}\uparrow}.$$

With these expansions we can calculate first order transitions where an electron from the normal metal creates a quasiparticle excitation in the superconductor. However, creating these quasiparticle excitations requires the energy of the incoming electron to be at least Δ above the superconductor's chemical potential. If this is not the case we must consider second order two-particle tunneling processes which occur with a rate [35]

$$(2.50) \quad \Gamma = \frac{2\pi}{\hbar} \sum_F \left| \sum_M \frac{\langle F | \hat{H}_T | M \rangle \langle M | \hat{H}_T | I \rangle}{E_M - E_I} \right|^2 \delta(E_F - E_I)$$

given by Fermi's golden rule, where $|I\rangle$ and $|F\rangle$ are the initial and final states of the system, and $|M\rangle$ an intermediate state.

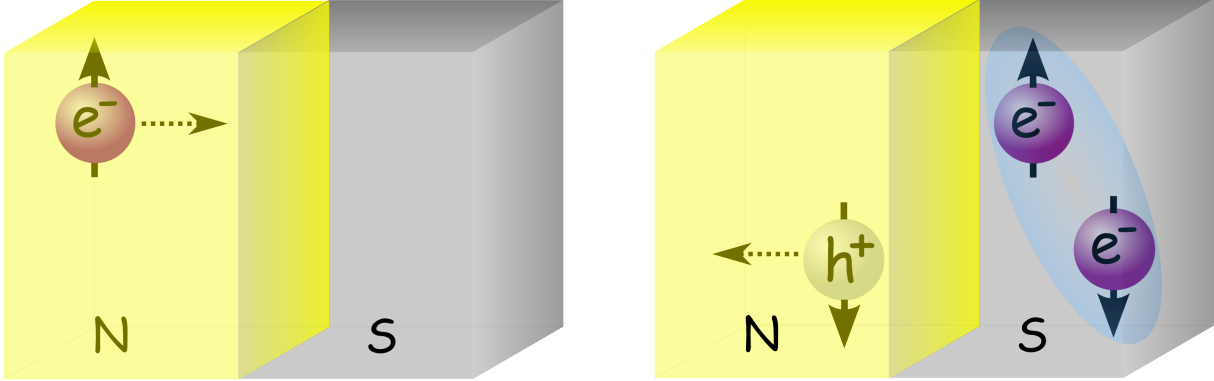


Figure 2.5. When an electron from a normal metal N is incident on an interface with a superconductor S, it is possible for the electron to pair with an electron of opposite spin and momentum to enter the superconductor as a Cooper pair. The second electron leaves behind a hole which is “retroreflected” back into the normal metal.

Restricting our consideration to the momentum and spin conserving case for an incoming electron, $T_{\mathbf{k}\alpha,\mathbf{q}\beta} = A_{\mathbf{k}\alpha}\delta_{\mathbf{k},\mathbf{q}}\delta_{\alpha,\beta}$, and to the case where no quasiparticles are created in the superconductor, we see that there is a finite transition probability involving the matrix elements

$$(2.51) \quad \langle F | A_{-\mathbf{k},\downarrow}^\dagger \delta_{-\mathbf{k},-\mathbf{q}} \hat{c}_{-\mathbf{q}\downarrow}^\dagger \hat{c}_{-\mathbf{k}\downarrow} | M \rangle \langle M | A_{\mathbf{k},\uparrow}^\dagger \delta_{\mathbf{k},\mathbf{q}} \hat{c}_{\mathbf{q}\uparrow}^\dagger \hat{c}_{\mathbf{k}\uparrow} | I \rangle.$$

In this transition, the incoming electron with wavevector \mathbf{k} is removed from the normal metal and a Cooper pair $\hat{c}_{\mathbf{q}\uparrow}^\dagger \hat{c}_{-\mathbf{q}\downarrow}^\dagger$ is added to the condensate. But there is also the destruction of a normal metal electron (or creation of a hole) with $-\mathbf{k}$ wavevector and spin \downarrow . This process of electron retroreflection, or Andreev reflection [36], is shown schematically in Fig. 2.5. It is the mechanism by which electrons with sub-gap energies can enter the superconductor. In the limiting case of a very clean interface between the normal metal and superconductor, with the current being carried at below gap energies, all incident

electrons should retroreflect. Since a Cooper pair enters the condensate for every electron sent towards the interface the conductance of the interface doubles compared to its conductance when the superconductor is in its normal state.

2.6. BTK

For a better accounting of the physics at NS interfaces, particularly of the more transparent variety, it is necessary to move away from the idea of a sharp line between the electronic normal metal states and the condensate and quasiparticle states in the superconductor. In reality the electronic wavefunctions should continuously evolve from one material to the other. Examining our many-body ground state wavefunctions (Eq. 2.12 and 2.13) we see that by adjusting our probability amplitudes we can form one state from the other, i. e. taking the limits

$$(2.52) \quad \begin{array}{lll} u_{\mathbf{k}} \longrightarrow 0 & v_{\mathbf{k}} \longrightarrow 1 & |\mathbf{k}| < k_F \\ u_{\mathbf{k}} \longrightarrow 1 & v_{\mathbf{k}} \longrightarrow 0 & |\mathbf{k}| > k_F \end{array}$$

leads to

$$(2.53) \quad |BCS\rangle \longrightarrow |FS\rangle.$$

More generally we can give the probability amplitudes a spatial dependence which varies across an NS interface or in the presence of an additional potential. Finding this spatial dependence for a given Hamiltonian \hat{H} is the purview of the Bogoliubov-de Gennes

equations [37, 1]:

$$(2.54) \quad \begin{aligned} \hat{H}u(\mathbf{r}) + \Delta(\mathbf{r})v(\mathbf{r}) &= Eu(\mathbf{r}) \\ -\hat{H}v(\mathbf{r}) + \Delta(\mathbf{r})u(\mathbf{r}) &= Ev(\mathbf{r}) \end{aligned}$$

where the solutions $u_n(\mathbf{r})$ and $v_n(\mathbf{r})$ will no longer necessarily be indexed by the wavevector \mathbf{k} appropriate for plane wave solutions. Well inside a normal metal, where $\Delta = 0$, these equations become the usual Schrödinger equations for electrons and holes. In the case of smoothly varying solutions, such as when an NS interface is transparent, the $u_n(\mathbf{r})v_n(\mathbf{r})$ product that characterizes our condensate wavefunction, Eq. 2.18, will penetrate into the normal metal. This leads to a “proximity effect” wherein a normal metal in contact with a superconductor takes on many of its properties [38]. While this effect has been known for many decades, more recent observations of it at semiconductor-superconductor interfaces [39, 40] has led to microscopic models that use quantum interference effects from multiple Andreev reflections at the interfaces to account for the observed increases in their conductance [41, 42].

Using the Bogoliubov-de Gennes equations, G. E. Blonder, M. Tinkham, and T. M. Klapwijk constructed a simple model of an NS interface that accounts for many of the possible transport effects so far discussed [43]. Known as the BTK model, the authors used a simple δ -function boundary potential with adjustable strength Z . Examining an electron traveling towards the boundary from the normal metal side (Fig. 2.6), the authors calculated the probabilities for the four possible results consistent with energy conservation and a group velocity that is unchanged for transmission, but reverses on reflection. For electrons below the gap energy, quasiparticle creation in the superconductor

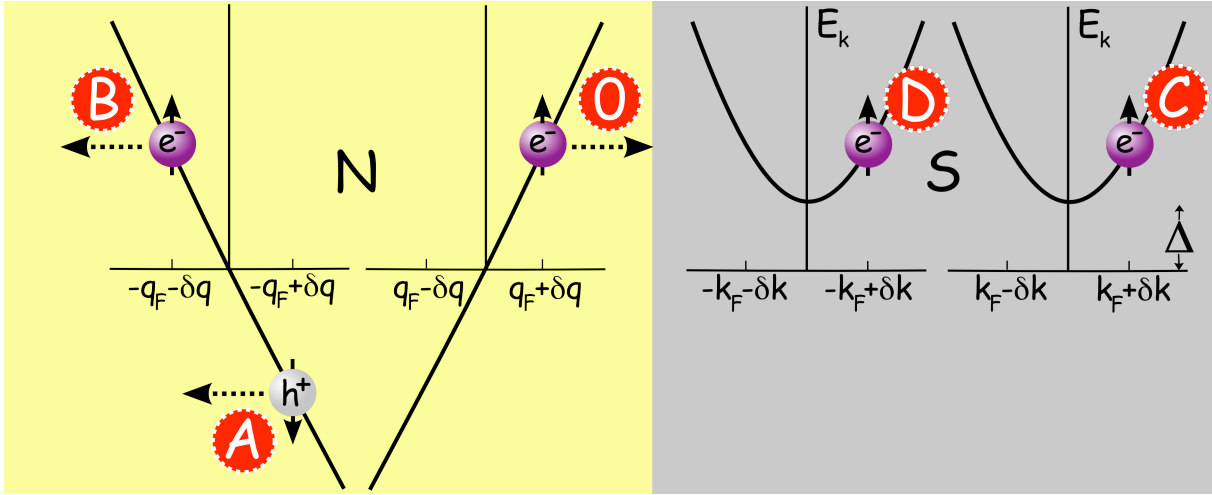


Figure 2.6. In the BTK model, an electron (0) from a normal metal incident on an interface with a superconductor can undergo one of four processes consistent with energy conservation and group velocity considerations. (A) Andreev reflection results in retroreflected hole traveling back into the normal metal. (B) The electron is regularly reflected back into the normal metal. (C) The electron creates an electron-like quasiparticle excitation in the superconductor. (D) The electron creates a hole-like quasiparticle excitation in the superconductor. [Figure after [43]]

is not energetically possible and the electron must undergo (A) Andreev reflection or (B) regular reflection. The latter process will dominate for a strong, high- Z , barrier, but in the transparent interface limit that the experiments of Chapter 5 approach, all sub-gap electrons will Andreev reflect. For energies above the gap, there is the added possibility of quasiparticle excitations, which will dominate the two types of reflection when the interface is of modest transparency or better. As shown in Fig. 2.6 there are two possible types of quasiparticles that the incoming electron can produce, one (C) electron-like and the other (D) hole-like, that are consistent with conserved group velocity. Due to the greater probability that the condensate occupies the hole branch, creation of an electron-like quasiparticle is always favored, particularly so when there is a low- Z barrier.

Therefore, for energies above the gap, there will be a large charge imbalance that develops in the superconductor.

With energy dependent probabilities in hand and a knowledge of the normal metal and quasiparticle density of states, the BTK theory can be used to integrate over the distribution function to obtain predictions for the conductance of the interface and the charge imbalance voltage. Typically, as in the original paper, one uses the equilibrium Fermi-Dirac distribution that depends on temperature and the voltage across the interface. In anticipation of our experiments, where clearly identifying the charge imbalance signal will be important, we note that in the BTK model there is a large predicted charge imbalance signal just under the critical temperature T_c of the superconductor which decays with decreasing temperature. The signal disappears almost entirely by $\sim T_c/2$, particularly for low- Z , high transparency interfaces. This dependence can be understood qualitatively by noting that as the temperature is lowered, the energy of the incident electrons falls more and more within the gap where quasiparticle excitation is not possible.

2.7. Green's Functions

The simplified introduction to the microscopic theory of superconductivity presented above is intended to give the reader some conceptual intuitions regarding processes such as the Josephson effect, charge imbalance, and Andreev reflection. As intimated in exhibiting the Bogoliubov-de Gennes equations, modeling real superconductors and superconducting heterostructures requires including the possibility of additional potentials, temperature dependence, and non-equilibrium conditions that can result in spatial, temporal, and phase variations of the condensate wavefunction, the single electron eigenstates, and the

superconducting energy gap. The most common technique for handling these possibilities are approaches using many-body Green's functions [44, 45]. As with classical Green's functions, many-body Green's functions G typically invert a differential operator, specifically the $i\hbar\frac{\partial}{\partial t} - \hat{H}$ of the Schrödinger equation, to satisfy

$$(2.55) \quad \left(i\hbar\frac{\partial}{\partial t} - \hat{H} \right) G_{\alpha\beta}(\mathbf{r}_1, t_1; \mathbf{r}_2, t_2) = \delta(\mathbf{r}_1 - \mathbf{r}_2)\delta(t_1 - t_2)\delta_{\alpha,\beta}.$$

For single-particle potentials in the Hamiltonian it can be shown that the solution to this equation is found if

$$(2.56) \quad G_{\alpha\beta}(\mathbf{r}_1, t_1; \mathbf{r}_2, t_2) \equiv \frac{-i}{\hbar} \langle \hat{T} \hat{\Psi}_\alpha(\mathbf{r}_1, t_1) \hat{\Psi}_\beta^\dagger(\mathbf{r}_2, t_2) \rangle$$

where the $\hat{\Psi}$'s are the field operators (Eq. 2.16) in the Heisenberg representation, \hat{T} is a time ordering operator, and the brackets refer to a statistical mechanically weighted expectation value. As can be seen from its form, the Green's function is a generalized correlation function relating the destruction of particles at (\mathbf{r}_1, t_1) to their creation at (\mathbf{r}_2, t_2) . Hence, it is closely related to the transmission coefficients T of our previous Hamiltonians.

For the two particle potential that binds the Cooper pairs in a superconductor, it was shown by Gor'kov [46] that Eq. 2.55 can be somewhat preserved by defining two “anomalous” Green's functions

$$(2.57) \quad F_{\alpha\beta}(\mathbf{r}_1, t_1; \mathbf{r}_2, t_2) \equiv \langle \hat{T} \hat{\Psi}_\alpha(\mathbf{r}_1, t_1) \hat{\Psi}_\beta(\mathbf{r}_2, t_2) \rangle$$

$$(2.58) \quad F_{\alpha\beta}^\dagger(\mathbf{r}_1, t_1; \mathbf{r}_2, t_2) \equiv \langle \hat{T} \hat{\Psi}_\alpha^\dagger(\mathbf{r}_1, t_1) \hat{\Psi}_\beta^\dagger(\mathbf{r}_2, t_2) \rangle$$

which are used to satisfy

$$(2.59) \quad \left(i\hbar \frac{\partial}{\partial t} - \hat{H} \right) G_{\alpha\beta}(\mathbf{r}_1, t_1; \mathbf{r}_2, t_2) + \Delta_{\alpha,\gamma}(\mathbf{r}_1, t_1) F_{\gamma\beta}^\dagger(\mathbf{r}_1, t_1; \mathbf{r}_2, t_2) = \delta(\mathbf{r}_1 - \mathbf{r}_2) \delta(t_1 - t_2) \delta_{\alpha,\beta}.$$

and related equations. We note that the anomalous Green's function of Eq. 2.57 is akin to the spatial form of the condensate wavefunction derived in Eq. 2.18, and, as such, is a measure of the strength of the superconductivity, disappearing in the fully normal metal. It can also be easily related to the position, time, and spin-dependent gap energy

$$(2.60) \quad \Delta_{\alpha,\gamma}(\mathbf{r}, t) = V F_{\alpha\beta}(\mathbf{r}, t; \mathbf{r}, t)$$

where V is a measure of the strength of the pairing interaction.

The statistical mechanical average that must be performed to calculate the Green's function can be accomplished using one of two equivalent techniques. In the Keldysh formalism [47], linear combinations of Eq. 2.59 and related equations are used to create a new ‘‘Keldysh’’ Green's function from which most relevant physical quantities can be extracted. In the Matsubara formulation [48], the formal similarity between the Hamiltonian propagator and the Boltzmann statistical weight is exploited by allowing the real time functions to be analytically continued to an imaginary time axis which is related to the temperature of the system. While both formalisms are can be shown to produce equivalent results [49], most contemporary theory uses the former technique, which is both more physically intuitive and more suited for handling nonequilibrium systems.

The strength of the Green's function formalism is its ability to incorporate perturbing potentials through diagrammatically calculated expansions. Of particular interest to the

experiments of this thesis is the case of dirty or diffusive superconductors, where there are a large number of elastic scattering centers within the material. Using a model of the single electron scattering process and an expansion in the Green's functions one can perform an ensemble average over the possible configurations of these scatters for a given scatterer density. There are two additional averages that can also be performed when modeling the aluminum used in our experiments. The fact that relevant changes to the behavior of the superconductor occur only over the correlation length scale ξ_S , which is several hundred nanometers, means that processes which occur on much shorter length scales can be averaged out of the Green's functions. Since the electronic wavefunctions of interest will have some oscillatory part similar to $e^{i\mathbf{k}\cdot\mathbf{r}}$ with $|\mathbf{k}| \sim k_F$, they will undergo phase oscillations on length scales $k_F^{-1} \sim \text{\AA}$, much shorter than ξ_S . This observation justifies averaging over the magnitude of \mathbf{k} , though not over its direction. However, since our dirty aluminum typically has an electronic mean free path l_e of tens of nanometers, an order of magnitude shorter than ξ_S , the directional average is justified as well. The magnitude averaging was pioneered by G. Eilenberger [50], the directional averaging by K. D. Usadel [51].

With some of the established concepts and techniques regarding superconductors now in hand, we proceed in the next chapter to examine two processes involving superconductivity that have only recently begun to be investigated.

CHAPTER 3

Crossed Andreev Reflection and Elastic Cotunneling

In this chapter we examine the case when two normal metal (N) or ferromagnet (F) probes are placed on a superconductor (S) within a superconducting coherence length of each other. Due to the correlations over this length scale between electrons constituting the Cooper pairs of the condensate wavefunction, it will prove to be theoretically possible to couple the electrons in the spatially separate probes through the novel processes of crossed Andreev reflection and elastic cotunneling. We begin by examining some of the early theory dealing with these processes, proceed to review the initial experiments searching for them, and conclude by looking at more recent theoretical developments. As the experiments of Chapter 5 will involve normal probes, diffusive metals, and transparent interfaces between the probes and superconductor, we keep these limits in mind throughout.

3.1. Early Theory

To write down a Hamiltonian for the case of two normal metal or ferromagnet probes on a superconductor we can simply double the Eq. 2.47 Hamiltonian we used for a single NS interface in Section 2.5:

$$(3.1) \quad \hat{H}_{NSN} = \sum_{\mathbf{k}, \mathbf{p}, \mathbf{q}, \alpha, \beta} T_{\mathbf{k}\mathbf{p}\alpha}^A \hat{c}_{\mathbf{k}\alpha}^\dagger \hat{d}_{\mathbf{p}\alpha} + T_{\mathbf{k}\mathbf{p}\alpha}^{A\dagger} \hat{d}_{\mathbf{p}\alpha}^\dagger \hat{c}_{\mathbf{k}\alpha} + T_{\mathbf{q}\mathbf{p}\beta}^B \hat{c}_{\mathbf{q}\beta}^\dagger \hat{d}_{\mathbf{p}\beta} + T_{\mathbf{q}\mathbf{p}\beta}^{B\dagger} \hat{c}_{\mathbf{p}\beta}^\dagger \hat{c}_{\mathbf{q}\beta},$$

where the \hat{c} 's operate in the normal metals and the \hat{d} 's in the superconductor, with indices \mathbf{k} for the first normal metal at NS interface A , \mathbf{q} for the second at interface B , and \mathbf{p} for the superconductor. We have made the assumption that spin is preserved for all processes. Again, first order transmission is limited to quasiparticle creation in the superconductor, so if we are interested in processes involving electrons with subgap energies we must proceed to a second order Fermi golden rule calculation (Eq. 2.50). As before we uncover Andreev processes for each interface, but there are two additional types of terms that may be non-zero, involving matrix elements such as

$$(3.2) \quad \langle F | T_{\mathbf{k}\mathbf{p}\uparrow}^{A\dagger} \hat{d}_{\mathbf{p}\uparrow}^\dagger \hat{c}_{\mathbf{k}\uparrow} | M \rangle \langle M | T_{\mathbf{q}-\mathbf{p}\downarrow}^{B\dagger} \hat{d}_{-\mathbf{p}\downarrow}^\dagger \hat{c}_{\mathbf{q}\downarrow} | I \rangle$$

and

$$(3.3) \quad \langle F | T_{\mathbf{k}\mathbf{p}\uparrow}^A \hat{c}_{\mathbf{k}\uparrow}^\dagger \hat{d}_{\mathbf{p}\uparrow} | M \rangle \langle M | T_{\mathbf{q}\mathbf{p}\uparrow}^{B\dagger} \hat{d}_{\mathbf{p}\uparrow}^\dagger \hat{c}_{\mathbf{q}\uparrow} | I \rangle.$$

The first process is nearly identical to the Andreev reflection one of Eq. 2.51. As before, an incoming electron from the second lead enters the superconductor creating a Cooper pair, only now, the retroreflected hole occurs in the first lead. This nonlocal, or crossed Andreev reflection (CAR) is shown in Fig. 3.1(A) and (C). In the second process, the incoming electron from the second lead undergoes a tunneling to the first lead that is mediated by the pair correlation in the superconductor. This elastic cotunneling (EC) is shown in Fig. 3.1(A) and (B).

From these matrix elements we can foreshadow some of the general themes found in the more detailed theoretical calculations discussed below. First, for a positive current

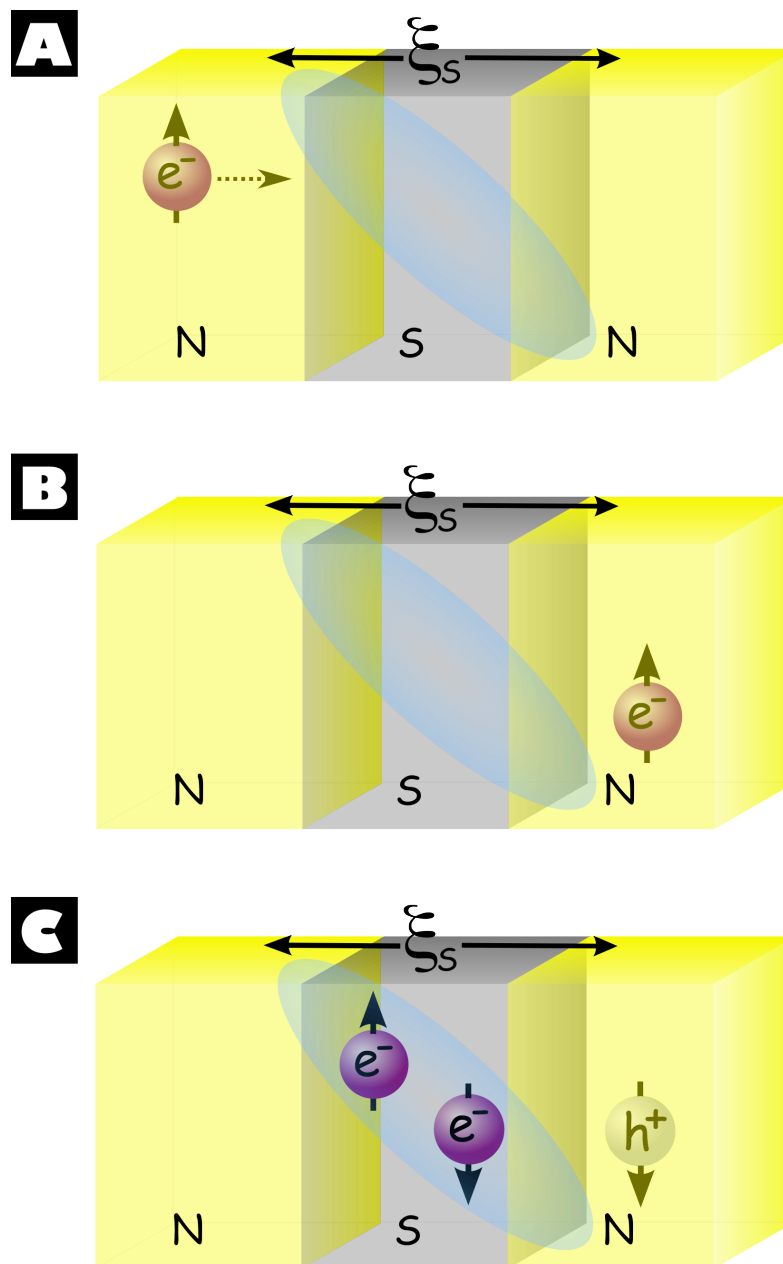


Figure 3.1. (A) When two normal metals N are placed within a superconducting coherence length ξ_S of each other on a superconductor S, there are two phase coherent processes for an electron incident from one normal metal towards the superconductor not possible when there is only a single NS interface: (B) The electron can undergo a condensate-mediated elastic cotunneling (EC) into the other normal metal (C) The electron can form a Cooper pair with an electron from the other normal metal, producing a nonlocal or crossed Andreev reflection (CAR) in this metal.

traveling from one normal metal lead to the superconductor, the retroreflection of the CAR process will produce a negative voltage in the second lead, while the tunneling of the EC process will produce a positive voltage in the second lead. Second, as both processes rely on pair correlations in the superconductor, the probability of their occurrence will be negligible if the probes are separated by distances much greater than ξ_S . Third, in the simplest approximation, where all the transmission coefficients are equal, the $|T_{\uparrow}^{A\dagger}T_{\downarrow}^{B\dagger}|^2$ amplitude for CAR and $|T_{\uparrow}^AT_{\downarrow}^{B\dagger}|^2$ amplitude for EC will be equal, and thus the two processes will cancel each other out. Fourth, an obvious way to avoid this cancelation is to make the transmission coefficients have a strong spin-dependence. This dependence can be easily arranged in principle by using ferromagnetic probes whose relative polarity can be flipped. If they are anti-parallel CAR should dominate, while EC should dominate if they are parallel. Fifth, as CAR involves operators of the form $\hat{d}^{\dagger}\hat{d}^{\dagger}$ and EC of the form $\hat{d}\hat{d}^{\dagger}$, more detailed calculations of the former process will be governed by terms involving the anomalous Green's functions F of Eq. 2.57 while the latter will be governed by terms involving the regular Green's function G of Eq. 2.56.

To our knowledge, the first published work on EC and CAR (though it did not refer to them as such) was by J.M. Byers and M. E. Flatté [52]. They envisioned the “conceptually straightforward, but impractical” experiment of having two scanning tunneling probes travel along the surface of a superconductor, separated by a variable distance R . Their main focus was examining the anisotropic nature of the condensate wavefunction presumed to exist in high temperature superconductors. Using a Hamiltonian similar to Eq. 3.1 and the same second order transmission method we used to identify our matrix elements of interest, Byers and Flatté related the nonlocal differential conductance (i. e.

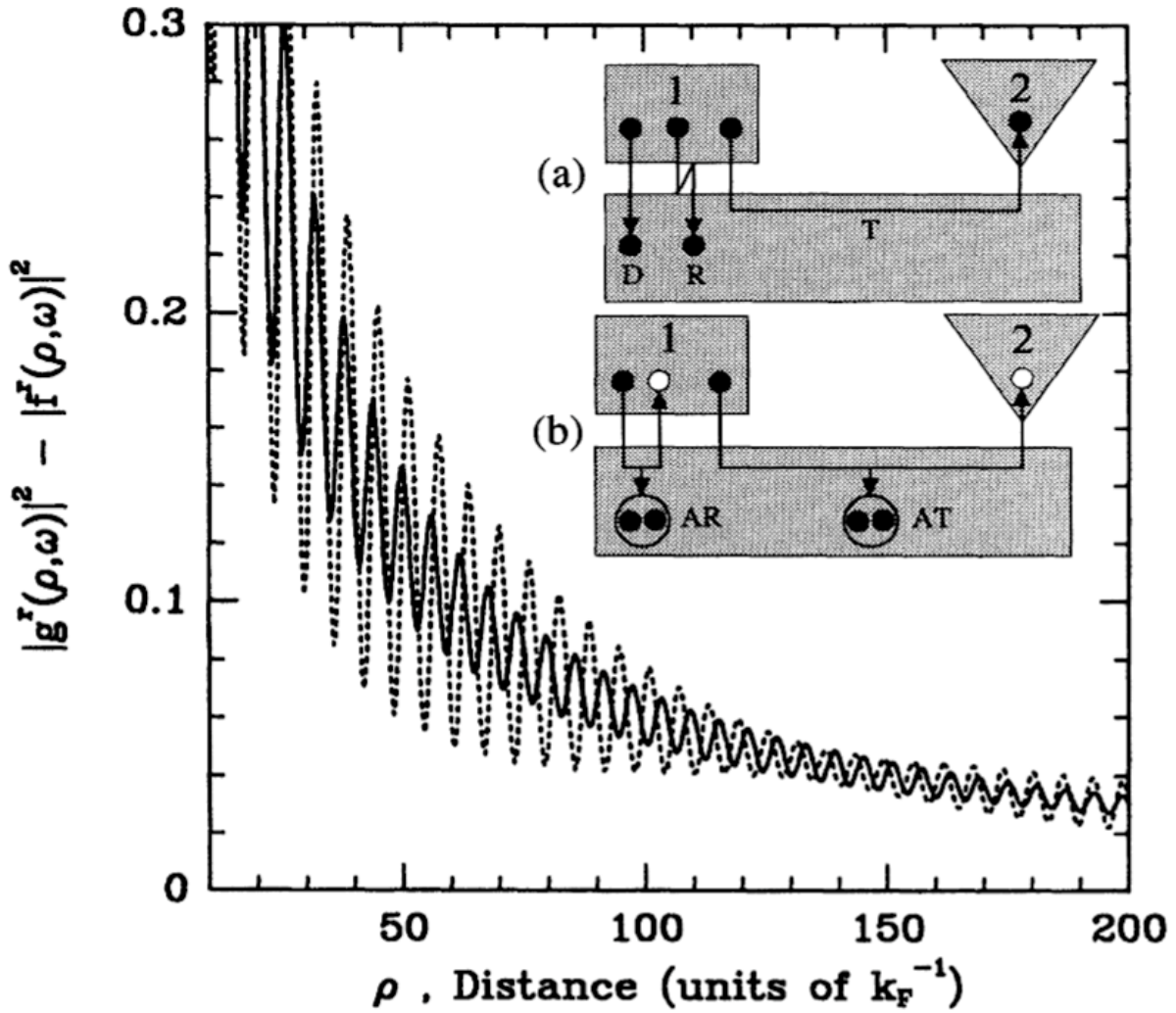


Figure 3.2. Calculation by Byers and Flatté for EC (a) and CAR (b) showing the nonlocal differential conductance amplitude due to these processes as a function of the spatial separation between the two probes. The solid line is for a normal metal substrate, the dotted line for a superconducting one. [Figure from [52]]

the change in current on one probe when the voltage on the other is changed) due to EC to a variant of G and that due to CAR to a variant of F . The calculated sum of these as a function of the separation between probes is shown in the dotted line of Fig. 3.2.

Though they explicitly noted that EC and CAR should only be possible if the probes are within a few ballistic superconducting coherence lengths ξ_0 of each other, this length scale does not enter into their calculation, where they assumed the transmission probabilities within the scanned substrate to be position independent. The decay in the nonlocal signal is due to a $1/R$ factor based on the geometry of their model. They also assumed that transport in their superconductor is ballistic over the probe separation used, which accounts for the fast $\sim k_F^{-1}$ oscillations which would be averaged out for a diffusive sample modeled with a quasi-classical treatment. While neither a realistic experiment or an accurate model, the work of Byers and Flatté has been cited by most subsequent investigations into EC and CAR for its recognition of the potential existence of these two processes.

G. Deutscher and D. Feinberg were the first to note that the use of ferromagnetic probes, with antiparallel polarities would be conducive to CAR [53]. Using a generalized version of the BTK formalism discussed in Section 2.6, which allowed for nonlocal A probabilities for CAR. Deutscher and Feinberg predicted the possibility of seeing a negative voltage on one probe when a positive current is sent into the superconductor from the other. While examining a simple model that did not include the possibility of EC, their work had the virtue of identifying a novel signal that might be observable using a device that was lithographically realizable. They were also the first to explicitly recognize the phase coherent nature of such a nonlocal process. The use of ferromagnetic probes has been investigated in a number of subsequent theoretical works [54, 55, 56, 57], but we will here focus on the development of the theory where normal probes, or probes of variable polarization that can be taken to be zero, are examined.

G. Falci with his collaborators Feinberg and F. W. J. Hekking tackled the problem with normal probes using methods similar to Byers and Flatté, but allowed for probes with multiple conductance channels and started from a more realistic model of the transmission probabilities [58]. Falci *et. al.* used Eq. 3.1 as their tunneling Hamiltonian and proceeded with the second order calculation outlined above to calculate the single channel conductance magnitudes for EC and CAR

$$(3.4) \quad \begin{pmatrix} G_{EC} \\ G_{CAR} \end{pmatrix} \approx A |T_A d_A|^2 |T_B d_B|^2 \frac{e^{-2R/\pi\xi_0}}{(k_F R)^2} \begin{pmatrix} \cos^2(k_F R) \\ \cos^2(k_F R) \end{pmatrix}.$$

Here A is dependent on the density of states and fundamental constants, T_A and T_B are the local tunneling probabilities for the two interfaces, d_A and d_B are the size of the probe contacts (assumed to be $\sim k_F^{-1}$ for a single channel), and R is the distance between them. The oscillatory character of the processes, due to the assumption of a ballistic superconductor, average away with no interference effects if the probes are assumed to be large enough to contain multiple, independent conductance channels. There are three important features of Eq. 3.4 to note. First, there is now an explicit exponentially decaying spatial dependence of EC and CAR on the ballistic superconducting coherence length ξ_0 . Second, there is a $1/R^2$ geometrical dependence which provides additional attenuation as the distance between the probes increases. Third, for a multiple channel lead configurations, the magnitude of the two processes are approximately equal, and so, since they produce nonlocal voltages of opposite signs, they will have zero net effect for normal metal probes.

A similar result was found by R. Mélin and Feinberg using the Keldysh Green's function technique [59]. While the second order technique of Byers and Flatté and Falci *et al.* is appropriate only if the Hamiltonian Eq. 3.1 is a small correction, such as for strong tunneling interfaces, the Keldysh technique allowed Mélin and Feinberg to examine the transparent probe contact regime in which they also found an exact cancelation of EC and CAR. It should be noted, though, that their transparent model still regarded the properties of the normal metals and superconductor as distinct and equivalent to their bulk values, i. e. there was no gradual crossover from the superconducting to the normal state at the interfaces, such as would be seen in a Bogoliubov-De Gennes treatment of transparent contacts.

The extension of the works discussed above on ballistic systems to the dirty, diffusive limit was provided independently by Feinberg [60] and N. M. Chtchelkatchev [61] who showed that the spatial dependence of Eq. 3.4 was altered as follows

$$(3.5) \quad \frac{e^{-2R/\pi\xi_0}}{(k_F R)^2} \quad \longrightarrow \quad \frac{e^{-R/\xi_S}}{(k_F R)(k_F l_e)},$$

where $\xi_S \sim \sqrt{l_e \xi_0}$ is the superconducting coherence length in the dirty limit. In addition to a difference in the exponential decay, the major alteration is the reduction of the $1/R^2$ geometrical factor to $1/R$, making observation of EC and CAR possible over longer probe separation distances for diffusive systems. Feinberg also noted that this geometrical factor could be further altered depending on the spatial extent of the superconductor. For a superconductor with one dimension smaller than l_e , he predicted that the geometrical factor goes as $1/\sqrt{R}$ for $R > \xi_S$ and $-\ln(R/\xi_S)$ for $R < \xi_S$. For the Al superconductors we use, both the thickness and width are $\sim 2l_E$, which likely puts the geometrical factor

at something slightly weaker than $1/R$. For simplicity we will assume only the exponential dependence, keeping in mind that there is probably an additional weak geometrical attenuation as well.

3.2. Prior Experimental Work

After the early theoretical predictions were set forth, the first two experiments designed to look for EC and CAR were reported. In the first, as envisioned by Deutscher and Feinberg, two ferromagnetic probes were placed on a superconductor to look for enhancement and suppression of EC and CAR as their relative polarities were switched. In the second, nonlocal effects, primarily as a function of current injected into the superconductor, were looked for using normal probes. The first experiment is similar to the ones we present in Chapter 5 in that it used transparent interfaces between the probes and the superconductor, but differs in that it used ferromagnetic probes. The second experiment differs from ours in that it used tunneling barriers between the probes and the superconductor, but is similar in that it uses normal metal probes. Both experiments, like ours, used diffusive metals.

A sample used in the ferromagnetic probe experiment of D. Beckmann *et. al.* is shown in Fig. 3.3(A) [62]. Several Fe probes are placed on an Al superconductor separated by a few hundred nanometers each, approximately the distance corresponding to ξ_S . Due to their different sizes the ferromagnets have different coercivities and so could be oriented either parallel or anti-parallel using an external field. A small, 50 nA measurement current I_A was sent across one of the FS interfaces and the voltage U_B relative to the superconductor potential was measured on a second ferromagnetic probe. Since no current crossed

the second probe this was a strictly nonlocal resistance measurement. Fig. 3.3(B) shows their main result, nonlocal resistance as a function of temperature for the two different magnetic orientations.

The dominant feature of this curve is the large peak which appears at the 1.2 K superconducting T_c of Al, and then decays with temperature. From its sign and temperature dependence, this can be identified as a charge imbalance effect (see Section 2.3) which is the dominant process for above-gap electrons entering the superconductor, particularly in the transparent interface limit. The charge imbalance was measured with the nonlocal probes since one was ferromagnetic, thus equilibrating with the out-of-equilibrium quasiparticle chemical potential, while the other was at the equilibrium condensate potential.

As the charge imbalance signal decayed, a difference was revealed in the nonlocal resistance for the two different magnetic configurations. For a parallel orientation the resistance was higher than for the antiparallel orientation. Since the CAR effect should be enhanced for the antiparallel configuration, and the effect of CAR on a current entering the superconductor from one lead should be a negative voltage on the other, the decrease seen is consistent with an increase in CAR (or, similarly, a decrease in the positive-voltage producing EC). While the resistance difference also exists when the superconductor is in the normal state due to the spin valve effect [63, 64] (as shown explicitly in the inset of Fig. 3.3(B)), the measured distance dependence of this effect was shown to be different than the resistance change in the superconducting state, which disappeared on a length scale comparable to ξ_S .

This experiment conformed to the theory at the time, insofar as it showed a polarity-dependent resistance change, decaying on a scale $\sim \xi_S$, and consistent with EC and

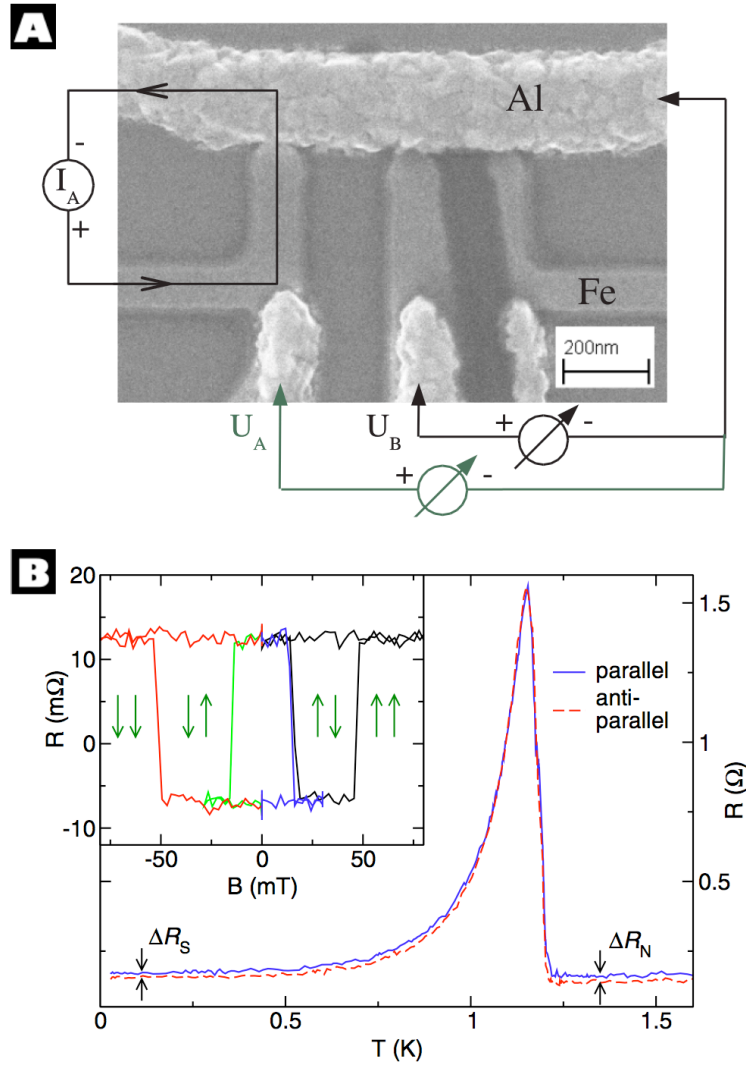


Figure 3.3. (A) Picture of a sample measured in Ref. [62] composed of an superconducting Al strip and several ferromagnetic Fe contacts. A small AC measurement current was sent across the far left lead and a nonlocal voltage was measured on the U_B and other leads referenced to the superconductor potential. The relative magnetic orientation between the lead across which current was sent and the lead on which voltage was measured could be switched with an external field. (B) Nonlocal voltage as a function of temperature. The nonlocal signal was dominated by a charge imbalance peak which decayed as the temperature was reduced. At low temperatures there was a difference between the signal depending upon whether the ferromagnetic leads were parallel or anti-parallel. The inset shows a close-up of this resistance difference for the normal state as the magnetic orientation was changed by the external field.[Figures from [62]]

CAR in its direction. It did not show, as had been hoped, an absolute negative nonlocal resistance in the antiparallel CAR configuration and a positive nonlocal resistance in the parallel EC configuration. There also appeared the difficulty, not explicitly anticipated in the theoretical works, of the large charge imbalance background seen when using clean interfaces. Indeed, if not for the polarity-dependence, it would be difficult to separate out the low-temperature nonlocal voltages in Fig. 3.3(B) due to EC and CAR from the background.

The ensuing experiment of Russo *et. al.* [65] employed a similar nonlocal measurement technique to Beckmann's, but the sample, shown schematically in Fig. 3.4(A), differed in three significant ways: it used normal metal probes, there were oxide tunnel barriers between the probes and superconductor, and their contacts are extended layers rather than small lateral interfaces. As shown in Fig. 3.4(B), a DC bias current and a $1 \mu\text{A}$ AC measurement current were sent from one normal probe (Al above its superconducting T_c) into the superconductor (Nb, with a ξ_S estimated to be 10 to 15 nm). The voltage drop of the DC part of this current across the J_1 tunnel barrier was recorded as " V_{dc} ". The nonlocal AC voltage at the measurement frequency between the second normal probe and the superconductor was measured and recorded as " V_{ac}^{nl} ".

The main results of Russo *et. al.* are shown in Fig. 3.4(C), which presents data from samples with three different S-layer thicknesses, i. e. three different normal probe separations. For the samples with close probe separations, there was a nonlocal signal which was positive at low DC voltages across the local junction, became negative at higher DC voltage biases, and then disappeared. From separate local tunneling measurements of the voltage corresponding to the gap energy, this signal was seen to be below the gap. In fact

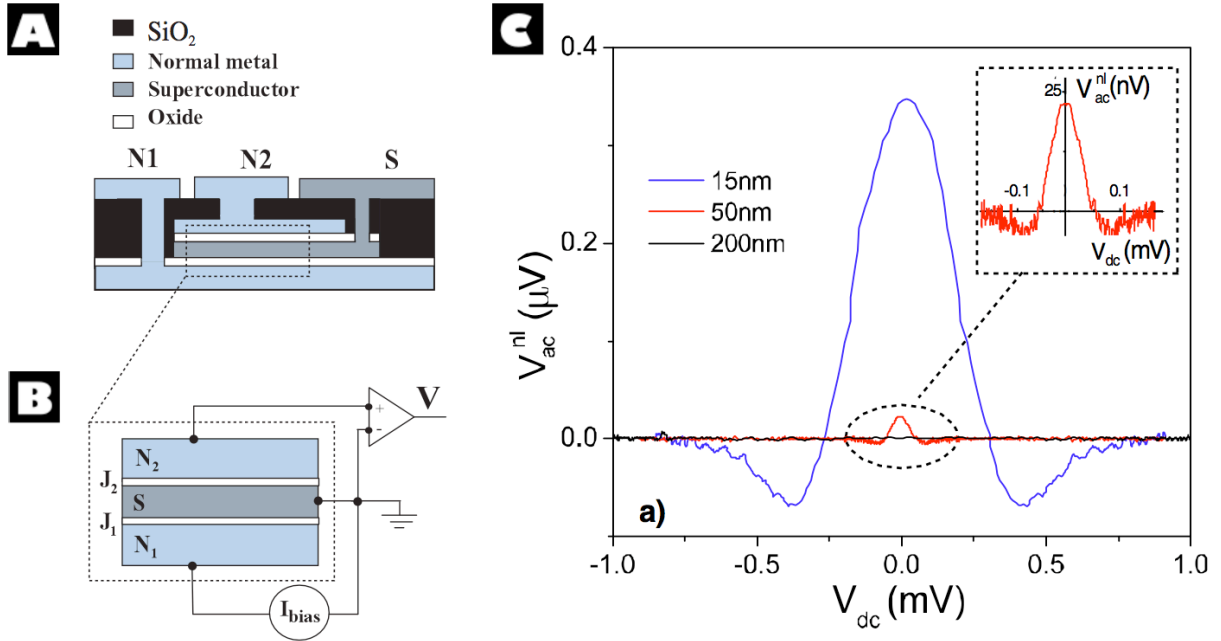


Figure 3.4. (A) Schematic of a sample measured in Ref. [65]. Nb was used as the superconductor and Al as the normal metal, with measurements taken above 1.7 K. (B) The measurement configuration used a DC current bias and AC measurement current. The nonlocal voltage was measured at the AC current frequency. (C) Nonlocal differential voltage as a function of the DC voltage across the barrier that the current is sent through. A signal was observed that was below the gap energy and decreased with separation between the two normal metals.[Figures from [65]]

the gap increased as the DC voltage range of the signal decreased with increasing probe separation. Russo *et. al.* noted that this voltage range for the two thicknesses where a nonlocal signal was observed was comparable in each case to the Thouless energy (Eq. 2.46) with the length scale set by the thickness of the superconductor.

This experiment showed several features that are consistent with EC and CAR. A nonlocal signal was observed on a probe located within roughly ξ_S of a probe injecting current into the superconductor at energies below the gap, and the signal disappeared as the distance between the probes increased to values much larger than ξ_S . However,

there are quite a few surprises in the experiment given the theoretical predictions at the time. First, and foremost, the theoretical models, which seemed most applicable to the tunnel junction regime that the experiment operated in, all predicted that the signals from EC and CAR should exactly cancel each other out when using normal probes. Second, it was expected that for a given current from one probe, the second one should see a nonlocal voltage which decayed with distance. In the experiment of Russo *et. al.* the decay depended not only on distance, but heavily on what injection current (or voltage) was being used. There was also no consideration in the theory of any dependence on the Thouless energy corresponding to the distance between the probes.

There is one criticism of the work of Russo *et. al.* regarding the interpretation of their data that should be mentioned, particularly as it has led to some confusion among subsequent theoretical papers trying to interpret it. The experimenters claimed that the positive part of the nonlocal signal they observe is due to EC and the negative part to CAR. This claim seems to be based on the expectation that for a positive current injected from a probe into the superconductor a positive nonlocal voltage would correspond to EC being the dominant process, while a negative voltage would correspond to CAR being the dominant process. This is not, though, what the authors measured. They injected both an AC and DC current and measured the nonlocal voltage at the AC frequency, which, assuming the AC modulation is much smaller than the DC current, corresponds to measuring the *differential* nonlocal voltage for a given DC injection current. An observation of a negative nonlocal differential voltage for a positive injection current does not necessarily imply that such a current created a negative nonlocal voltage consistent with CAR. To construct what nonlocal voltage is seen for a given local bias, one would have

to integrate the curves of Fig. 3.4(C) and make the, physically reasonable, assumption that for zero local bias there is zero nonlocal voltage. Doing so would show that Russo *et. al.* always observed a positive nonlocal voltage for a positive injection current and a negative nonlocal voltage for a negative injection current, nonlocal voltages consistent with a dominant EC process in all cases.

Having reviewed these experiments, we examine some of the more recent theoretical modifications and approaches produced in response to them.

3.3. Recent Theory

Shortly after the results of Beckmann *et. al.* were announced, Mélin and Feinberg returned to the problem of how to model transparent interfaces between the superconductor and probes [66]. While their use of the Keldysh method in their previous calculation [59] had allowed them to examine the transparent limit, they had not supposed any alteration of the Green’s functions for the probes and superconductor due to their mutual influence near the interface. Here, they posited a “dressing” of these Green’s functions due to multiple regular Andreev reflections at each interface. By using an expansion in $1/k_F R$, which is a small parameter for the above experiments (as well as our own), they could allow the possibility of transport processes that went through multiple local Andreev reflections, while still being limited to a single nonlocal Andreev reflection or cotunneling to the remote probe. These assumptions broke the earlier calculated symmetries between EC and CAR allowing for a net nonlocal conductance for normal metal probes:

$$(3.6) \quad G = -A \frac{e^{-R/\xi_s}}{(k_F R)(k_F l_e)} \frac{\tau^8}{(4 + \tau^4)^2}.$$

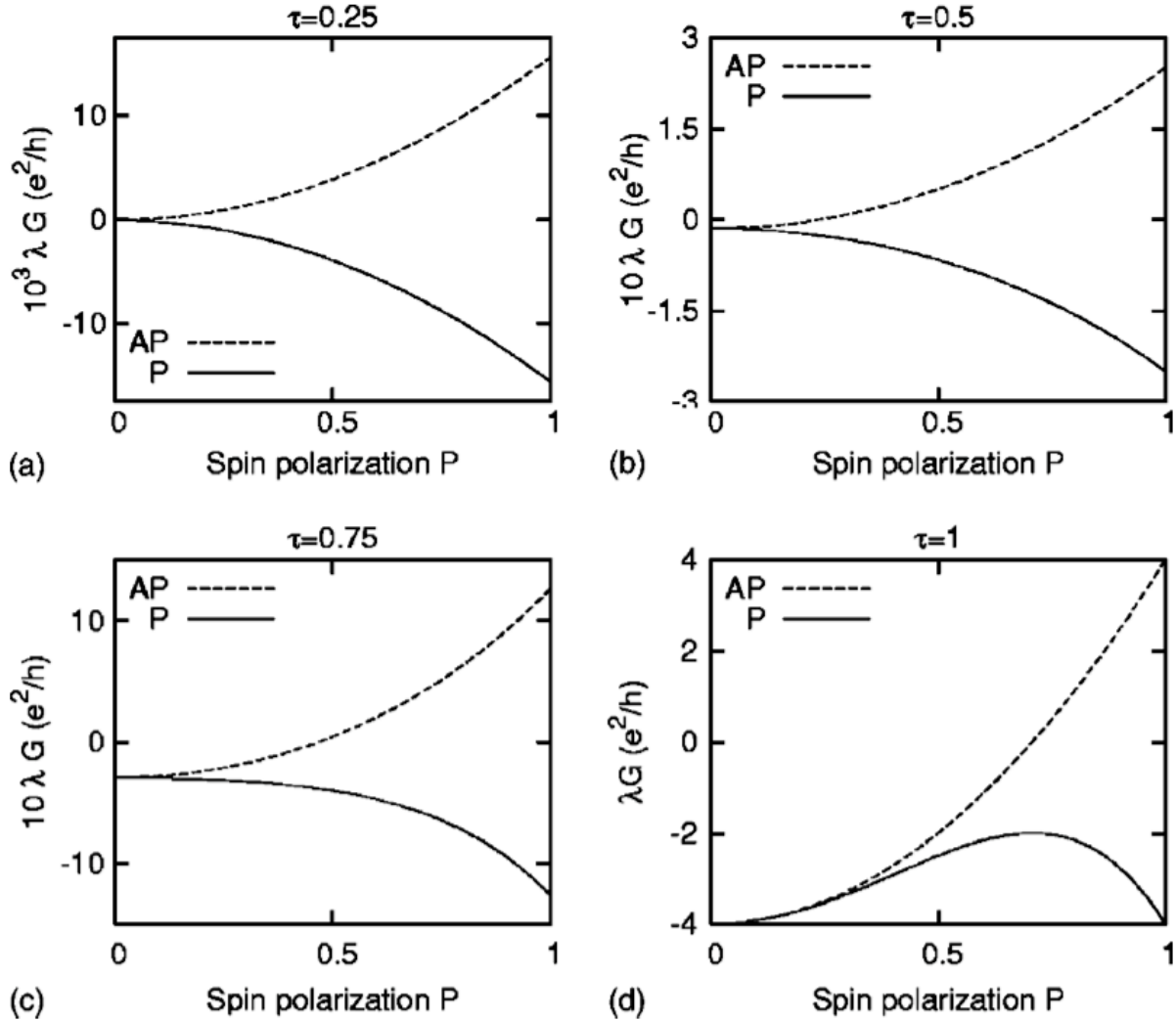


Figure 3.5. Mélin and Feinberg prediction of the total nonlocal conductance for different polarizations P and polarities of probes with four different interface transparencies τ . For current injected from one probe into the superconductor, a negative G corresponds to a positive voltage on the nonlocal probe. [Figure from [66]]

where A is a positive constant and τ is a transparency parameter that varies from 0, for perfect tunneling contacts, to 1, for perfectly transparent contacts. Due to their sign conventions, a negative G corresponds to observing a positive nonlocal voltage when current is injected into the superconductor from the local probe. Thus, for any normal contacts

that are even modestly transparent, EC should dominate over CAR. A plot of the total conductance that includes the possibility of ferromagnetic probes with polarization P in either a parallel or anti-parallel configuration is shown in Fig. 3.5 for four different transparencies. Note that the sample measured by Beckmann *et. al.* corresponds approximately to perfectly transparent contacts ($\tau = 1$) and a polarization of 0.5. In this case the plot predicts the sign of the nonlocal voltage is positive for a positive injected current with its magnitude reduced only slightly when the probes are antiparallel, which is consistent with the data of Fig. 3.3(B). Though this paper was published before the work of Russo *et. al.* it also predicted the sign of their observed nonlocal signal, provided their tunneling barriers are not perfect, though it does not predict any dependence on the correlation energy.

This dependence was directly addressed by Morten *et. al.* [67] who took a different tack attempting to model the alteration of the Green's functions when the probe contacts are transparent. They used a circuit theory [68] model to derive the energy dependence and relative strengths of EC and CAR for a number of situations. As shown in their model (Fig. 3.6(A)), circuit theory uses the quasiclassical Green's functions, which take on their bulk values appropriate for the normal and superconducting reservoirs N_1 , N_2 , and S . The reservoirs are connected to a cavity c in which the Green's functions may take on a nonequilibrium form. Connecting the reservoirs and cavity are sets of transmission probabilities T_n^i , which can be tuned not only to govern transmissions of electrons, but the flow of correlations between them. These flow probabilities establish a set of "Kirchoff's laws" which can be solved to determine the nonequilibrium behavior.

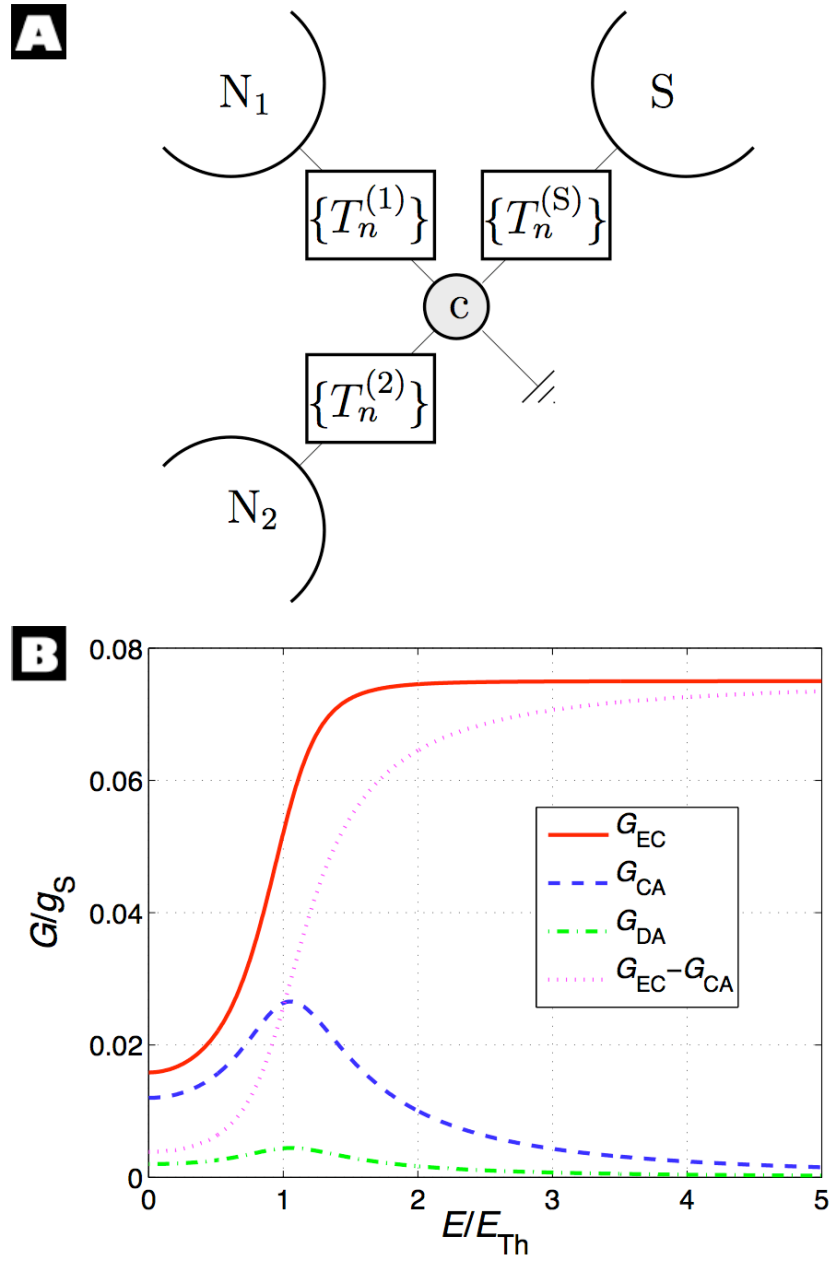


Figure 3.6. (A) Drawing of the circuit theory model used by Morten *et al.* (B) The model's prediction of the conductance for the EC, CAR, and direct Andreev reflection (DA), along with the total nonlocal conductance ($G_{EC} - G_{CA}$) in the case of transparent contacts between all the N and S reservoirs and the cavity c . [Figure from [66]]

Fig. 3.6(B) shows the results of a calculation for the nonlocal conductances when all the transmissions are high, similar to the types of interfaces we study in Chapter 5. Morten *et. al.* found that EC is larger than CAR for all electron energies, a result replicated for all other simulated transparencies. In addition, their calculations revealed a Thouless energy (E_{Th}) dependence on the relative strengths of the transport processes, where the length scale governing the Thouless energy is related to the size of the cavity. Although the authors showed that in their model the EC and CAR processes do not exactly cancel when normal probes are used, they lamented that they do not observe the negative nonlocal signal of Russo *et. al.* in their simulations. However, as we have discussed above, this signal is actually still indicative of the dominance of EC over CAR, so the findings of Morten *et. al.* are consistent in their sign with these measurements. It is doubtful, though, that the results of these theorists could replicate the functional form of the nonlocal signal seen by Russo *et. al.*

Finally, we review the work of Yeyati *et. al.* [69] who attempted to explicitly model the experimental set-up of Russo *et. al.* These authors' solution to identifying a process that breaks the exact cancellation of EC and CAR found in the early theories was to consider the collective electronic excitations that could be present between the normal metal probes. They modeled the space between the tunnel junctions occupied by the superconductor as a cavity capable of supporting electromagnetic modes that can be of a symmetric or antisymmetric spatial form. Adding these modes into the Keldysh formalism, Yeyati *et. al.* demonstrated that each type of mode could curtail either EC or CAR depending on its symmetry. By calculating at what local probe biases the different types of modes are created for the geometries used by Russo *et. al.*, they argued that

the voltage crossover observed in this experiment could be accounted for by the changing symmetries of the induced modes. While not evaluating the contents of this theory, or whether these modes do play a significant role in effecting EC and CAR, we note that the predicted crossover to a CAR dominant regime at higher current injection into the superconductor does not match the data of the experiment they are attempting to model when it is properly interpreted.

To conclude our tour of the current state of theoretical understanding and experimental observations of EC and CAR, we recall some of the key points to be kept in mind when we present the results of our own investigations in Chapter 5. First, EC and CAR are phase coherent processes that can occur when two probes are placed on a superconductor. Measured relative to the potential of the superconductor, EC should produce a positive voltage on a nonlocal probe when current is injected into the superconductor from the other probe, while CAR should produce a negative voltage. Second, the signals produced by these processes should exponentially decay as the distance between the probes is increased on a length scale set by the superconducting coherence length ξ_S . There is also an additional geometrical decay factor which may be as strong as $1/R$ for diffusive systems. Third, while the initial theories predicted that EC and CAR should cancel each other when normal metal probes are used, recent work, trying to more accurately model cases with transparent interfaces, showed that EC should be the dominant process. Fourth, in the single experiment performed in transparent limit, the dominant nonlocal signal was due to charge imbalance.

CHAPTER 4

Experimental Fabrication and Measurement

As the fabrication and measurement techniques used in the experiments presented here follow procedures similar to those described in past theses from Northwestern's Mesoscopic Physics Group [72, 25, 73, 74, 75], much of what is only briefly outlined here can be found in more detail in the experimental techniques sections of these earlier works.¹ The more explicit descriptions in this chapter present either new techniques, refinements of previous techniques, or implementation and construction of new equipment.

As indicated in the previous chapters, our experimental work focuses on effects between normal metal probes placed on a superconductor and separated by lengths comparable to the superconducting coherence length ξ_S . Since this length does not typically exceed several hundred nanometers, at least three fabrication steps are required to produce devices to observe these effects. First, fashion a mesoscopic superconductor. Second, attach nanoscale normal metal probes to the superconductor. Third, connect the superconductor and normal probes to wires that can be handled by a macroscopic experimentalist. In practice these three layers of fabrication are performed in reverse order (top-down), with photolithography used for the third step and electron-beam lithography used for the first two.

Two other considerations related to the transport properties of the samples are also kept in mind when fabricating the samples: the interface between the normal metal

¹At the time of writing, all past theses can be found online at <http://www.nano.northwestern.edu>

probes and the superconductor should be as transparent as possible, and the normal metal coherence length l_ϕ should be as long as possible. Various steps in making the samples that effect and do not effect these properties are commented on in this chapter.

4.1. Substrates

Polished silicon substrates with a silicon oxide top layer are used as starting points for sample fabrication as they are widely available as wafers with near atomically flat insulating surfaces. While several different varieties were used, most of the samples measured are made on $\langle 100 \rangle$ oriented wafers with 300 nm SiO_2 top layers and unknown Si doping.

The substrates are cut by a hand-held diamond scriber from Ted Pella² and then cleaned to remove any residual surface contamination by i) Running a stream of 18 M Ω -cm resistivity distilled water over the sample for 1 minute. ii) Ultrasonicing it in isopropanol for 1 minute. iii) Ultrasonicing it in acetone for 3 minutes. iv) Ultrasonicing it in isopropanol for 1 minute to remove any acetone residue. v) Blow-drying the sample with a jet of pure nitrogen gas. While the additional cleaning step of subjecting the substrate to an oxygen plasma etch is sometimes performed [74], unless the substrate has been previously used or is noticeably contaminated this step is not necessary as long as the *in situ* etching described below is performed prior to metal evaporations.

4.2. Photolithography

The standard photolithographic pattern used to connect macroscopic and microscopic wires is shown at various magnifications in Fig. 4.1. The pattern consists of several square “pads” each composed of 22 Au on Ti films that taper from several hundred micrometers

²Ted Pella, Inc., Redding, CA, www.tedpella.com.

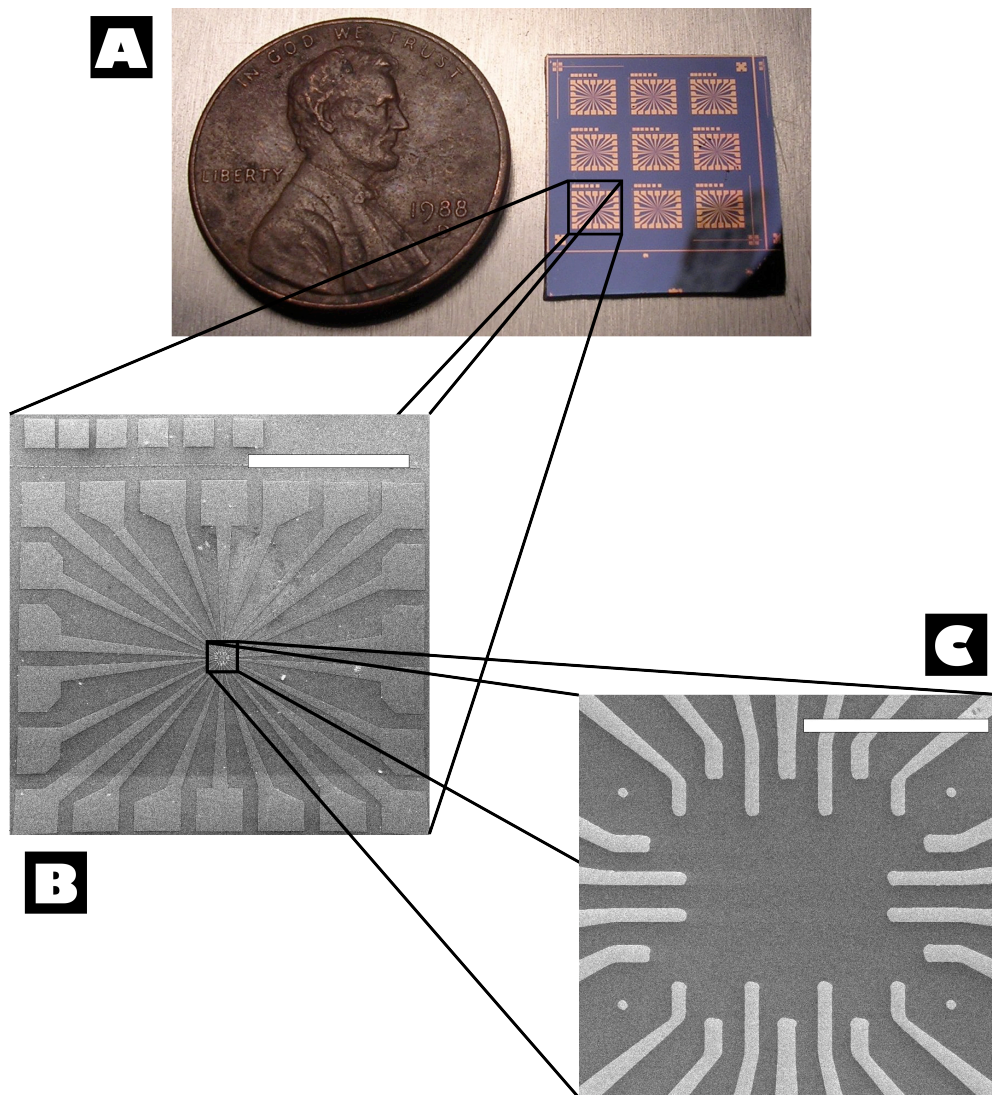


Figure 4.1. (A) Photo of a set of nine Au/Ti “pads” made photolithographically on a Si/SiO₂ substrate. (B) Scanning electron micrograph of a single pad. The pad consists of 22 separate films that narrow from several hundred micrometers to several micrometers in width as they taper from the edge of the pad to the center. The size bar is 1 mm. (C) Close-up of the center of a pad: the 22 leads terminate leaving a $\sim 1000 \mu\text{m}^2$ area for the critical part of the experiment to be fabricated and connected to the leads using electron-beam lithography. The four circles near the corners of the image are used to align the photolithographic layer to the subsequent layers, and may be sacrificially exposed during fabrication of these layers to tune the focus and alignment of the electron microscope. The size bar is $50 \mu\text{m}$.

at the edge to a few micrometers at the center. The central, $\sim 1000 \mu\text{m}^2$, area is left unpatterned for subsequent electron-beam lithography. After cleaning a substrate the following fabrication steps are performed:

- i) A clean glass pipet is used to coat the substrate with LOR 7B under-layer chemical from Microchem³.
- ii) The substrate is spun at 4,000 rpm for 30 seconds on a Headway Research⁴ spinner, the chemical forms a thin film with a nominal thickness of 600 nm.
- iii) The coated substrate is placed in a Pyrex dish and baked in a Clean 100 oven from Lab-Line Instruments⁵ for 45 minutes at 170° C to harden the under-layer.
- iv) The substrate is removed from the oven, coated with S1813 photoresist from Shipley⁶, and spun at 3,000 rpm for 40 seconds producing a film with a nominal thickness of 700 nm.
- v) The photoresist is baked at 110° C for 30 minutes.
- vi) After removal from the oven, the layered sample is put in a homemade mask aligner [74] where it is placed behind a Cr on quartz negative photomask pattern that has been commercially produced by Photronics⁷. Several different patterns are present on a single photomask, though the pattern shown in Fig. 4.1 is invariably used.

³Microchem Corp., Newton, MA, www.microchem.com.

⁴Headway Research, Inc., Garland, TX, www.headwayresearch.com.

⁵Lab-Line Instruments, Inc., Melrose Park, IL.

⁶Shipley Co., Inc., now a subsidiary of Rohm & Haas Co., Philadelphia, PA, www.rohmhaas.com.

⁷Photronics, Inc., Allen, TX, www.photronics.com.

- vii) The sample is exposed to light from a halogen lamp located ~ 1 m from the mask aligner for 7 minutes.
- viii) Upon removing the sample from the aligner, the exposed area of the wafer is washed away using a squeeze bottle to stream Rohm & Haas⁸ MF-319 photodeveloper across the surface of the sample for 55 seconds. The developer is then rinsed off of the surface using a stream of distilled water, and dried in a jet of nitrogen gas.
- ix) The patterned sample is loaded into one of the group's e-gun evaporators, typically the one constructed by José Aumentado [73], along with two evaporation crucibles containing 99.99% pure Au from Hoover & Strong⁹ and 99.95% pure Ti from ESPI¹⁰. Before closing the evaporation chamber, the sample is prepared for *in situ* etching by attaching the high voltage line to the sample stage and flushing the etch gas supply tubes with a flow of oxygen.
- x) The chamber is pumped to $\sim 10^{-6}$ Torr and the pumping is stopped. 40 mTorr of oxygen is introduced into the chamber and the 512 VAC power supply to the sample stage is turned on at maximum voltage for 25 seconds to subject the developed surface of the sample to cleaning by an O_2^+ plasma. The shutter in front of the sample is left open during the etching to reduce spark discharges on the sample.

⁸Rohm & Haas Co., Philadelphia, PA, www.rohmhaas.com.

⁹Hoover & Strong, Buffalo, NY, www.hooverandstrong.com.

¹⁰ESPI Metals, Ashland, OR, www.espi-metals.com.

- xi) After etching, the chamber is pumped for two minutes before evaporation is started. 4 nm of Ti (used to improve the surface adhesion of the subsequent Au deposition) is deposited at a rate of $\sim 1 \text{ \AA}/\text{sec}$, followed by 50 nm of Au at 10 - 20 $\text{\AA}/\text{sec}$. Before each evaporation, with the shutter shielding the sample, 4 nm of the metal is evaporated to remove its surface contaminants.
- xii) The chamber is pumped on for at least 20 minutes after the evaporations to allow time for the crucibles to cool. When the chamber is vented the sample is removed and placed in a beaker of acetone to begin lifting off the S1813 photoresist.
- xiii) The sample is soaked in acetone for 15 minutes, then rinsed in a stream of acetone until the bulk of the unpatterned metal is washed away. The sample is then ultrasonicated in acetone for 30 seconds to remove any additional unpatterned metal and resist, and then rinsed again in a flow of acetone, followed by a flow of isopropanol, and a drying jet of nitrogen gas.
- xiv) To remove the LOR 7B underlayer, the sample is soaked in a beaker containing 1165 Microposit remover from Rohm & Haas for 10 minutes. During this process the remover should be kept between 60° and 70° C by heating the beaker on a hot plate. The temperature of the remover should be constantly monitored as it has a flash point of 88° C . After

soaking, the sample is ultrasonicated for 30 seconds, rinsed in 1165 remover, rinsed in acetone, rinsed in isopropanol, and dried in the nitrogen gas jet.

Except for steps x-xii all procedures are carried out in a class 1000 clean room to minimize the sample's exposure to dirt that can interfere with the patterning process. Typically, one will make the maximum number of the 36 pads available on the photomask pattern. In order to spin chemicals on a substrate large enough to accommodate this number of pads, the usual vacuum mechanism on the spinner must be replaced with a larger spinner head covered in double-sided copper tape. While the vacuum mechanism is sufficient to hold a smaller 9 pad substrate during spinning, it will prove insufficient for the larger substrates and the tape adhesion is required.

4.3. Electron Beam Lithography

Electron beam (e-beam) lithography, performed in the central area of the photolithographic pads (see Fig. 4.1(C)) is used to fabricate the nanoscale components of the experiments. Typically two separately patterned layers, one of Au and one of Al, are needed to produce the devices discussed here. The e-beam lithography process mirrors the photolithographic procedure to a large extent:

- i) 6.5% MMA(8.5) in ethyl lactate from MircoChem is spun on the sample for 60 seconds at 3,000 rpm to form an underlayer with a nominal thickness of 300 nm.
- ii) The underlayer is baked for 30 minutes at 140° C.

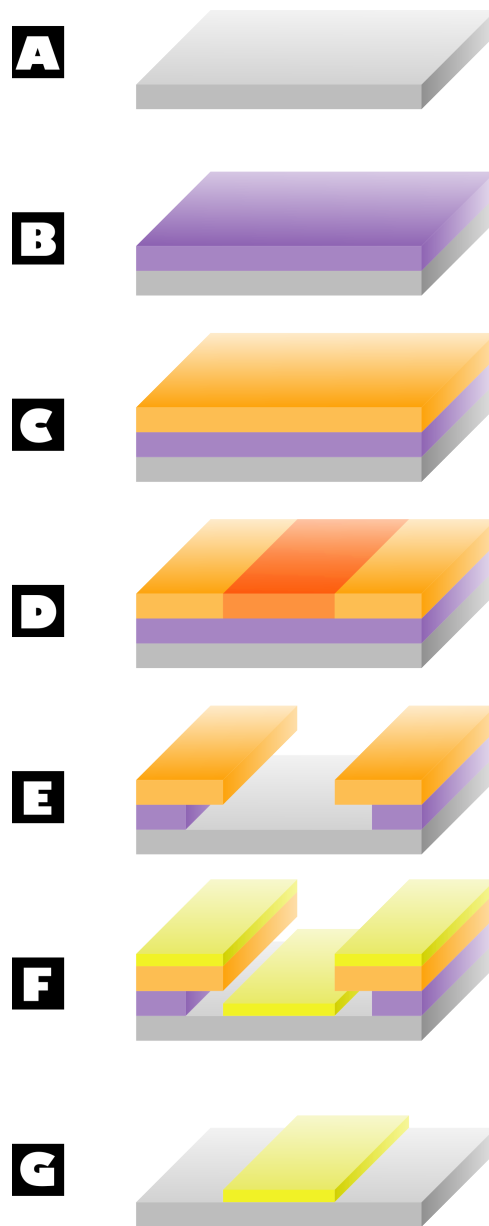


Figure 4.2. Photo and electron beam lithography process. (A) A bare or prepatterned SiO_2 on Si substrate is cleaned and prepared. (B) An underlayer is spun and baked on the substrate. (C) A resist layer is spun and baked on the underlayer. (D) A pattern in the resist is exposed using light or electrons. (E) The exposed resist and the underlayer beneath it are developed away. (F) Metal is evaporated onto the developed resist and substrate. (G) The remaining resist is chemically lifted off to leave patterned metal structures on the substrate.

- iii) 3% 950 PMMA e-beam resist in anisole from MircoChem is spun on the sample for 60 seconds at 4,000 rpm to form a layer with a 150 nm nominal thickness.
- iv) The resist is baked for 30 minutes at 170° C.
- v) The resist is exposed in a scanning electron microscope with exposure dosage dependent on the desired feature size. Fuller details on this step are provided below.
- vi) To develop the resist, a mixture of methyl isobutyl ketone and isopropanol in a 1:3 ratio is prepared and heated to 24° C. The sample is developed in a stream of this mixture for 1 minute, rinsed in a stream of pure isopropanol, and blown dry with nitrogen gas.
- vii) The sample is loaded into a refurbished Edwards¹¹ 306 thermal evaporator with either 99.999% pure Au or 99.999% pure Al. The etch gas supply tube is flushed with either oxygen or argon before the evaporation chamber is sealed.
- viii) After pumping the chamber to its base pressure of 3×10^{-7} Torr, the pumping is stopped and a plasma etch of either O_2^+ or Ar^+ is performed with the shutter closed. The chamber is pumped for a few minutes and the metal is then evaporated onto the sample. Further details on evaporation in the Edwards are discussed below.

¹¹Edwards, Ltd., Wilmington, MA, www.edwardsvacuum.com.

- ix) The chamber is pumped on for at least half-an-hour after evaporation to allow the chamber to cool. The chamber is vented with Nitrogen and the sample is removed and placed in a beaker of acetone.
- x) The sample is soaked for 5 minutes and then subjected to a stream of acetone to remove the unpatterned metal. If lifting off the metal proves difficult the sample may be soaked in acetone for several additional minutes. If lift-off problems persist the sample can be ultrasonicated in an acetone beaker; however, due to the violence of this process towards the nanoscale features, this should be avoided if possible and should last no more than 1 second in duration if necessary.
- xi) Once the lift-off is complete, the sample is rinsed in acetone, rinsed in isopropanol, and blown dry with Nitrogen.

For the electron beam patterning either a JEOL JXA-840 or Tescan Mira field emission scanning electron microscope is used. As lithography with the JEOL has been discussed in previous theses, we focus on some of the procedures used to pattern with the Tescan. The Tescan provides superior resolution to the JEOL and is equipped with a more efficient user interface. However, the overall stability of the JEOL, though requiring several hours to achieve, is better than the Tescan for fine multi-level alignment.

Samples are typically mounted on a standard flat sample holder using double-sided copper tape. To minimize the working distance between the beam and sample (and thus improve the resolution) a 1.2 cm standoff is used to raise the height of the sample. For ease of orientation, it is best to load the sample in the center of the Tescan stage carousel

(position 7) and manually rotate the sample on loading so that it is aligned with the stage's x-y axis (the chamber door slides open and closed along the x axis).

Once the sample is loaded and the chamber is being pumped down, the automatic stage calibration is performed. The z axis of the stage is then moved up to the 10 mm position to give a nominal working distance of just under 4 mm. When moving the stage to such a near position, the e-beam column and sample should be closely monitored on the chamber camera to ensure they are not in danger of touching.

Alignment of the microscope is performed by adjusting the magnetic coils along the e-beam column from the top down. First, one of the two Faraday cups on the stage is imaged and the magnification is increased to the point that the cup fills the entire view field. The autogun procedure is run to maximize the absorption current by aligning the gun tilt coils. Second, a non-critical part of the photolithographic pattern is imaged and focused. The manual adjustment is selected to perform alignment on the centering coils by wobbling the focus. This adjustment is done first by selecting and tuning the objective precentering coils to minimize the image shifts and then repeating the process with the objective centering coils. Finally, the stigmator coils are adjusted, initially by optimizing the focus and then by moving to an unpatterned section of the substrate and using the Analysis & Measurement tool in the Tescan software to write a spot at a magnification of 500,000 or higher. During the spot-writing, the graph of the absorption current is monitored and should change slowly or quickly depending on the quality of the focusing. After noting some change in the current, which can take a few seconds to a minute depending on the alignment, the spot is imaged and the working distance and stigmatism are adjusted to optimize the focus and roundness of the spot. This process is

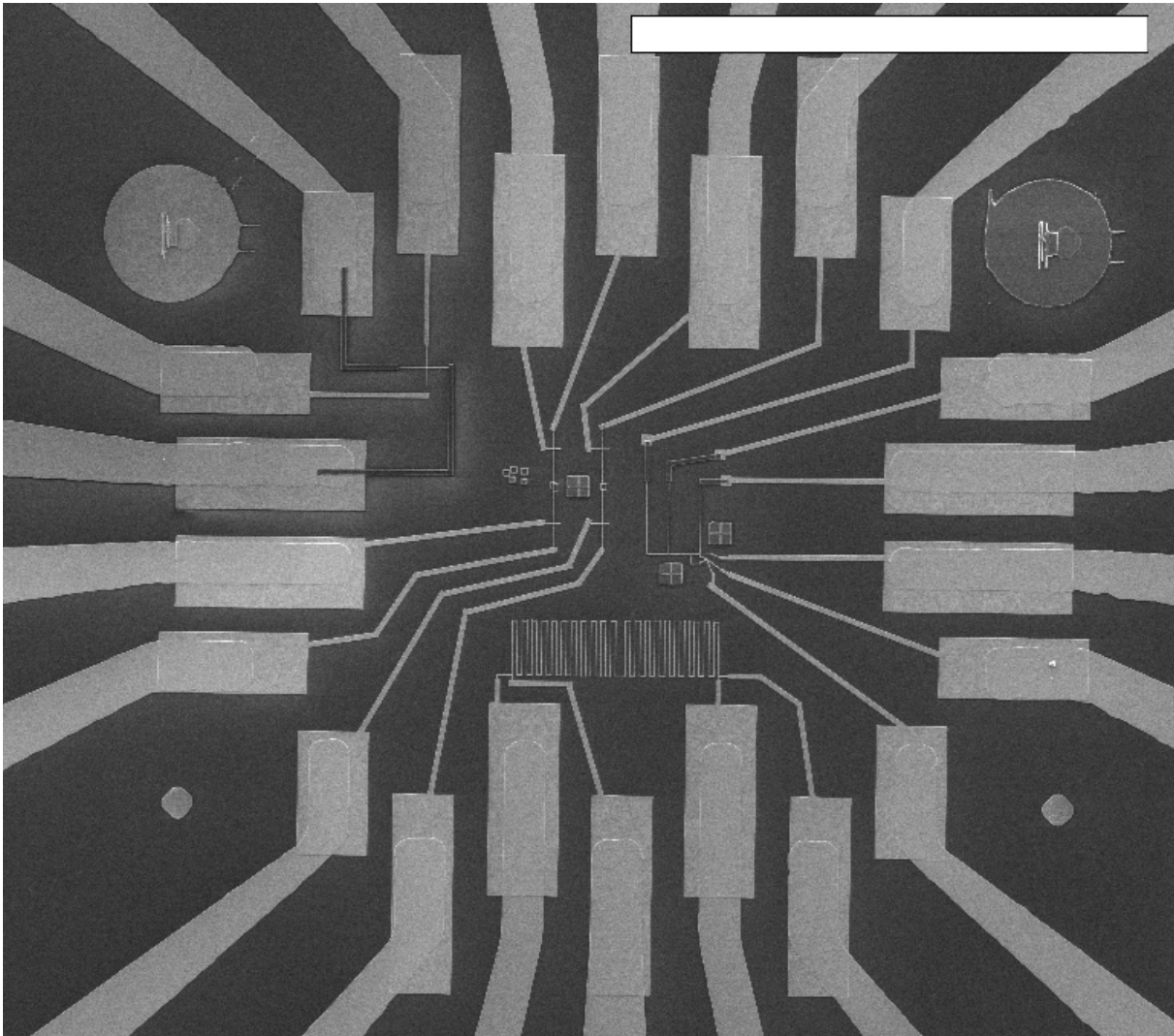


Figure 4.3. Center of an e-beam patterned photopad. Two e-beam layers of Au and Al have been deposited. During alignment of these layers the upper-right and upper-left photopad alignment marks have been exposed. The sample includes a normal-superconducting cross (upper-left) a normal meander wire (bottom) and a nonlocal coherence experiment (see Fig. 5.9).

often repeated several times until the spot exposure takes only a few seconds and the spot image is round with a 20 nm diameter. While the working distance is usually readjusted before e-beam writing on each photopad, the gun tilt, objective, and stigmation lenses are

not tuned further after this final spot test. The alignment procedure is typically performed at 30 kV acceleration voltage and the lowest probe current setting (PC20) corresponding to a current of around 10 pA.

After the beam alignment is adjusted, the next step is to align the position of the sample so that the layer to be patterned matches up with previous layers. This alignment is accomplished with assistance from the imaging features of Venkat Chandrasekhar's ElectronScribe program that can be used to control the electron beam when the Tescan Mira software is set to "external scanning". For patterning the first e-beam layer the following procedure is followed:

- i) The sample stage is rotated to make the photolithographic pattern as orthogonal to the image scan orientation as possible. For future reference, the coordinates of two points demarcating a horizontal line on the photopads are recorded (typically the upper left corner of the upper left photopad and upper right corner of the upper right photopad are used).
- ii) Starting from one of the corner leads on the upper left photopad, a small reduced scanning window is opened to image the edge of the lead. While imaging the edge, the stage is moved so that the center of the photopad is approached. As the lead narrows, the magnification of the image is increased. Typically the magnification starts at 1,000 and is increased to 10,000 by the time the end of the lead is reached. When the end of the lead is found, the stage is moved horizontally to bring one of the four photopad alignment marks into view.

- iii) The alignment mark is centered at the middle of the image scan and the magnification is increased to do a final focusing on the edge of the mark. The beam is then blanked externally by using the ElectronScribe program and the magnification of the Tescan is reduced to 2,000. The stage is then moved to center the photopad in the scan range. Typically, this requires moving the stage $45 \mu\text{m}$ in the x direction and $29 \mu\text{m}$ in the y direction with the signs of the shifts dependent on which alignment mark is being used.
- iv) Setting the ElectronScribe program magnification to correspond to the Tescan magnification, four $3 \times 3 \mu\text{m}$ alignment rectangles each centered around the $(\pm 45 \mu\text{m}, \pm 29 \mu\text{m})$ coordinates are used to take an image of the four photopad alignment marks. The stage is then moved to adjust the photopad position to be as centered as possible. With repeated imaging exposures and stage motion the photopad can be centered within a few hundred nanometers.
- v) The sample is now ready for patterning exposure with the ElectronScribe program; typical exposure parameters for various feature sizes are listed in Table 4.1.
- vi) After exposure of the first pad, subsequent pads may be easily located with the ElectronScribe “Pattern Grid” widget. Taking for the first and second alignment coordinates the horizontal points recorded in step i), a 3.597 mm spacing between pads (“die spacing”) for both the x and y directions, and the first pad’s alignment mark as the “starting die

Table 4.1. Typical E-Beam Exposure Parameters

Feature Width (nm)	PC (#)	Absorption Current (pA)	Dosage ($\mu\text{C}/\text{cm}^2$)	Rate (#)
50	20	10	250-350	1.8
75	20	10	250-350	1.6
100	20	10	250-350	1.4
500	20	10	250-350	1.0
5,000	14	60	150-200	1.0

coordinate focus”, the output coordinates yield stage positions on the Tescan that will bring one within a few microns of the corresponding alignment marks on the other pads. When the stage is moved to one of these positions, a reduced window scan, one tenth of the scan range area at 10,000 magnification, will usually image the alignment mark at the center of the screen. The writing process can then proceed from step iii).

If additional e-beam lithography layers need to be patterned, the earlier lithography layers should include alignment marks (usually $2 \times 2 \mu\text{m}$ crosses) that can be exposed for imaging when aligning the later layers. The e-beam lithography process is identical for later layers except that after a pad is centered using the photopad alignment marks, alignment rectangles in the ElectronScribe program are used to image the previously patterned alignment crosses. Electronic shifts controlled with the software can then be used to position the alignment crosses appropriately. These shifts allow for the possibility of aligning e-beam patterns to each other with tolerances of less than 10 nm.

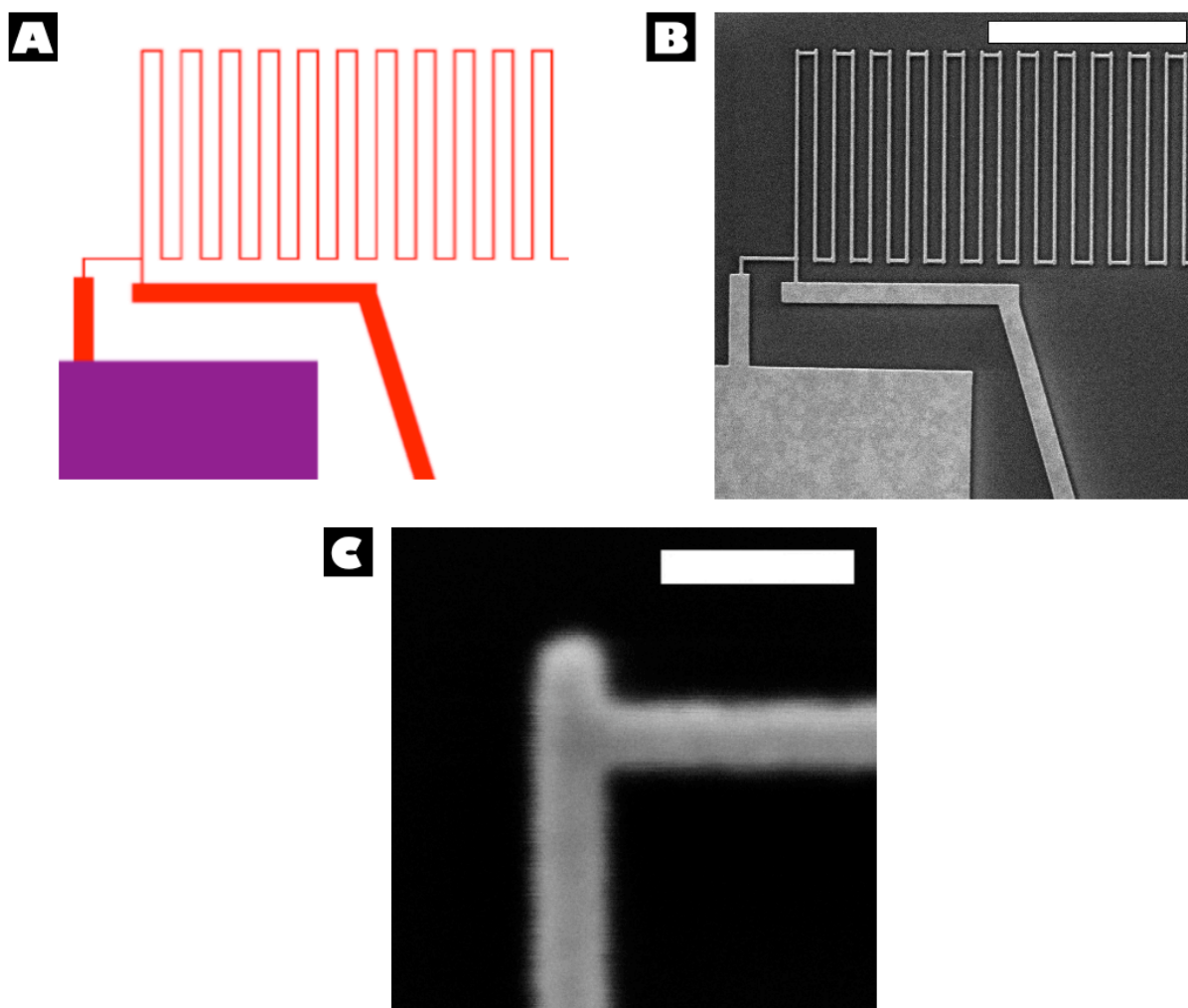


Figure 4.4. (A) ElectronScribe program design for part of a long Au meander wire. (B) Scanning electron image of the patterned meander; the size bar is $5\ \mu\text{m}$. Due to the speed of the beam deflection used to expose the vertical lines in the meander, the ratio between scan coil voltage and beam deflection is perturbed resulting in the lines overshooting the corners. (C) A close-up of the overshoot on one of the meander corners. The size bar is $200\ \text{nm}$.

Several obstacles to achieving such alignment are present due to deficiencies in the Tescan microscope design and must be accounted for during fabrication. First, the sample stage in the microscope undergoes small thermal drifts on the order of $5\ \text{nm}$ per minute.

One must work quickly between aligning and exposure in order for these drifts not to take the sample position too far out of alignment. Second, when the probe current is changed the scanning field of view will be shifted, sometimes as much as several hundred nanometers. For patterns with some features exposed at higher probe currents than others, the sample design should allow for the possibility of shifts this size. Third, when the scan coils of the Tescan are rastered at a high rate, as they typically are during exposure, the ratio of driving voltage to beam deflection changes slightly. This change can result in the dimensions of a patterned shape being a bit stretched in the direction of the fastest beam deflection as can be seen in Fig. 4.4; pattern designs must be altered to account for this stretching. The change in the voltage-to-deflection ratio can also affect the ostensible position of patterned alignment marks when imaging them with alignment rectangles, a mismatch that can be compensated for by using pairs of alignment marks that are symmetric about the scan origin and matching the alignment error evenly on both sides.

4.4. Thermal Evaporation

The main features of the Edwards thermal evaporator used to deposit Au and Al e-beam patterns are discussed in [74]. Since the writing of this reference, the potential evaporation rates of the instrument have been greatly improved by using an external 500 Amp AC current source from Denton Vacuum¹² in place of the Edwards source.

While the evaporator has been used to deposit Au wires with long phase coherence lengths in the past, initial samples prepared by the author found lengths of less than 1 μm . To improve on this value it was necessary to clean all removable parts in the evaporator

¹²Denton Vacuum Inc., Moorestown, NJ, www.dentonvacuum.com.

chamber, first by sand blasting, then by scrubbing with acetone and isopropanol. After reassembling the chamber, a new W thermal boat (from R.D. Mathis¹³) was cleaned in acetone and isopropanol and placed in the evaporator. Once the chamber is pumped down to its base pressure of 3×10^{-7} Torr, the boat was heated for half-an-hour using 100 Amps of current to bake it out. With Au loaded into this boat, evaporations capable of producing wires with long phase coherence lengths are now achievable. It is advisable to perform several pre-evaporations and allow the system to pump for a few days after cleaning to improve the coherence lengths further. After a boat for evaporating Au has been prepared it may be used repeatedly. While W boats are also used for the evaporation of Al, a new, unbaked boat should be used for each evaporation to maintain the purity of the Al. Degradation in Al quality has been empirically observed in the higher superconducting critical temperatures found for Al films fabricated with recycled boats.

As mentioned above the *in situ* etching performed prior to evaporations is critical for providing both good surface adhesion of the metals and good interfaces between them [74]. For the first Au layer, 40 mTorr of O₂ is introduced to the chamber after it has reached its base pressure. 5-600 Volts are applied to the sample with the shutter closed and chamber grounded to form an oxygen plasma. Typically the patterned substrate is etched for 25 seconds and the chamber is subsequently pumped 5 minutes to $\sim 10^{-6}$ Torr before a 50 nm Au evaporation is performed at a rate of 5 Å/sec using 125 Amps of heater current. For an Al evaporation 40 mTorr of Ar is used for a 70 second etch, followed by 2 minutes of pumping to $\sim 10^{-6}$ Torr, and evaporation of 80 nm at 15 Å/sec using 110 Amps of heater current.

¹³R.D. Mathis Co., Long Beach, CA, www.rdmathis.com.

4.5. Preparing Samples for Cooldown

After the Al layer has been evaporated, it is necessary to cool the sample down as quickly as possible to avoid the formation of AuAl_2 (“purple plague”) [76] at the interfaces which degrades the contact quality. The time from Al evaporation to having a sample cooled to liquid Nitrogen temperature is typically a matter of hours. Once the final lift-off is complete, images of the sample are taken in the electron microscope to determine which samples are suitable for measurement. There exists some mesoscopic folklore about the possibility that exposing normal metal wires to an electron beam will degrade their phase coherence properties. However, a test was conducted with simultaneously fabricated Au wires in which only some were imaged. Measurements of l_ϕ showed no difference between imaged and unimaged samples. The samples are mounted on a homemade 32-lead sample holder with a combination of vacuum grease and colloidal silver paste and the appropriate photopad leads are then wire-bonded to the sample holder using a Kulicke and Soffa¹⁴ 4123 Universal wedge bonder. While many samples were bonded using Al wire, Au wire was utilized for more recent bonding. Theoretically the Au wire should improve the low temperature thermal conductance of the leads to the sample, yielding colder electron temperatures, however a careful study comparing the two types of bonding wires was not performed.

During the final stages of fabrication, imaging, wire-bonding the samples, and loading them onto the fridge, care must be taken to avoid static discharges which result in currents large enough to burn out the nanometer-scale wires in the samples. Preventing discharges is achieved through a number of precautions: whenever possible grounding

¹⁴Kulicke and Soffa Industries, Fort Washington, PA, www.kns.com.

straps are worn, particularly when wire-bonding and loading the sample onto the refrigerator; the sample holder is kept in a grounding stage that shorts all the leads together; and humidifiers are run near the wire-bonder and refrigerator, promoting dissipation of static buildup with ambient moisture.

4.6. Dilution Refrigerator

Samples are loaded onto either a Janis¹⁵ ^3He SVSD refrigerator, an Oxford Instruments¹⁶ Kelvinox 300 dilution refrigerator, or an Oxford Instruments Kelvinox MX100 dilution refrigerator. As past group theses have discussed the use of the first two instruments, we here only discuss details involving the MX100.

A critical requirement of low current, low temperature transport measurements is to prevent rf noise from coupling into the dilution unit and the sample. To address this requirement, measurement signals are sent to the top of the fridge in shielded coaxial cables that mate to an rf filter box with an Amphenol¹⁷ connector (Fig. 4.5). The aluminum box from Pomona Electronics¹⁸ contains 4-pole C&K¹⁹ switches for grounding the lines and individual Pi filters from Spectrum Control²⁰ each with a 3 Db cut-off frequency of 800 kHz. After filtering, the lines pass through hermetic feedthroughs from Detorronics²¹ that are sent into the body of the fridge in twisted pairs of Supercon²² superconducting wire.

¹⁵Janis Research Company Inc., Wilmington, MA, www.janis.com.

¹⁶Oxford Instruments Inc., Concord, MA, www.oxford-instruments.com.

¹⁷Amphenol Corporation, Wallingford, CT, www.amphenol.com.

¹⁸Pomona Electronics, Everett, WA, www.pomonaelectronics.com.

¹⁹CoActive Technologies, Newton, MA, www.ck-components.com.

²⁰Spectrum Control Inc., Fairview, PA, www.spectrumcontrol.com.

²¹Detorronics Corporation, South El Monte, CA, www.detorronics.com.

²²Supercon Inc., Shrewsbury, MA, www.supercon-wire.com.

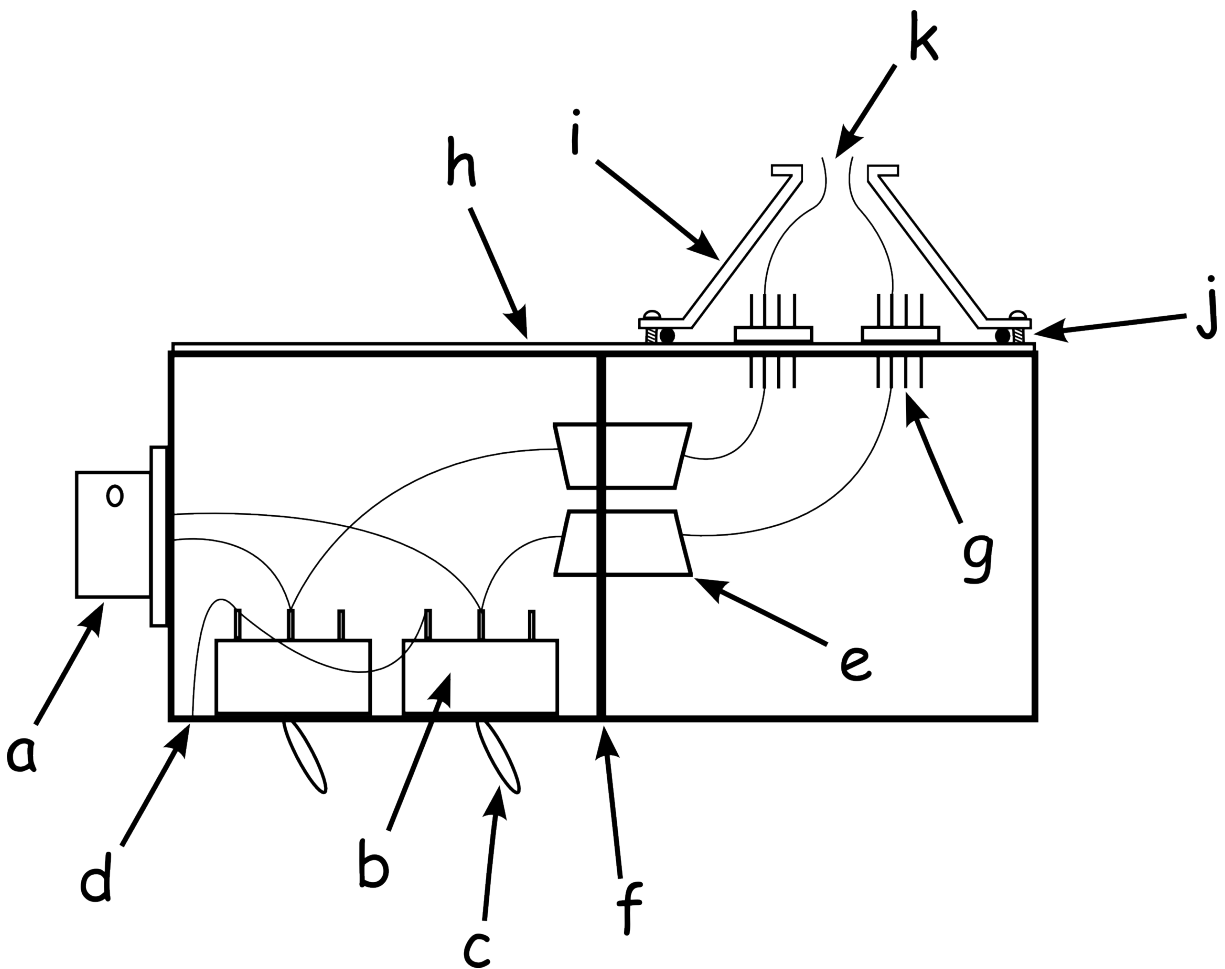


Figure 4.5. Schematic of the filter/feedthrough box attached to the top of the Oxford MX100 dilution refrigerator showing the path taken by two of the 32 wires. Shielded coaxial cables from the measurement electronics are plugged in with a 32-pin Amphenol connector (a). The lines go first to 8 4-pole C&K switches (b), which can be externally switched (c) to ground all the lines to a single point on the box (d). The lines are subsequently filtered through two Spectrum Control 25-pin d-sub rf Pi filter plugs. The filters are embedded in an aluminum divider (f), which shields the filtered half of the box. Lastly, the lines are sent through 4 8-pin Detronics hermetic feed-throughs (g) which are soft-soldered into the top plate of the box (h). The hermetic area is enclosed by a modified NW flange (i) sealed to the top plate with screws and an o-ring (j). The flange is attached to the top of the cryostat where twisted pairs (k) run down to the dilution unit.

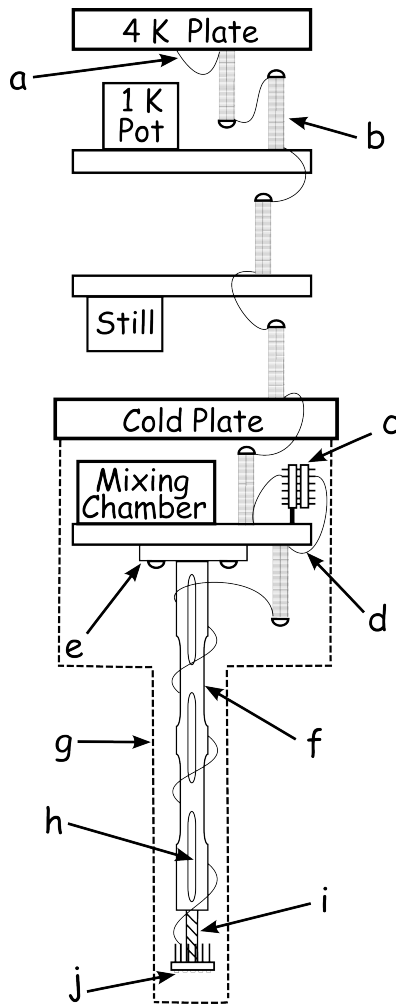


Figure 4.6. Schematic of the wiring for the Oxford MX100 dilution unit. Twisted pairs of superconducting NbTi wire in a CuNi matrix enter the vacuum can chamber through the 4K plate (a). The wires are wrapped around a series of copper heat sinks (b) coated with a thin electrical insulator as they travel down the dilution unit; the wires are sheathed in an insulating braid in between heat sinks. At the mixing chamber stage, a home-made connector (c) contacts the NbTi wires to plain Cu wire (d). The connector, subsequent heat sink, and detachable stage (e) are removable, allowing other types of experiments to be attached to the mixing chamber. The Cu wire is wrapped around a hollow copper rod (f) that extends into the narrow section of the radiation can (g). Slits (h) are machined through the rod to prevent eddy current heating when an external field is applied. An adjustable stainless steel screw (i) at the end of the rod allows the home-made sample holder (j) to be precisely set at the optimum level for field measurements.

A schematic of the lines as they travel down the dilution unit is shown in Fig. 4.6. Of crucial importance to cooling the electrons in the sample is extensive heat-sinking of the transport lines as they travel down the fridge. While the set-up shown is for transport measurements, the last section of the lines from the mixing chamber down are removable to allow other types of experiments to be mounted on the refrigerator.

The temperature of the MX100's mixing chamber is read by a RuO₂ resistor thermometer and "Femtopower" system from Oxford instruments. Initial cooldowns of the fridge before wiring produced a base temperature reading of 30 mK on this thermometer, higher than expected from the refrigerator's specifications. To cross check the thermometer readings a ⁶⁰Co nuclear orientation thermometer [77] was borrowed from Oxford Instruments and installed on the mixing chamber. A comparison of the nuclear orientation thermometer and RuO₂ thermometer showed discrepancies between the two below 40 mK with the former reaching temperatures of less than 16 mK (see Fig. 4.7). While subsequent adjustments to the fridge to improve radiation and noise shielding affecting the RuO₂ thermometer have allowed it to read as low as 18 mK, it is still likely that these readings are a few mK higher than the actual mixing chamber temperature.

4.7. Measurement Set-up and Techniques

4-terminal transport measurements are performed using Princeton Applied Research²³ 124 and 124A lock-in amplifiers with 116 preamplifier inputs and modified Adler-Jackson resistance bridges [78] constructed using General Radio²⁴ 1433 decade resistors. A low frequency (< 100 Hz) voltage signal is sent from the lock-in amplifier to the bridge in

²³Ametek Princeton Applied Research, Oak Ridge, TN, www.princetonappliedresearch.com.

²⁴IET Labs Inc., Westbury, NY, www.ietlabs.com.

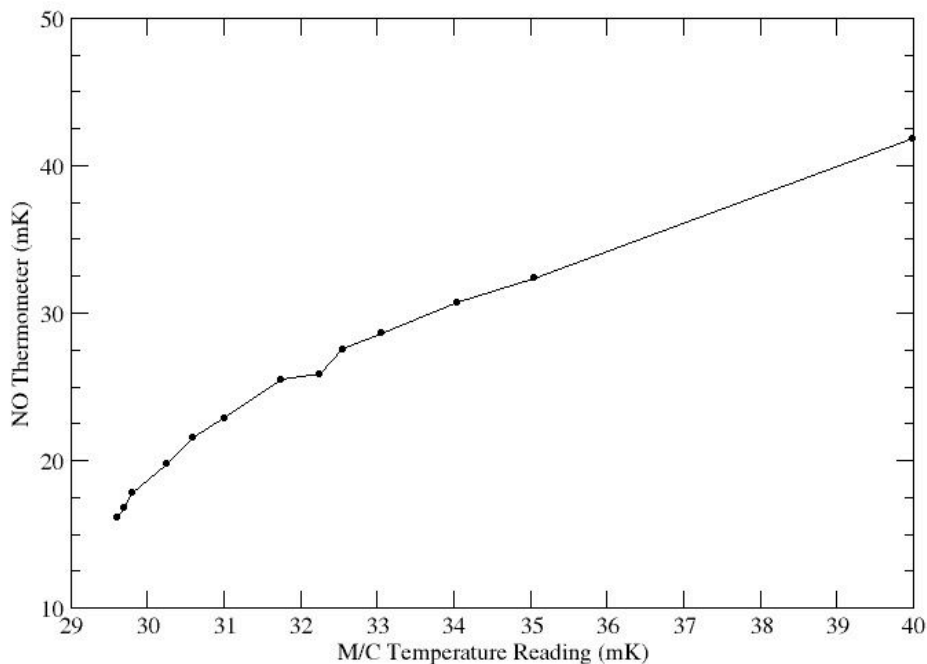


Figure 4.7. Comparison of the temperature of the mixing chamber on the MX100 dilution refrigerator as measured by a nuclear orientation (NO) thermometer and a RuO₂ thermometer. Recent improvements in the electrical noise and radiation coupling affecting the RuO₂ thermometer have allowed it to record readings as low as 18 mK.

which MΩ resistors convert the signal to a current source that is sent to the sample. Frequencies are chosen by examining the noise background on the sample with a Stanford Research Systems²⁵ SR760 spectrum analyzer and finding frequencies with noise at the background level (typically 4-8 nV/√Hz). Depending on the cryostat and set-up used, the low-frequency spectrum may be flat, though small 60 Hz harmonics are often present.

²⁵Stanford Research Systems Inc., Sunnyvale, CA, www.thinksrs.com.

The voltage signal across the sample and balancing resistor are input to a homemade first-stage 500x gain amplifier based on an AD624 chip. The signal is then sent back to the lock-in amplifier to monitor the voltage difference between the potential across the sample and balancing resistor. This difference is subsequently sent to an HP 34401A multimeter capable of transmitting a GPIB signal to a computer where data are recorded using an in-house data acquisition program.

Resistance is usually measured as a function of temperature (controlled by a heater on the mixing chamber or manually adjusting the dilution mixture circulation), magnetic field (controlled by various current sources and recorded with the aid of a homemade current monitor [73]), or DC current. Adding a DC current to the AC measurement current from the lock-in and bridge means the lock-in is reading the differential resistance (dV/dI) of the sample at the input DC current. Most DC current measurements use an AD624-based current source controlled by a Keithley²⁶ 230 voltage source or HP²⁷ 3345A function generator with the current monitored by measuring the voltage drop across an in-series resistor. Circuit diagrams for the resistance bridge, AD624 based instrumentation amplifiers, and AD624 based current sources can be found in [72]. For a few measurements, such as are shown in Fig. 4.8, a second DC current can be added through the sample using a floating circuit. This diagram also illustrates a setup for measuring IV characteristics of a sample by using one of the DC current setups in conjunction with a AD624 amplifier and HP multimeter for measuring the DC voltage.

To minimize the noise on input and output signals to and from a sample, coaxial cables are used for all signals between measurement equipment leading to the filter box on the

²⁶Keithley Instruments Inc., Cleveland, OH, www.keithley.com.

²⁷Agilent Technologies, Santa Clara, CA, www.home.agilent.com.

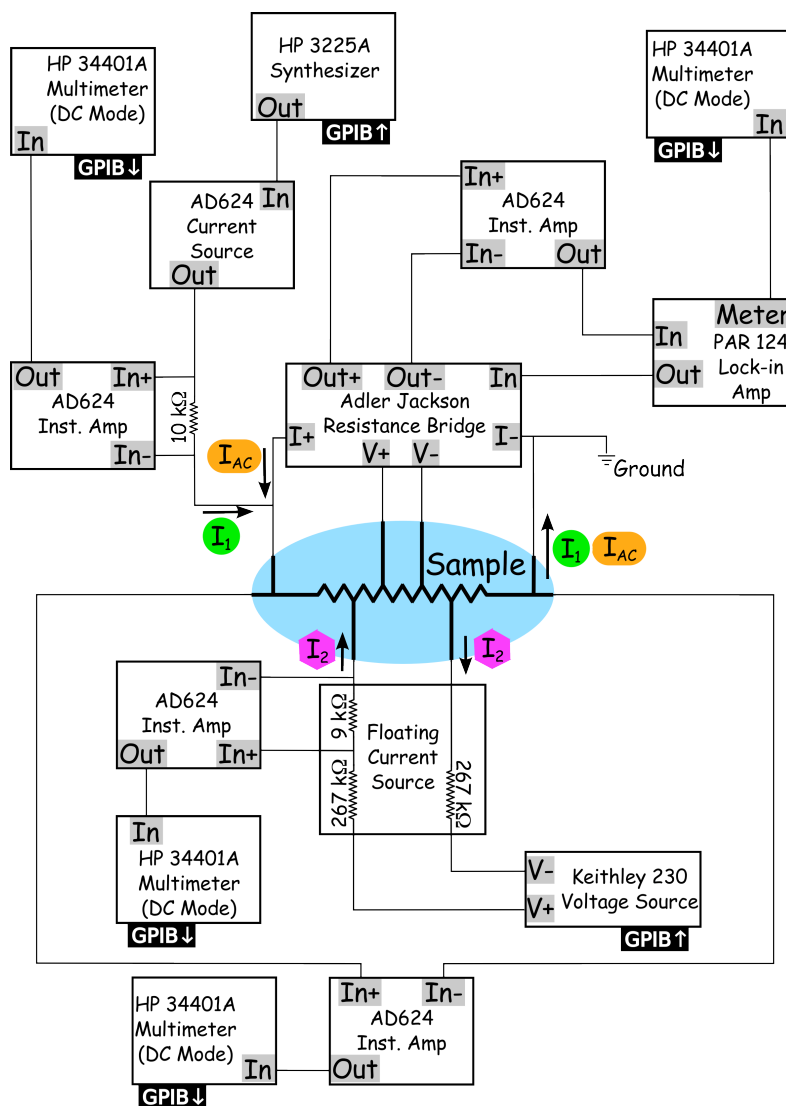


Figure 4.8. Example of a measurement set-up. The sample, represented as a resistor at the center of the diagram is subject to several simultaneous transport measurements. The circuit in the upper right quadrant uses a lock-in amplifier and bridge to conduct a 4-terminal AC measurement of the resistance of the central section of the sample. When adding the DC current set-up in the upper left quadrant to produce and measure I_1 the lock-in and bridge can measure current-dependent differential resistance. A second DC current I_2 following a different path can be added using the floating circuit just below the sample. Finally, the DC voltage across the entire sample can be measured using the circuit at the bottom of the page to create I-V curves in conjunction with I_1 . The GPIB tag indicates components being controlled or read via GPIB with a computer.

top of the cryostat. In addition, the AD624 first-stage amplifiers and current sources are battery operated to eliminate possible line frequency noise. These instruments and the bridge are placed in a shielded μ -metal box for further noise minimization. The box is located less than 1 m from the top of cryostat, with the coaxial lines from box to cryostat sheathed in several layers of metal shielding.

CHAPTER 5

Experimental Results

To experimentally detect signs of EC and CAR, we focus on four predicted aspects of these processes discussed in Ch. 3.

- 1) These processes occur when two spatially separate normal metal probes are placed on a superconductor.
- 2) Their effects are nonlocal; no current need be sent between the probes.
- 3) Their effects should attenuate rapidly with the separation of the probes, exponentially over a superconducting coherence length or faster.
- 4) Effects between the two probes due to these processes are phase coherent.

As discussed in Sections 2.3 and 3.2, for the transparent interfaces between the normal probes and superconductor that we use here, the dominant signal seen for an experiment with the configuration of 1) will be charge imbalance. Though charge imbalance will also be shown to be a dominant nonlocal signal, thus satisfying 2), we will demonstrate in this chapter that, using characteristics 3) and 4), signals consistent with all four of these criteria for EC and CAR can be isolated from the charge imbalance background.

5.1. Charge Imbalance

An example of a large charge imbalance effect is shown in Fig. 5.1. In this experiment a 100 nA AC measurement current is sent across the interface between a 45 nm thick

superconducting (S) Al wire and a 30 nm thick ferromagnetic (F) Ni ellipse.¹ As shown in the annotated scanning electron micrograph of Fig. 5.1(A), when the current is injected the potential drop across the interface in series with short sections of Al and Ni is measured with either two Au probes or one Au probe on the ferromagnet side and one Al probe on the superconducting side. Above the 1.2 K superconducting T_c of Al, the different sets of voltage probes measure the same resistance. However, below T_c the measured interface resistance diverges depending on whether the V- voltage probe is Au or Al (Fig. 5.1(B)). As discussed in Section 2.3, the difference in the two measurements is due to the current sent across the ferromagnet-superconductor interface, which creates non-equilibrium quasiparticle excitations resulting in a net charge imbalance of electron-like and hole-like excitations within the superconductor. While this imbalance relaxes over micron-scale distances in the superconductor, leading to its eventual absence in the Al voltage probe, the Fermi level of the Au voltage probe equilibrates with the imbalanced quasiparticle potential at its point of contact with the superconductor.

The connection between the two different interface measurements and the discussion of charge imbalance in Section 2.3 can be seen most clearly by subtracting the two interface measurements (Fig. 5.1(C)). The resulting curve is the difference between the potential seen by a normal probe and a superconducting probe (normalized by the injected current) at the same point on the superconductor just to the left of the ferromagnet-superconductor interface. At temperatures just below T_c , the superconducting gap is small and the thermal distribution of the incident current contains higher energy quasiparticles than at lower

¹This sample was fabricated by Zhigang Jiang and measured by the author. All other samples discussed in this chapter were fabricated and measured by the author.

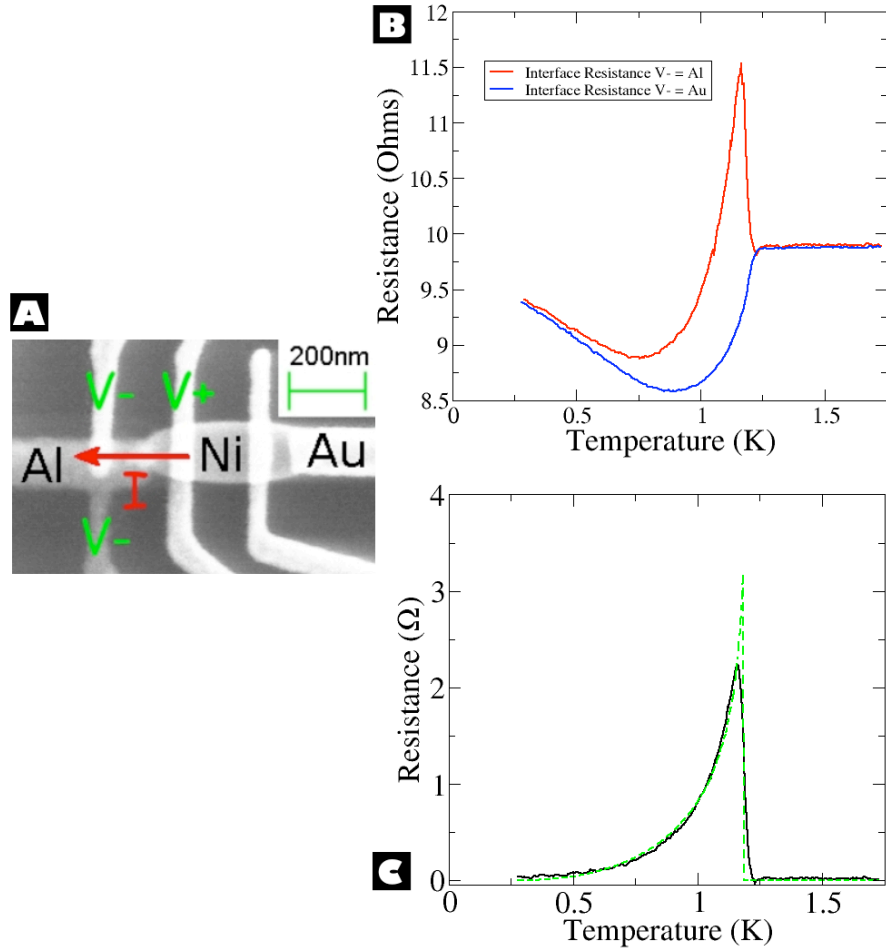


Figure 5.1. **(A)** Scanning electron micrograph of an interface between a ferromagnetic Ni ellipse and a superconducting Al wire with Al and Au voltage and current probes. **(B)** Interface resistance using either the Al probe or the Au probe as the V- lead. **(C)** Difference between the two curves in (B), which results in the potential difference when the same point on the superconductor is measured with either a normal probe (quasiparticle potential) or a superconducting probe (condensate potential). Due to normal quasiparticles injected above the superconducting gap the Au probe measures a higher, charge imbalance potential than the Al probe. As the temperature is lowered the injected current is dominated more and more by sub-gap quasiparticles and the charge imbalance potential decreases. The dashed line shows a fit to a modified BTK model of charge imbalance.

temperatures. These two factors combine to create a large number of above-gap excitations in the superconductor, resulting in a significant charge imbalance voltage detected in the normal probe. As the temperature is lowered, the size of the energy gap increases and the injected electrons hew closer to the Fermi energy. A higher and higher proportion of the incident charge carriers are then below the gap, the number of quasiparticle excitations in the superconductor diminishes, and the charge imbalance voltage decreases. This qualitative picture is reflected by the experiment and the quantitative theoretical curve of the BTK model discussed in Section 2.6. The fitting curve is a slightly modified form of the BTK predictions due to Strijkers *et. al.* [79] which includes the possibility that the injected current from the ferromagnet is spin-polarized. This modification broadens the charge imbalance regime slightly, but does not change the overall character of the curve. For the simulation shown, a BTK barrier strength of $Z = 0.2$ and a spin polarization of 0.175 is used. The latter value is somewhat lower than expected for current injected from Ni [80].

Although, as was discussed in Chapter 3, the use of ferromagnetic probes on superconductors presents a promising path for distinguishing the EC and CAR effects [53, 58, 59, 62], we will focus here strictly on the use of normal metal (N) probes used to detect the combined EC and CAR effects and satisfying the conditions outlined at the beginning of this chapter. There are a number of reasons for preferring normal probes over ferromagnetic ones. First, the large magnetic field and field gradients present in the vicinity of a ferromagnetic probe suppress and perturb the superconducting condensate, leading to the possibility of additional field-dependent effects in the transport data, which has been largely ignored in the theory. Second, as seen in the experiment of

Beckmann *et. al.*, nonlocal measurements conducted with ferromagnetic probes demonstrate a spin-valve signal [63, 64, 81] that may be difficult to separate from other nonlocal effects. Third, the exchange energy in ferromagnets E_{ex} , which results in a disparity between the carrier energy for different spins, produces robust singlet Cooper pair dephasing for currents across a superconductor-ferromagnet interface [82]. For typical ferromagnets $E_{ex} \approx k_B T_{Curie} \sim 100$ meV corresponds to a dephasing time of $\tau \approx \hbar/E_{ex} \sim 5 \times 10^{-15}$ sec. This time scale results in a dephasing distance of tens of nanometers, making demonstrations of the phase coherence of EC and CAR effects discussed below exceedingly difficult using lithographically produced devices. Fourth, the transparent contact regime, where the cancellation of EC and CAR signals is predicted to be smallest [66], can be achieved more readily using normal metal probes [74].

Perhaps the simplest case of transport using normal probes is the direct measurement of an NS interface. As shown in Fig. 5.2(A), a cross composed of one Al wire and one Au wire is used to directly measure a superconductor-normal metal interface. In this and all subsequent samples discussed, the Al film thickness is 80 nm and the Au film thickness is 50 nm with the widths of the wires around 100 nm. Examining the resistance of this interface as a function of temperature using a 100 nA AC measurement current (Fig. 5.2(B)), we first note that the interface resistance when the Al is in the normal state is very low: 70 m Ω , comparable to the limiting Sharvin resistance [83] of 10 - 20 m Ω . On cooling through the transition temperature T_c a charge imbalance peak appears. As theoretically expected this peak decays with temperature, however once the temperature reaches $\sim T_c/2$, the region where charge imbalance should be almost entirely absent, there is still a measured resistance of 1 Ω . Both the temperature independence of

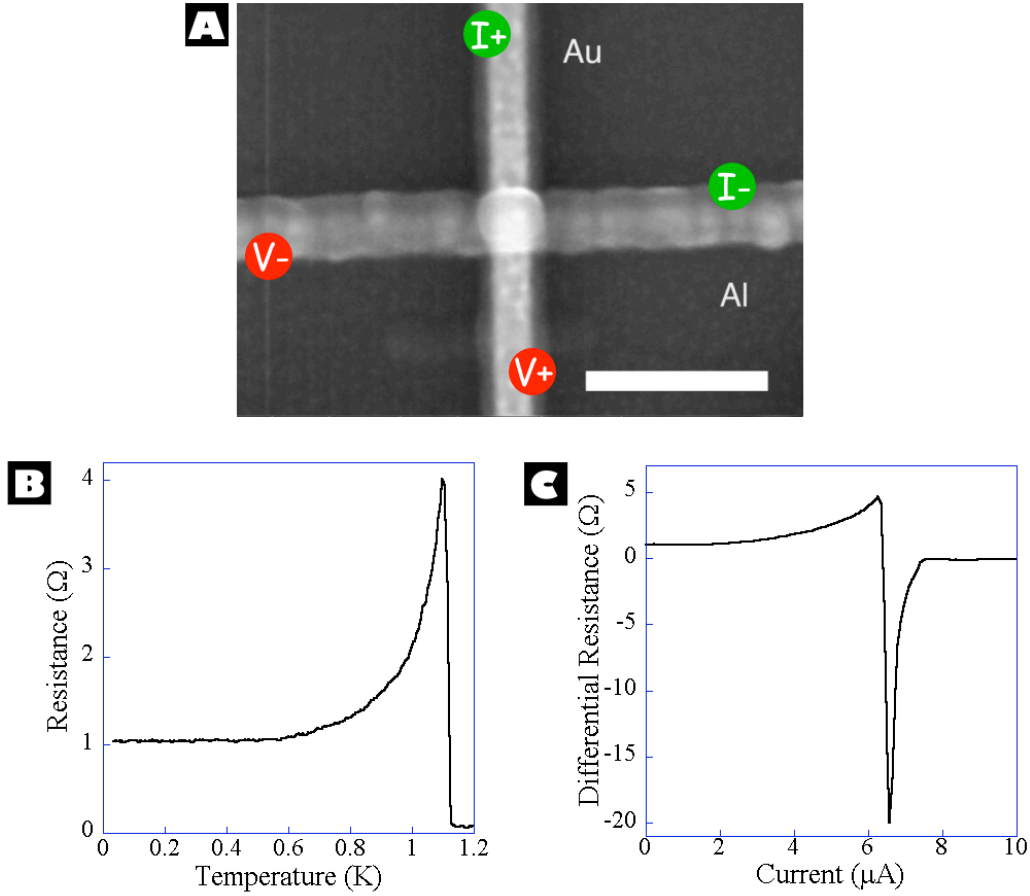


Figure 5.2. (A) Au-Al normal metal-superconductor cross. The interface is measured using the marked configuration; the size bar is 300 nm. (B) Resistance of the interface as a function of temperature. Above the Al T_c the interface resistance is 70 m Ω . When cooled, a large charge imbalance signal is seen below T_c . This signal decays but leaves a remnant resistance of over 1 Ω , which appears to be temperature independent below 0.5 K. (C) Differential resistance of the cross at 20 mK as a function of a DC current added to the AC measurement current. At low bias the remnant resistance of $\sim 1 \Omega$ is present. A charge imbalance peak develops at higher bias until the critical current is reached just above 6 μA .

this resistance below 0.5 K and its magnitude of more than ten times the normal state resistance stand out. From the BTK picture, for the lowest temperatures we should be observing sub-gap transport at the interface. This transport should only be temperature

independent in the limit of very clean (dominated by Andreev reflection) or very dirty interfaces (dominated by regular reflection). Our sample preparation and the low normal state resistance would lead us to expect that the interface is in the former category, but, in this Andreev reflection limit, the resistance is expected to saturate at a value smaller than the normal state resistance, not an order of magnitude larger.

A possible resolution to this paradox presents itself if we regard the cross not as a single normal metal-superconductor interface, but as two normal metal probes placed within a superconducting coherence length of each other on a superconductor. Though the probes marked “I+” and “V+” in Fig. 5.2(A) are fabricated as a single wire, the proximity effect in this wire where it intersects the superconductor may be robust enough to effectively separate the I+ and V+ leads. If this is the case, the conditions exist for current incident from the I+ lead to create EC and CAR effects in the V+ lead. The observed 1Ω signal is consistent with this hypothesis in its sign, as the positive voltage producing EC is expected to dominate in the transparent contact regime. The temperature independence of the signal would also be expected in the transparent contact limit for $T \ll \Delta/k_B$, which should be satisfied below 0.5 K as direct measurements of Δ for nanoscale Al wires find $\Delta/k_B \simeq 200 \mu\text{eV}/k_B = 2.3 \text{ K}$ [84].

5.2. Nonlocal Signals

To test this hypothesis that the majority of the low temperature NS cross resistance is due to EC and CAR, we fabricate a normal metal-superconductor sample that allows true nonlocal measurements. Shown in Fig. 5.3(A), the sample consists of an NS cross with six additional normal metal probes located on the superconductor, spaced at 210 nm

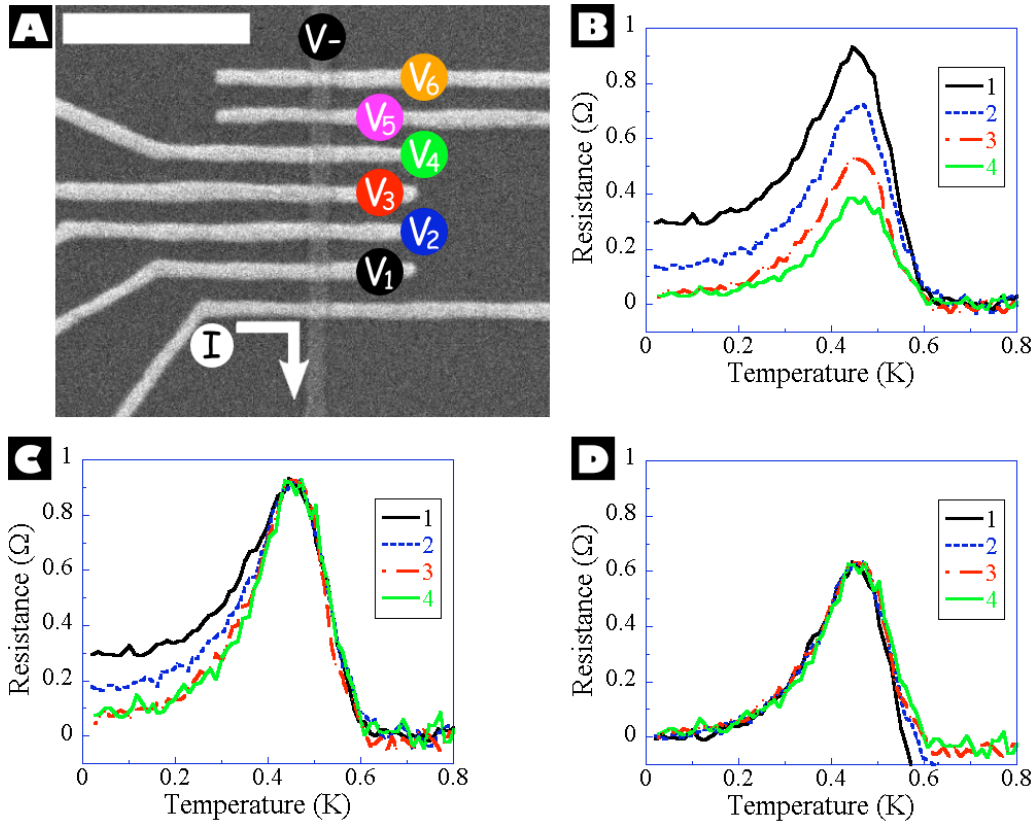


Figure 5.3. **(A)** Scanning electron microscope image of an Au-Al normal metal-superconductor sample with six nonlocal Au leads each separated by 210 nm. Current is sent from the bottom normal lead into the superconducting wire and the six nonlocal voltages are measured relative to the condensate potential V_- . The size bar is 1 μm . **(B)** Temperature dependence of the first four nonlocal leads measured with 20 nA AC measurement currents. Due to the inverse proximity effect from the large number of normal leads, the T_c of the Al is suppressed to around half of its usual value. Below T_c a charge imbalance peak is present on all the leads. As the sample is cooled towards zero temperature the nearest leads retain a significant nonlocal voltage. **(C)** The charge imbalance signal has a distance dependence that is different from that of the zero-temperature saturation as can be seen by noting that the full temperature curves cannot be scaled onto each other. **(D)** Only if the zero-temperature signal is subtracted from the data can the entire curves below T_c be scaled to each other.

intervals. By sending current across the bottom NS interface we can probe the nonlocal voltage created on the normal metal probes (located outside the current path) relative to the condensate potential. As with the local interface measurement, a large charge imbalance peak appears just below T_c . (Due to the large number of normal probes on the superconductor and the inverse proximity effect, the T_c is reduced to around half of its usual value.) For a given temperature this peak decays as the distance of the nonlocal probe from the NS interface increases (Fig. 5.3(B)), reflecting the gradual re-equilibration of the quasiparticle potential. Again, when the temperature is decreased the charge imbalance signal decays, but on the closest probes there is still a finite nonlocal resistance similar to what was seen for the NS cross. We can now see that this $T \rightarrow 0$ nonlocal signal decays rapidly with distance, over a length scale shorter than the charge imbalance decay. These two scales are graphically presented in Fig. 5.3(C) and (D). In the first figure the charge imbalance peaks are scaled to coincide, but the zero temperature values do not overlap. Only in the second figure, when the zero temperature values are first subtracted from the curves, can they be scaled to match up below T_c .

The two length scales present in the decay of the nonlocal signals can also be seen by examining the nonlocal differential resistance at 20 mK as the DC current across the NS interface is increased (Fig. 5.4). With this increase there is an increase in the number of quasiparticles traversing the interface with energies above the gap, leading to a charge imbalance peak that rises with the current until the critical current of just below $3 \mu\text{A}$ is reached. In analogy with the temperature curves, two different length scales can be found for the zero-bias resistance and the high-bias peak. The decays for these two bias regimes are shown in Fig. 5.4(B). If the zero-bias behavior is due to EC and CAR effects it should

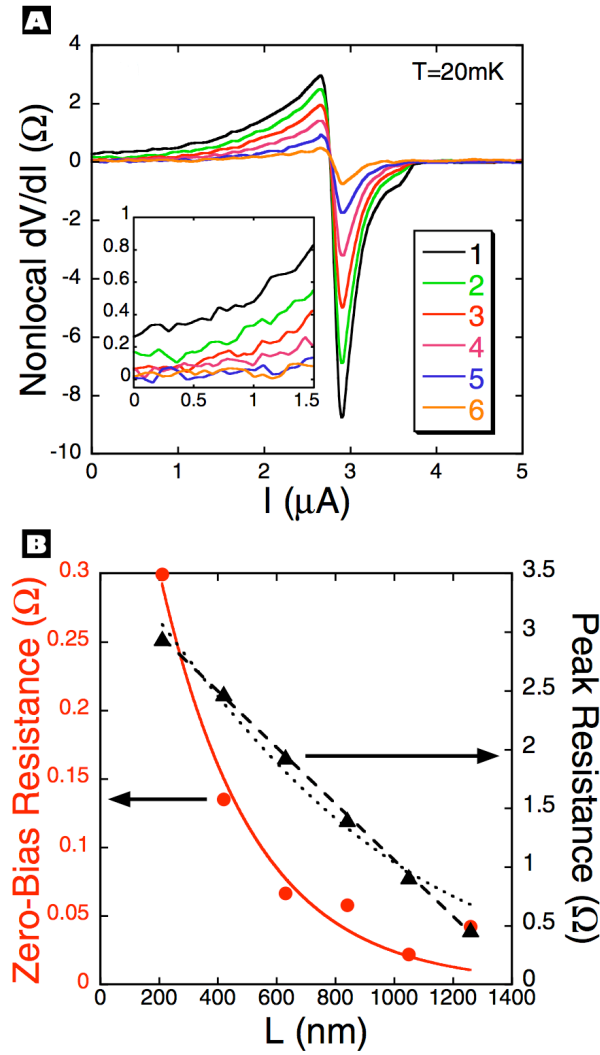


Figure 5.4. **(A)** Nonlocal differential resistance measurements of the six leads shown in Fig. 5.3(A) as a function of DC current bias. The traces show a charge imbalance signal developing with increasing bias until the critical current is reached just below $3 \mu\text{A}$. Inspection of the low-bias regime shown in the inset reveals a nonlocal voltage that rapidly decays with distance, similar to the temperature traces of Fig. 5.3(B). **(B)** As with the temperature data separate scaling parameters can be found for the zero-bias resistance and the charge imbalance peaks. The zero-bias signal decays much more rapidly than the charge imbalance signal.

decay exponentially or faster with the superconducting coherence length ξ_S [60]. The solid line shows the best fit for the exponential decay, e^{-L/ξ_S} , yielding a value of $\xi_S = 315$ nm. One achieves a slightly better fit, with $\xi_S = 217$ nm, if the possibility of a small offset due to the measurement bridges is included. Typical values of ξ_S for plain Al films deposited in our lab are 140-310 nm [26]. The fitted values of ξ_S are in very good agreement with this range given that the inverse proximity effect present in this sample may increase the coherence length from its bulk value. A fit to the peak decay using $(1 - \tanh(x/\Lambda_{Q^*}))$, the predicted functional form for charge imbalance recombination [85, 26], is shown as a dotted line with a value of the charge imbalance length $\Lambda_{Q^*} = 1085$ nm. We note that an even better fit (dashed line) is obtained positing a linear decay, $(\Lambda_{Q^*} - x)$, with $\Lambda_{Q^*} = 1442$ nm, which would be expected if the relaxation of the quasiparticle created voltage followed the same linear decay as it does in a normal metal. With either model, Λ_{Q^*} is consistent with the lower end of previously measured charge imbalance lengths [22, 71, 26].

We have thus observed two different nonlocal effects. The first is entirely consistent in its temperature, current, and distance dependence with the well-studied charge imbalance effect. The second nonlocal effect seen at low temperatures and low current bias occurs between normal probes placed on a superconductor and decays on a length scale comparable to ξ_S . This effect is consistent with the first three of our criteria for EC and CAR laid out at the beginning of the chapter. To demonstrate the fourth criterion, phase coherence, we need to make devices that create tunable quantum interference.

5.3. Nonlocal Coherence

To create quantum interference we use a variant of the Aharonov-Bohm (AB) effect [86]. This effect uses the dependence of the phase of a charged particle on the magnetic vector potential \mathbf{A} over the possible paths it can traverse. For two possible paths enclosing an area, the accumulated phase difference is given by:²

$$(5.1) \quad \Delta\phi = \frac{e^*}{\hbar} \oint \mathbf{A} \cdot d\mathbf{s} = \Phi/\Phi_0,$$

where e^* is the charge of the particle, the integral is around the enclosing path, Φ is the magnetic flux enclosed by the path, and $\Phi_0 = h/e^*$ is the flux quantum for the charge. By confining a charge carrier to a loop one can observe shifting interference effects as $\Delta\phi$ is tuned from 0 to 2π using the external field, provided the charge carrier maintains its phase coherence all the way around the loop. Oscillations in the magnetoresistance of a mesoscopic normal metal loop (with flux period h/e) are an example of the AB effect [87].

Flux-periodic behavior can also be observed in measurements of the transport properties of segments connected to, but not on, mesoscopic loops. Measurements of the resistance of normal [88] and superconducting [89] wires connected to loops have demonstrated that, provided the phase coherence length of the charge carrier extends from the wire to around the loop, one can observe evidence of quantum interference.

Here we present a variant of these experiments using a hybrid normal metal-superconducting loop, known as an Andreev interferometer [90, 91], and normal probes located just off of the loop on the superconductor (see Fig. 5.5, 5.9, 5.14). There are two pertinent

²Gaussian units are used throughout.

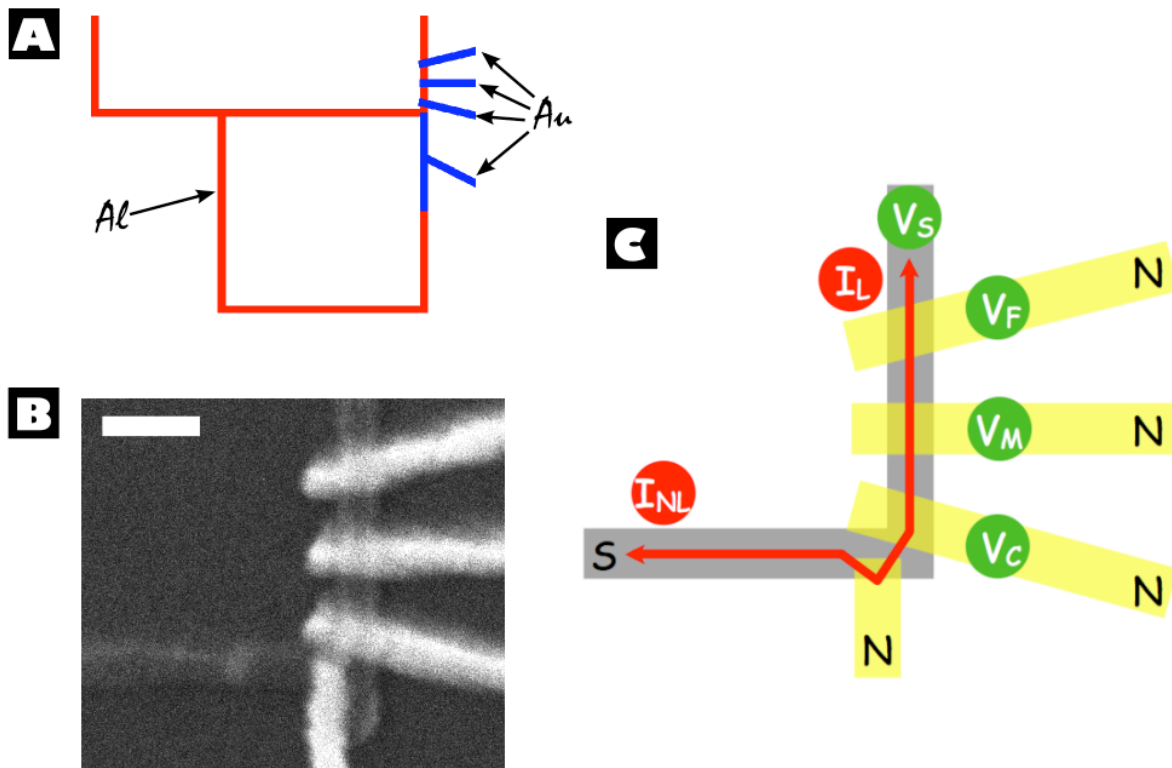


Figure 5.5. (A) Design of a normal-superconducting interferometer loop with nonlocal normal leads just off of the loop. (B) Scanning electron micrograph of the upper-right corner of the fabricated sample; the size bar is 300 nm. (C) Measurement schema showing two possible current paths across the NS interface on the loop. The nonlocal current path I_{NL} travels around the loop but does not pass the three voltage leads V_C , V_M , and V_F which are measured in reference to the condensate voltage V_S . The local current I_L travels around the loop, but also crosses the voltage leads.

differences between this variant and the previous experiments examining off-loop phase coherence. First, our measurements will be strictly nonlocal – no current is sent across or through the off-loop probes. Second, and more importantly, the previous experiments were demonstrations of the phase coherence of a single charge carrier, a normal metal quasiparticle or superconducting Cooper pair. Here, we need to demonstrate the coherence of the EC and CAR *processes* between the two carrier types. To do so we have one NS

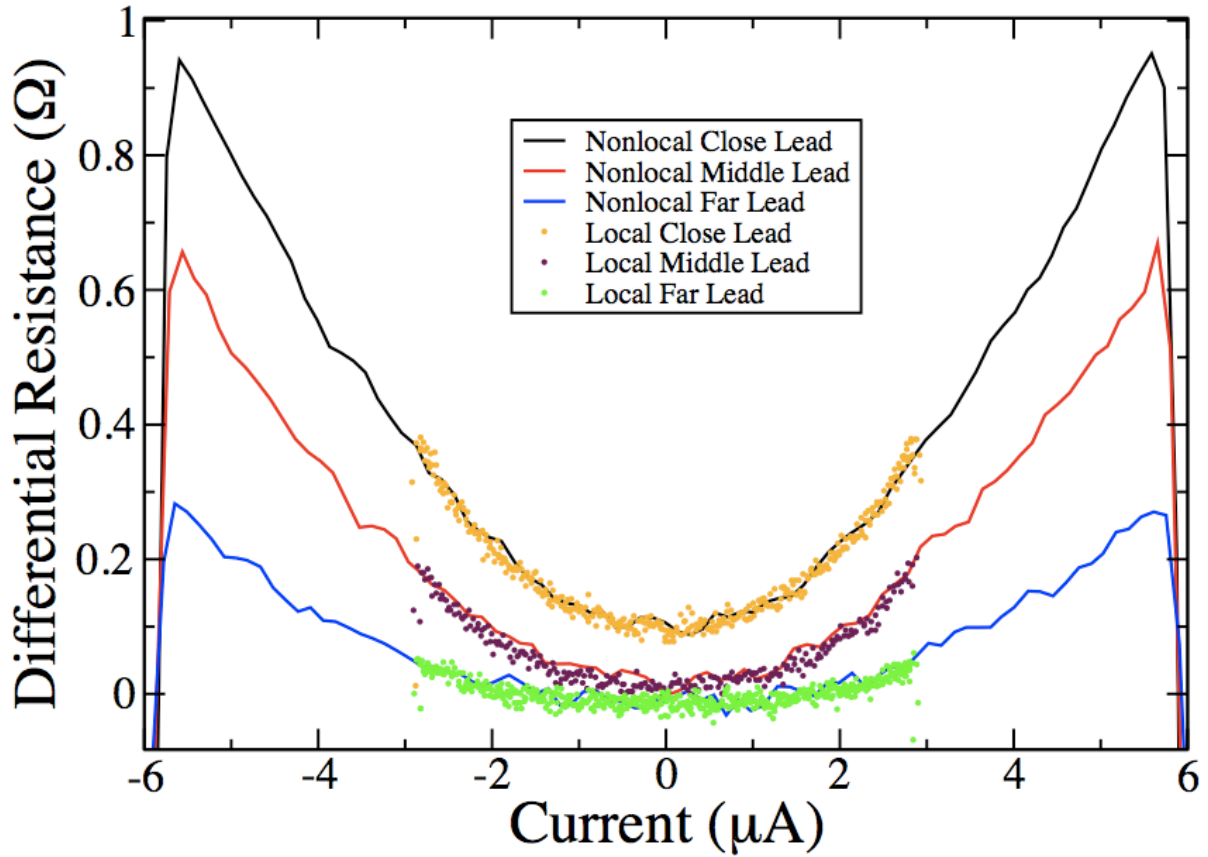


Figure 5.6. Differential resistance measurements for the two different current configurations of Fig. 5.5(C) show that while the two current paths have different critical values, the measured voltages are independent of the current paths.

interface on the loop and a second, formed by the nonlocal probe, off of the loop, but within a superconducting coherence length of the on-loop interface.

A first attempt at such a device is shown in Fig. 5.5. As discussed below, the normal metal coherence length for this sample is too short to observe any robust phase-coherent behavior in this sample when a flux is threaded through the loop. It is worthwhile, though, to examine some of the properties of this sample as it bridges the behavior of the linear nonlocal sample described above and the fully coherent loop samples described below.

As shown schematically in Fig. 5.5(C), a 20 nA AC measurement current can again be sent across an NS interface and nonlocal signals measured on a series of normal probes at different distances from the interface. The differential resistance curves for these nonlocal probes as a function of DC bias current are shown in Fig. 5.6 and exhibit identical behavior to the linear sample, with charge imbalance peaks at high bias and a zero-bias resistance present on only the closest probes. In addition to this nonlocal measurement we can also perform the same measurement using a local current that crosses the three normal probes. Due to the loop structure this current path has half of the critical current of the nonlocal path, but below this critical current we note that the signals measured for the two different current paths are indistinguishable. EC and CAR effects, relying centrally on transport conversion across the interface should be independent of the direction of the condensate flow. The picture described in Section 2.3 of charge imbalance as a pooling of quasiparticle excitations which undergo a diffusion and recombination in the superconductor independent of the condensate current is consistent with the identical higher bias behavior seen for the two current paths.

Using the local measurement configuration, we can again use scaling techniques to separate the charge imbalance signal from the zero-bias effects. Fig. 5.7 shows that once the zero-bias resistance has been subtracted from the differential resistance curves, the traces can all be scaled to coincide. As with the linear sample, the peak decay is on the order of a micron, appropriate for charge imbalance, while the zero-bias resistance decays over a few hundred nanometers, consistent with the EC and CAR processes.

The short normal metal phase coherence length of the Au in this sample can be directly observed by measuring the magnetoresistance of a long 250 μm Au wire that

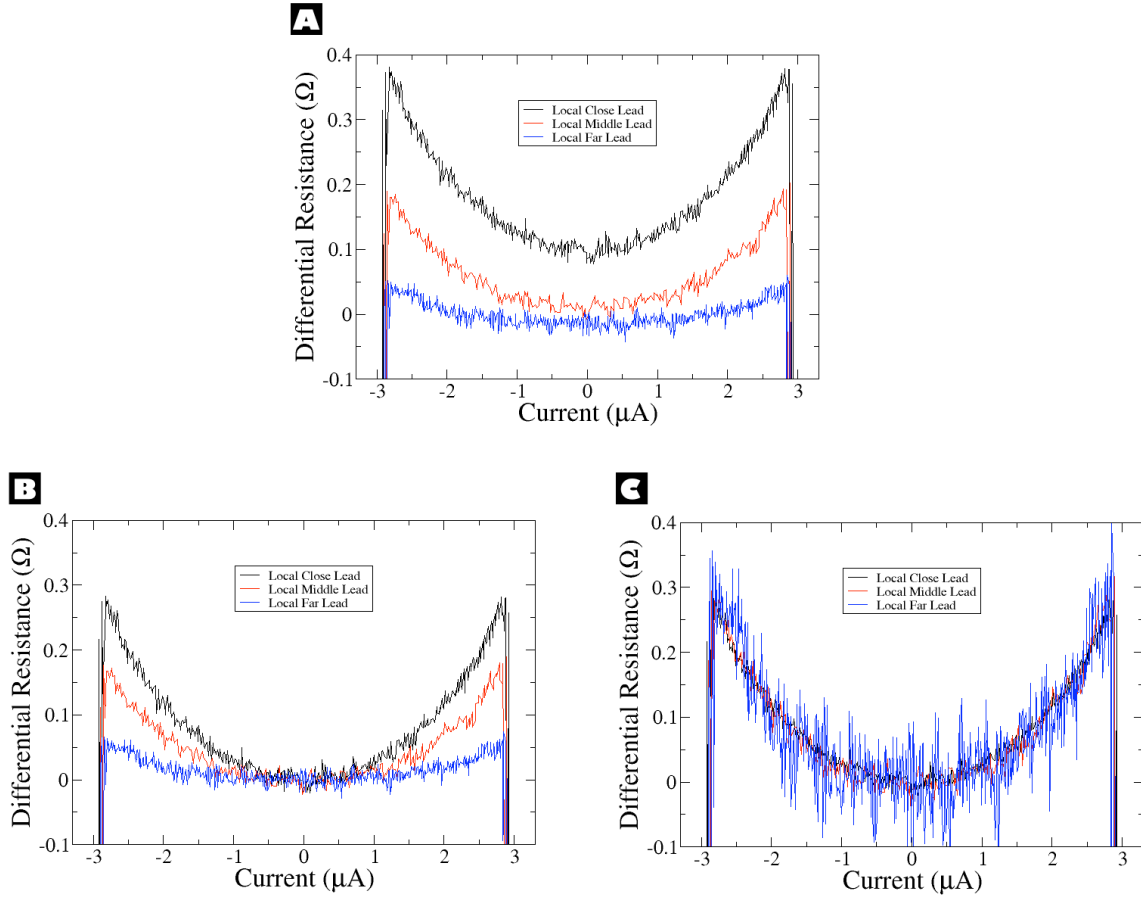


Figure 5.7. As with the linear nonlocal sample the differential resistance of the incoherent loop sample displays two distinct decay lengths for the zero-bias signal and the charge imbalance peak signal. **(A)** Differential resistance of the leads in the local configuration of Fig. 5.5(C) as a function of DC current. **(B)** Curves with the zero-bias subtracted out. **(C)** With the zero-bias removed, the curves can be scaled to each other for currents less than I_c .

was fabricated with the device. Time-reversed quasiparticle paths in the normal metal that are less than a coherence length lead to weak localization [92] corrections to the resistivity of the metal. By suppressing this phase coherent behavior with an external field of strength B and noting the change in the resistance of the wire, we can extract the

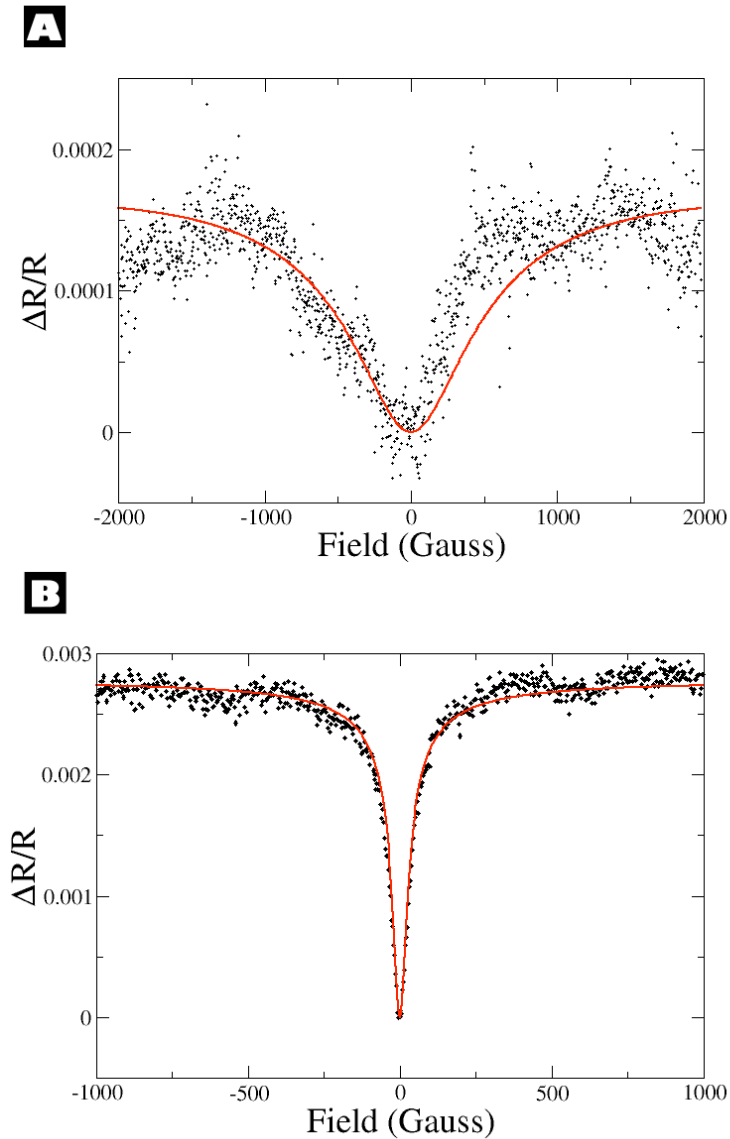


Figure 5.8. Change in magnetoresistance of Au wires demonstrating weak localization. The data (dots) are fit (solid line) using Eq. 5.2 to find the normal metal coherence length l_ϕ . **(A)** A wire co-fabricated with the incoherent ring sample with a 92.4 μm length, 50 nm width, and 50 nm thickness. The poor localization results in a fit yielding $l_\phi = 590$ nm. **(B)** After improvements to the Au deposition process described in Chapter 4, much longer normal metal coherence lengths could be achieved. Shown here is the change in the magnetoresistance of a 502.4 μm wire with 50 nm thickness and 65 nm width fabricated just prior to the coherent ring samples. The weak localization fit yields $l_\phi = 8.12\mu\text{m}$.

phase coherence length l_ϕ using a formula due to Altshuler and Aronov [93]:

$$(5.2) \quad \frac{\Delta R}{R} = \frac{Re^2}{Lh} \left[3 \left(l_\phi^{-2} + \frac{1}{3} \left(\frac{BWe}{\hbar} \right)^2 + \frac{4}{3} l_{so}^{-2} \right)^{-1/2} - \left(l_\phi^{-2} + \frac{1}{3} \left(\frac{BWe}{\hbar} \right)^2 \right)^{-1/2} \right],$$

where L is the length of the wire, W its width, and l_{so} is the spin-orbit length for quasi-particles in Au, which we take to be 85 nm [94]. Fitting to this formula we find an l_ϕ of just over half a μm (Fig. 5.8(A)), shorter than the normal section of the loop. By improvements to our Au deposition process described in Chapter 4, subsequently fabricated wires exhibited l_ϕ 's in excess of 8 μm (Fig. 5.8(B)) and enabled us to make Andreev interferometers with robust quantum coherence.

Fig. 5.9 shows an image and schemata for the first type of nonlocal coherent sample measured. The sample is composed of a hybrid interferometer, a single normal probe located off of the interferometer, but within a few hundred nanometers of one of the interferometer's NS interfaces, and a few additional current and voltage probes. To demonstrate the phase coherent properties of the interferometer, we first use a local measurement configuration (Fig. 5.9(B)) employing a 20 nA AC measurement current to look at its magnetoresistance (Fig. 5.10(A)). As a function of flux through the interferometer loop, the local resistance exhibits oscillations periodic with the superconducting flux quantum $\Phi_0 = h/2e$. These oscillations exhibit non-sinusoidal behavior [95] with a limiting peak resistance that is constant as the amplitude of the oscillations are suppressed with the addition of a DC bias current. Similar behavior has been observed and modeled for the temperature dependence of oscillations observed in Andreev interferometer devices [96]. One other feature of note in the local resistance is a dip in the differential resistance of the interferometer when low, $\lesssim 1\mu\text{A}$, DC currents are added to the AC measurement current.

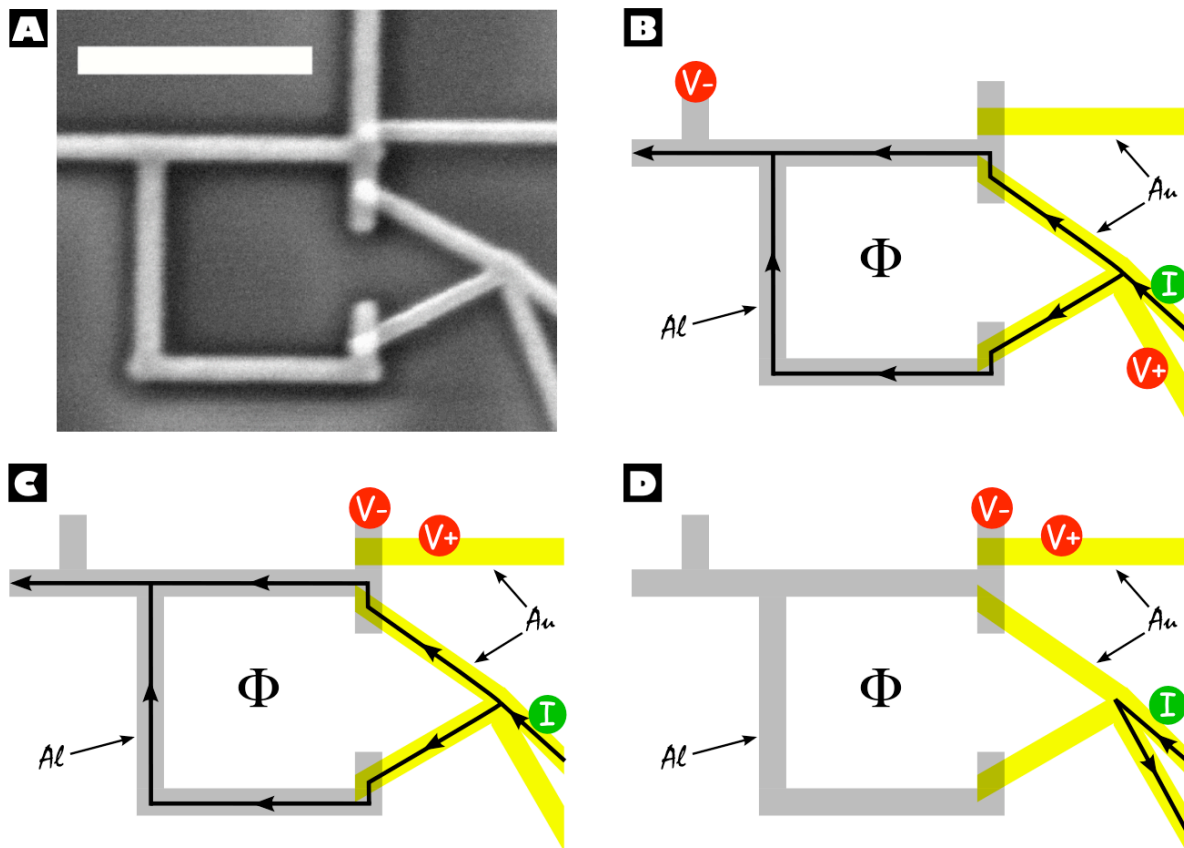


Figure 5.9. (A) Coherent normal-superconducting loop with a single non-local normal lead off of its upper-right corner. The size bar is $1 \mu\text{m}$. (B) “Local” measurement configuration used to measure the resistance and differential resistance of the loop. A flux Φ through the loop can be controlled with an external magnetic field, and a DC current can be added to the AC current path for differential resistance measurements as a function of current bias. (C) “Nonlocal” measurement configuration using the same current path as the local configuration but comparing the potential on the nonlocal normal lead to the condensate potential. (D) “Nonlocal heating” measurement configuration where the nonlocal voltage is measured with current sent through a single point on the loop rather than around it.

As discussed below, currents larger than this bring the device out of the correlation regime set by the Thouless energy E_c and lead to the suppression of interference effects. Though there is a dip in the differential resistance, we note that the measured resistance at the

base temperature of our cryostat remains finite even when the measurement current is reduced.

Proceeding to a nonlocal measurement configuration (Fig. 5.9(C)), we send a 100 nA measurement current into the loop and probe the nonlocal voltage with a normal probe just off of the loop. From the previous experiments with the linear sample and the incoherent loop sample, we would expect to see a zero-bias, low temperature signal on the nonlocal probe, as it is located only a few hundred nanometers from an NS interface across which current is sent. However, in this and subsequently measured coherent loop samples, we observe no zero-bias nonlocal voltage relative to the potential of the superconductor, nor any oscillatory signal periodic in the flux through the loop (Fig. 5.11(A)). The reasons for the absence of such a signal are not clear, but there are two pertinent clues to this mystery. First, the measurement here is identical to the previous measurement on the incoherent loop sample that showed a zero-bias nonlocal signal. The only obvious difference between the samples is that the normal metal phase coherence length l_ϕ is now long enough to encompass the normal segment of the loop. Second, the Thouless energy (Eq. 2.46) for this segment, using $D = 100 \text{ cm}^2\cdot\text{sec}$, corresponds to a temperature of 40 mK. As the Thouless energy sets the scale on which the quasiparticles dephase over the length of the normal arm of the interferometer, the 18 mK temperature at which these measurements were taken is an energy regime where conversion processes at one on-loop NS interface are not completely isolated from the other. Of course, these two factors, long l_ϕ and L_T , are what allow robust Andreev interference effects to be observed in the first place, so that we may be trapped in a situation where our previously observed zero-bias signal disappears just as phase coherent effects start to appear.

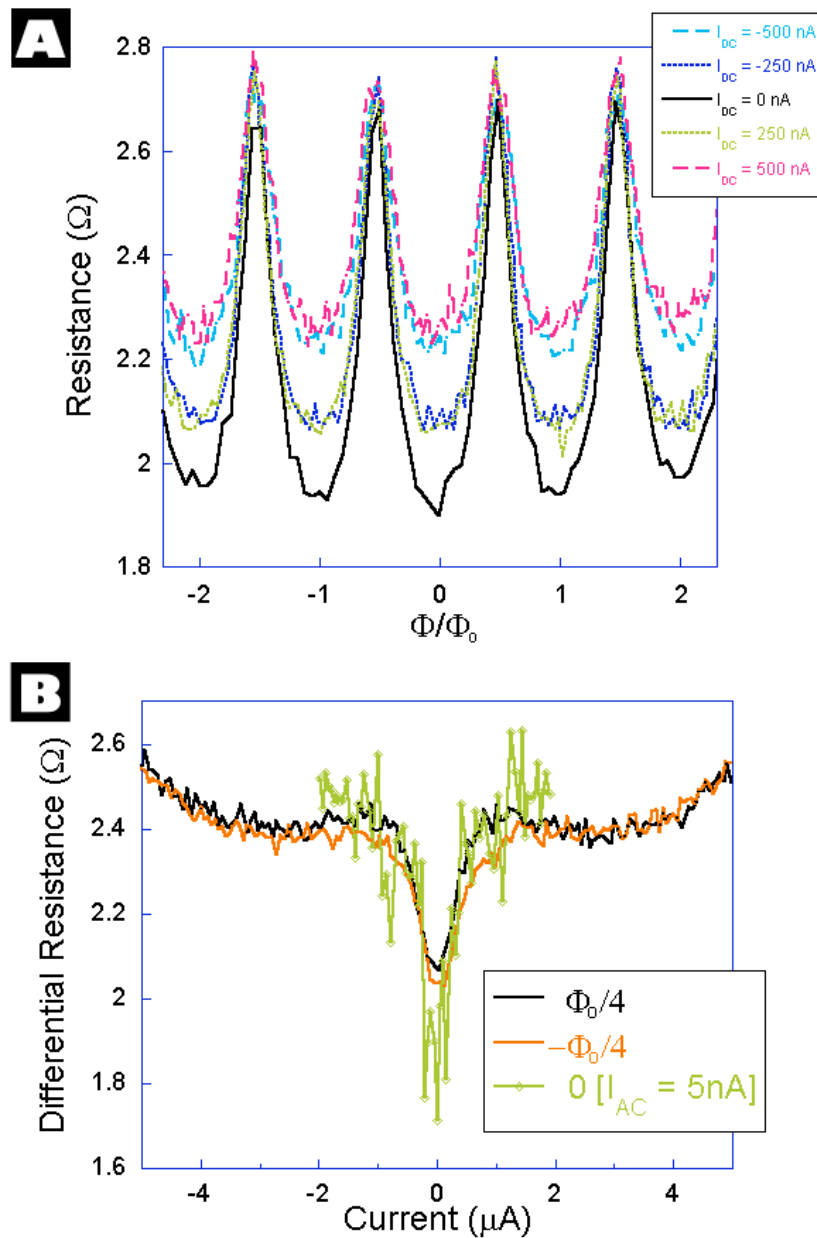


Figure 5.10. Measurements of the single-lead nonlocal coherence sample using the “Local” configuration of Fig. 5.9(B) taken at 18 mK. **(A)** Magnetoresistance of the loop at several different DC bias currents using a measurement current of 20 nA. The flux is measured in units of the superconducting flux quantum $\Phi_0 = h/2e$ which corresponds to a field of 16.75 Gauss. **(B)** Differential resistance of the loop at three different fields. The zero-field trace is taken at a small measurement current of 5 nA to check that the loop maintains a finite resistance even at low currents.

Fortunately, there is another manner of observing nonlocal, phase-coherent effects. By adding a small $\lesssim 1\mu\text{A}$ DC current to our AC measurement current, antisymmetric oscillations arise on the nonlocal probe (Fig. 5.11(A)).³ The origin of these phase coherent oscillations can be surmised from two additional measurements. First, if the DC current is reversed the polarity of the oscillations switches. Second, from Fig. 5.11(B), the same oscillations are present if one does not send any current around the loop, but rather injects the DC and AC currents into a point on the normal section of the loop (see Fig. 5.9(D)). That these dV/dI measurements reverse sign with I indicates that the nonlocal voltage is independent of the direction of the current. That the effect persists when no charge current is sent into the loop indicates that the current serves only to heat the normal part of the loop. The Φ_0 -periodic nonlocal oscillations thus appear to be thermoelectric in origin.

Detailed measurements of the thermopower of Andreev interferometers – where the voltage induced by a thermal gradient along the normal metal arm is measured – have been performed by our research group [97, 98, 99, 100] and others [101, 102]. Interferometers similar in geometry to our design display Φ_0 -periodic thermopower oscillations of the same antisymmetric character as the thermoelectric oscillations seen here. Due to the nonlocal nature of our measurement and the differing thermal gradients, direct comparison with earlier experiments and theory on Andreev interferometer thermopower is difficult. However, in what follows we present measurements on a different sample which indicate that the mechanisms which produce our nonlocal signal may be closely related to the previously observed thermopower oscillations.

³Unfortunately, this measurement run was plagued by intermittent white noise (< 100 kHz) from an undiscovered external source which resulted in large spikes in the data.

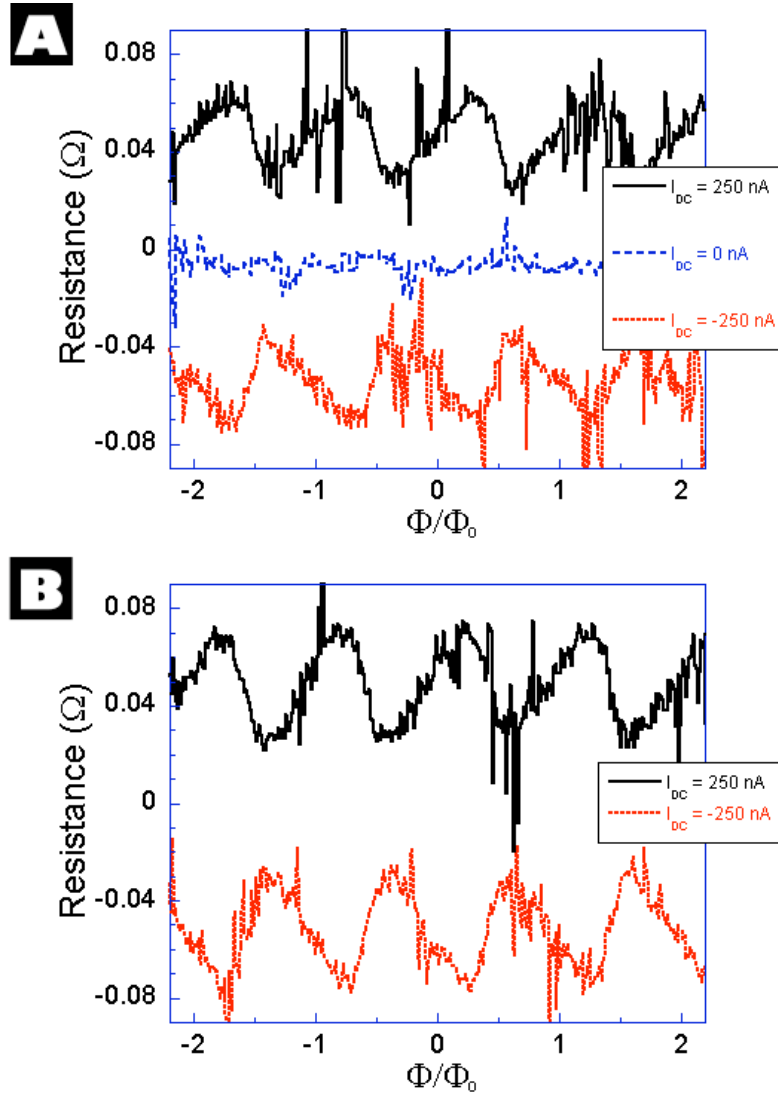


Figure 5.11. Nonlocal oscillations in the single-lead nonlocal coherence sample at finite DC current bias; the data were taken at 18 mK. **(A)** Oscillations seen using the nonlocal configuration of Fig. 5.9(C). The antisymmetric oscillations are only present when a small $\lesssim 1 \mu\text{A}$ DC current is added to the AC measurement current. Unlike the incoherent loop sample, no nonlocal voltage is seen at 0 DC bias. The symmetry of the oscillations reverse when the DC bias is reversed. The finite bias curves are offset by $\pm 50 \text{ m}\Omega$ for clarity. **(B)** Nearly identical oscillations are seen if the currents are sent not through the loop, but only intersect the normal part of the loop at one point, as shown in Fig. 5.9(D). This current path, along with the switching polarity of the oscillations, indicates the voltages are thermoelectric in origin.

The phase coherent nonlocal oscillations disappear as the DC current is increased (Fig. 5.12(A)). The scale over which this decay occurs matches the scale of the differential resistance dip seen in the local measurement of the interferometer, which, we discuss below, is the same current scale over which the device should be pushed out of the correlation regime. The attenuation of the oscillations can also be observed by biasing the flux at $\pm\Phi_0/4$, where the magnitude of the differential resistance is greatest, and sweeping the DC current. As shown in Fig. 5.12(B), the two flux biases display opposite polarities until the signals start to coincide above $\pm 2\mu\text{A}$. Since this measurement is performed using the configuration of Fig. 5.9(C), the current across the NS interfaces on the loop creates a charge imbalance signal on the nonlocal lead that accounts for the increasing background as the current is increased.

The nature and cause of the nonlocal coherent oscillations can be further illuminated by examining a similar device design that is fabricated with additional normal metal probes. Shown in Fig. 5.13(A) the sample consists of an Andreev interferometer with two nonlocal probes, each located 210 nm from the on-loop NS interfaces. There are also two normal probes located on the corners of the interferometer at these interfaces. We label these normal voltage probes with superscripts “T” and “B” to distinguish between top and bottom, and subscripts “N” and “C” to distinguish between the nonlocal and corner probes. Overall, this device exhibits behavior that is consistent with the previous design. From Fig. 5.13, local measurements of the loop reveal large flux-periodic resistance oscillations and a dip in the differential resistance at low DC bias currents. We also show that the resistance of the loop undergoes an analogous dip at temperatures below 70 mK. Again, this temperature scale is comparable to the 30mK value set by the Thouless

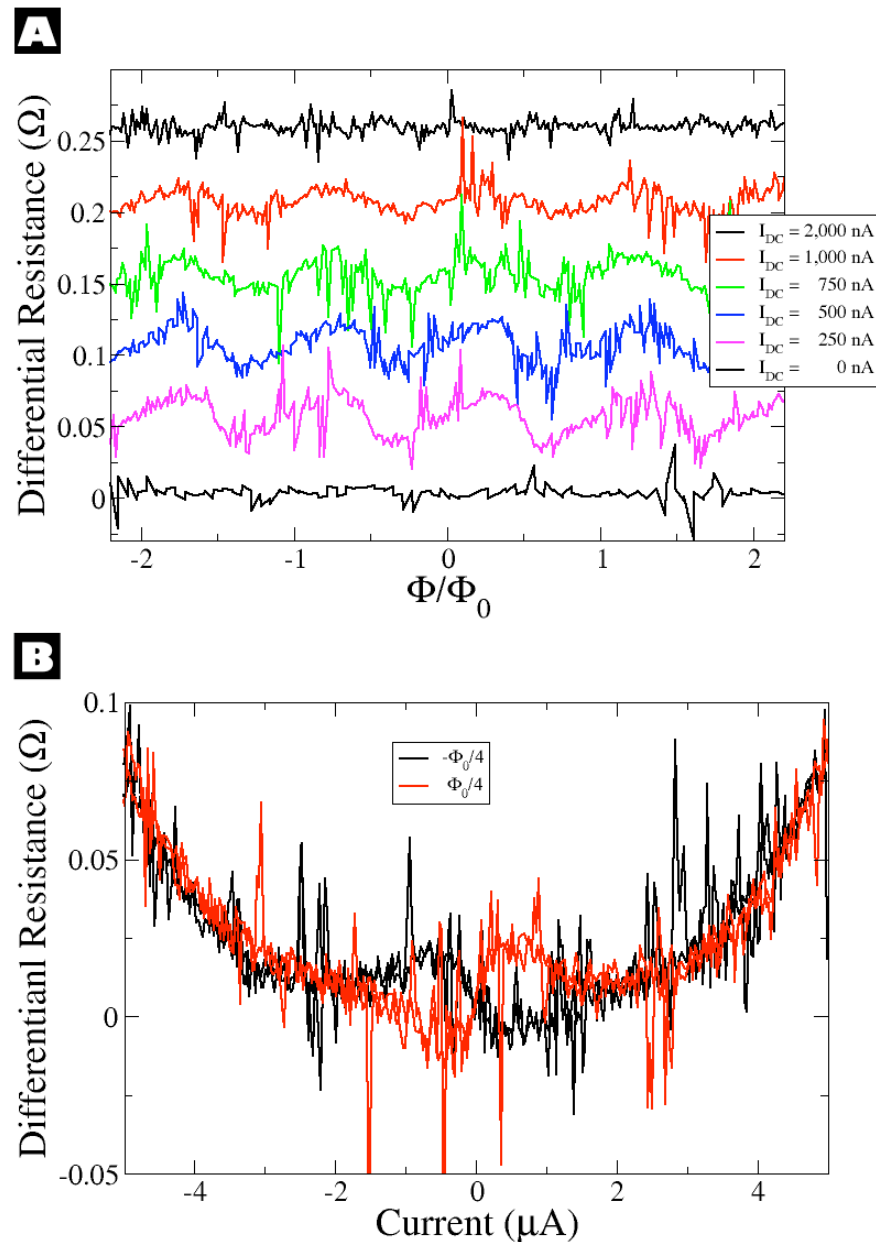


Figure 5.12. Decay of the nonlocal coherent signal using the nonlocal configuration of Fig. 5.9(C), taken at 18 mK. **(A)** As the DC bias is increased the oscillations die out. **(B)** Alternately this decay can be observed by biasing the field at $\pm\Phi_0/4$ and sweeping the current. The antisymmetric nature of the phase-coherent signal distinguishes it from the background charge imbalance which is symmetric with respect to the DC current. Note that the decay of the coherent signal is observed over the same range as the sharp dip in the local differential resistance of Fig. 5.10(B).

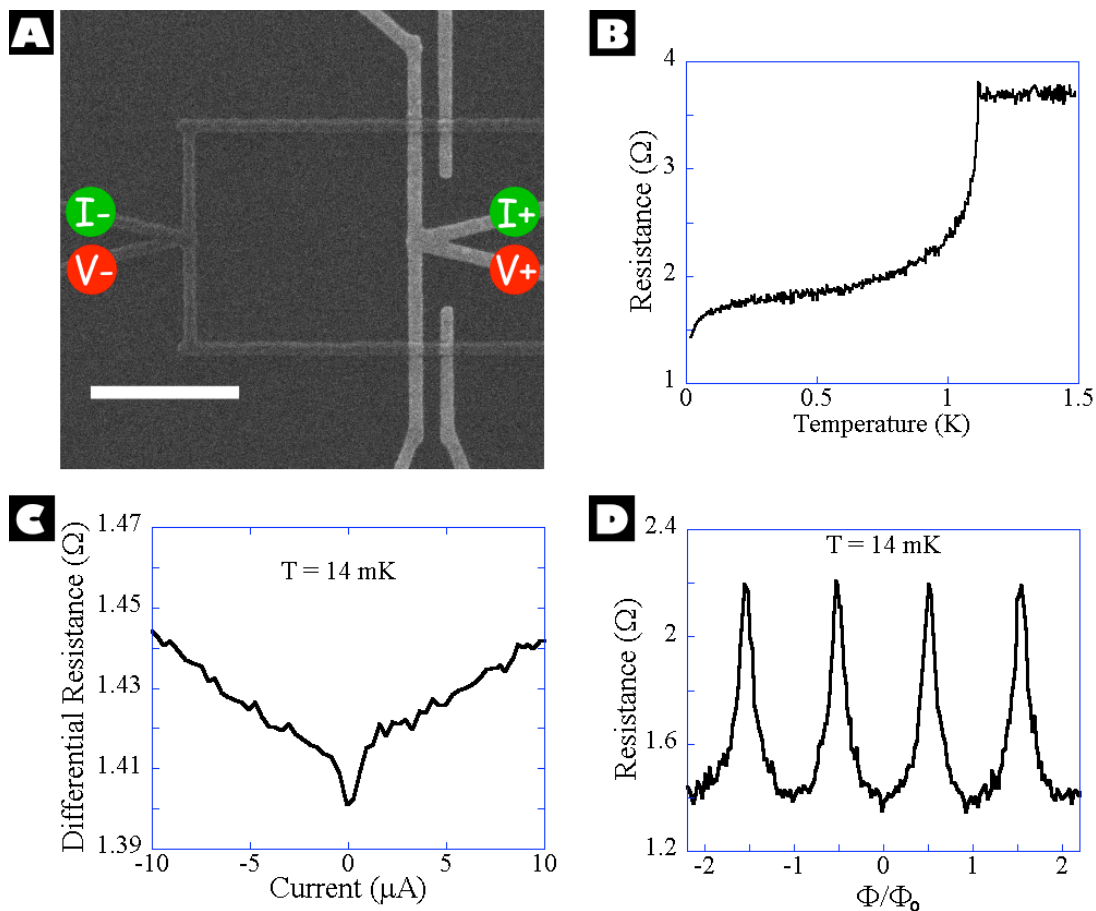


Figure 5.13. (A) Scanning electron micrograph of a multiple-lead nonlocal coherence sample; the size bar is $1 \mu\text{m}$. This geometry has two nonlocal normal metal probes in addition to two probes on the corner of the hybrid normal metal-superconductor loop. The current-voltage configuration marked is used to measure the local properties of the loop with a 20 nA AC measurement current. (B) Resistance of the loop as a function of temperature. At the Al T_c of 1.2 K the loop resistance decreases followed by a regime where the resistance change is dominated by charge imbalance and the proximity effect. At 70 mK, near the Thouless energy, the resistance starts to drop much more quickly, though it remains finite down to the lowest measurement temperatures. (C) Differential resistance of the loop as a function of DC bias showing a sharp low-bias dip corresponding to the low-temperature resistance dip. The behavior is identical to the analogous measurement of the single-lead nonlocal sample shown in Fig. 5.10(B). (D) Local resistance oscillations, similar to those of Fig. 5.10(A).

energy for the normal section of the loop in this device, which has a $1.7 \mu\text{m}$ length and $110 \text{ cm}^2\cdot\text{sec}$ diffusion constant.

Most of the nonlocal measurements of this multiple-lead nonlocal coherence sample use the heating configuration shown in Fig. 5.14(A), analogous to the configuration of Fig. 5.9(D) for the single-lead sample. This configuration has the virtue of not directly sending any current across the NS interfaces of the device, which avoids producing conventional charge imbalance signals even at high currents. As with the single lead device, nonlocal oscillations referenced to the superconductor potential are present on the off-loop leads when a small DC current is added to the 100 nA AC measurement current (Fig. 5.14(B)).⁴ Yet the additional leads provide us with some new information. Using the same current configuration the signals on all four leads can be measured relative to the condensate potential (Fig. 5.15). Comparing V_C^T and V_N^T , the same oscillations are present on both probes, but the amplitude of the oscillations are six times smaller on the nonlocal probe, attenuating rapidly over a length scale $\lesssim \xi_S$.

We have thus demonstrated a quasiparticle signal that 1) occurs on two spatially separate probes placed on a superconductor, 2) is nonlocal; there is no current sent between the probes, 3) attenuates rapidly from one probe to the other, on the order of ξ_S or faster, and 4) is phase coherent and can be tuned using an external flux. These criteria satisfy our goal of finding an effect that conforms to the predicted aspects of EC and CAR laid out at the beginning of this chapter.

⁴The perceptive reader will note that the nonlocal oscillations of the single lead device in Fig. 5.11 are of opposite polarity to the analogous oscillations of the multiple lead device exhibited in Fig. 5.15(B). This apparent discrepancy stems from the fact that the single lead device is measured in the Oxford Instruments Kelvinox MX100 cryostat, which is wired with the convention that a positive field or flux points out of the page, while the multiple lead device is measured in the Oxford Instruments Kelvinox 300 where a positive field or flux points into the page.

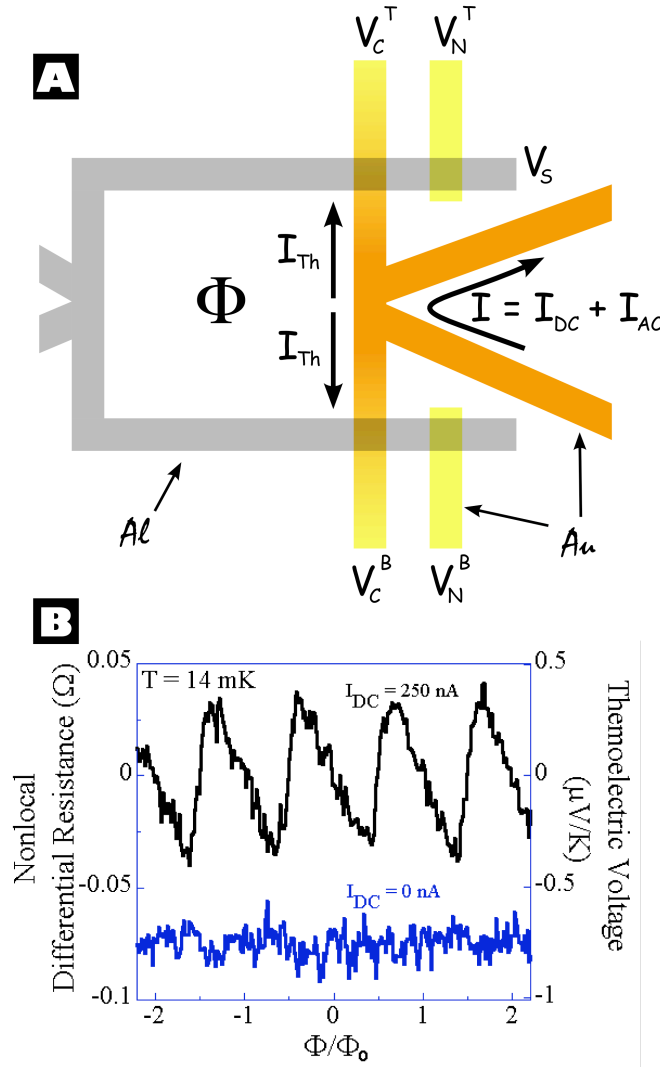


Figure 5.14. **(A)** Nonlocal measurement configuration of the sample shown in Fig. 5.13(A). The configuration is analogous to the nonlocal heating configuration (Fig. 5.9(D)) of the single-lead sample where a DC heating current creates thermal gradients along the normal part of the loop. In this sample four normal leads can be used to probe the thermoelectric oscillations: two nonlocal leads (subscript “N”) at the top and bottom of the loop (superscripts “T” and “B”) and two leads on the corners of the loop (subscript “C”). The voltage on these probes is always referenced to the superconducting condensate potential V_S . **(B)** Differential magnetoresistance on the V_N^T lead with and without a DC heating current. The oscillations are analogous to those in the single nonlocal lead sample shown in Fig. 5.11.

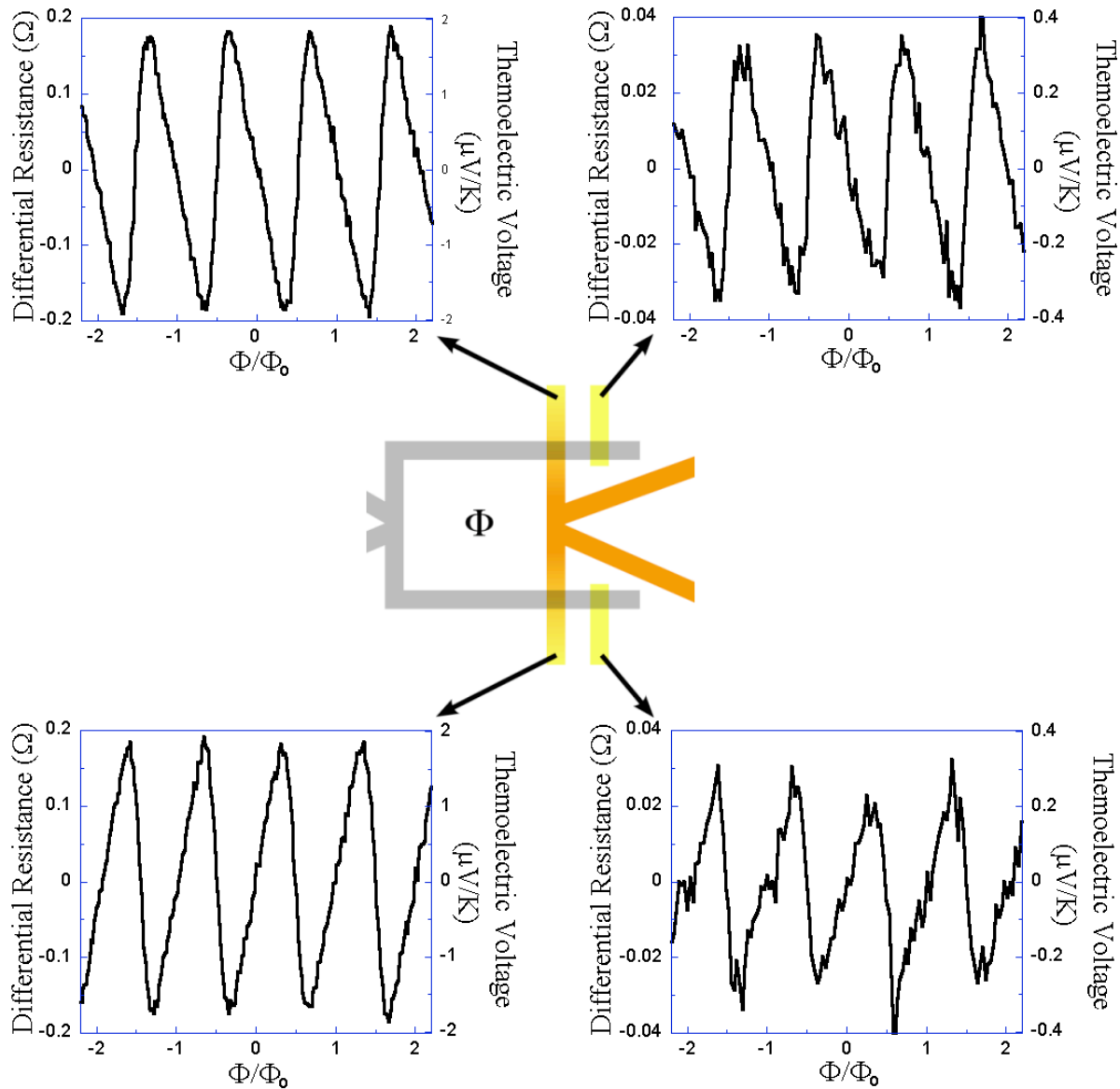


Figure 5.15. Thermoelectric oscillations on the four probes of the multiple-lead sample. An identical 250 nA DC heating current and 100 nA AC measurement current is used for all four measurements using the configuration shown in Fig. 5.14(A); all traces are taken at 14 mK. The magnitude of the thermoelectric voltages shown on the right-hand ordinates is referenced to the temperature at the center of the normal section of the loop calculated from a heat flow model.

5.4. Thermoelectric Oscillations

Though we have reached our goal, several serious mysteries remain. First and foremost, what is the physical mechanism that creates this thermoelectric signal? A clue is provided on noticing that while the same attenuation occurs between the V_C^B and V_N^B probes as between V_C^T and V_N^T , the signals seen at the top and bottom of the interferometer are of opposite polarity. This is surprising since the geometry of the device is symmetric about its horizontal axis, and the signals are independent of the direction of the heating current sent to the center of the normal section of the loop. The only dynamic mechanism that could cause the reversal in polarity between the two signals is a thermodynamic persistent current around the loop induced by the external flux. Additional evidence for the role of a persistent current in producing the observed voltages can be found in the sawtooth shape of the signals, which corresponds to the functional form of theoretically predicted persistent currents in NS rings where the superconducting section is much longer than both the normal section of the loop and the superconducting coherence length [103, 104]. We follow the latter reference in identifying the persistent current in this limit with Josephson currents found in linear SNS devices.

Further clues to the origin of the observed oscillations, and the interaction between the thermal gradients produced by the DC heating current and the polarity-determining persistent Josephson current, can be found by examining a series of alternate measurement configurations, shown in Fig. 5.16. All measurements use a 100 nA AC measurement current and a 250 nA DC heating current sent along the marked path. Configurations a) - e) all record the signal on the nonlocal V_N^T lead referenced to the condensate potential with different heating current paths. While the observed oscillation amplitude varies,

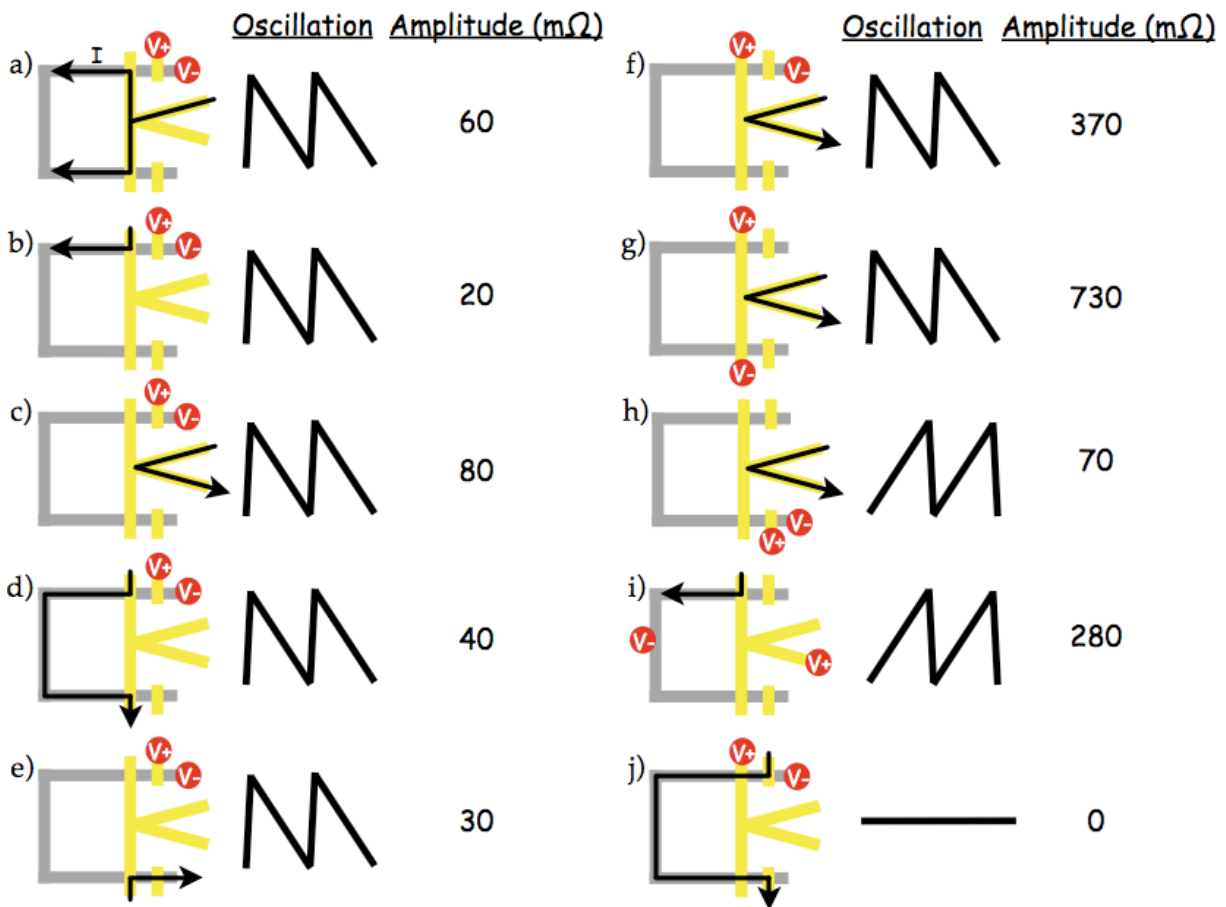


Figure 5.16. Alternate measurement configurations for the multiple-lead sample along with the polarity and amplitude of the observed oscillations when using a 250 nA DC heating current and 100 nA measurement current. a) - e) show that oscillations are present on the V_N^T lead as long as the DC current flows along any part of the normal lead that completes the interferometer. f) & g) are the large corner oscillations. h) is the reversed polarity at the bottom of the loop. i) demonstrates that the oscillations can also be observed at the center of the interferometer. j) indicates that the oscillations are not present when current is injected into the nonlocal leads.

the polarity of the oscillations are all identical. These paths suggest that the direction of the thermal gradients produced may be unimportant in determining the polarity of the oscillations. Of particular note are configurations b) and e), which heat the V_C^T

and V_C^B leads respectively. These two configurations should result in thermal gradients traveling opposite directions along the normal part of the interferometer, but the observed oscillations are similar in polarity and magnitude.

The measurements in these two configurations also argue against the nonlocal signal being due to any direct heating of the nonlocal leads. While bulk superconductors are excellent thermal insulators, there is an exponential dependence of electronic heat conduction through a superconductor governed by the magnitude of the superconducting energy gap [105]. This dependence, coupled with uncertainties regarding the behavior of this gap in the inverse proximity regime between the corner and nonlocal leads, makes it difficult to argue with theoretical certainty that heating currents on the interferometer do not also heat the nonlocal leads. However, the fact that configurations b) and e) display oscillations of a similar amplitude, though the heated section of the latter configuration is separated from the nonlocal voltage probe by an additional $1.7 \mu\text{m}$ length of Au wire, indicates that the existence of the oscillations is not dependent on direct heating of the nonlocal probes. Further empirical support for the claim that there is minimal heat transport between the corner and nonlocal leads is found in configuration j). Configurations a) - e) and h) show that any heating of the loop produces nonlocal oscillations, while configurations f) and g) show that the same oscillations are much larger when observed with the corner voltage probes. If the superconductor provided a modicum of thermal transport between the nonlocal and corner leads, heating the nonlocal leads should heat up the loop, which should produce oscillations that will be largest when measured with the corner probes. The absence of oscillations in configuration j) shows this is not the

case, and adds weight to the claim that the nonlocal leads are not being heated in any of the other configurations.

To compare these oscillations with the earlier work on the thermopower of Andreev interferometers, it will be helpful to translate our differential resistance measurements into the voltage/Kelvin units used to measure thermopower. As we have just remarked, the oscillations in our sample can be seen using a number of different current paths producing a number of different thermal gradients. For simplicity we return to the configuration of Fig. 5.16 and 5.17 and take the temperature increase at the center of the normal section of the interferometer to be the relevant temperature change.

To calculate this change, we follow the modeling procedure of [72] and use an equation for steady-state heat flow in normal metal wires written down by Nagaev [106]:

$$(5.3) \quad \left(\frac{eV}{L}\right)^2 + \frac{\pi^2}{6} \frac{d^2(T_e^2)}{dx^2} - \Gamma(T_e^5 - T^5) = 0,$$

where L is the length of the wire, T_e is the local electron temperature, T is the phonon temperature of the substrate, and Γ is a parameter that is dependent on the strength of the electron-phonon scattering. In this equation the first term arises from Joule heating, the second from the electron-electron thermal transport in the Sommerfeld approximation, and the third term from the electron-phonon interaction. For boundary conditions, we assume that where the Au wires widen to 500 nm they act as a thermal reservoir at the base temperature of the refrigerator, which we also take to be the temperature of our substrate phonons. The only other unknown parameter of Eq. 5.3 is the electron-phonon constant Γ . Using noise measurements, Henny *et. al.* have experimentally found $\Gamma \simeq 5 \times 10^9 \text{ K}^{-3} \text{ m}^{-2}$ for diffusive Au wires of varying lengths [107]. As the resistivity

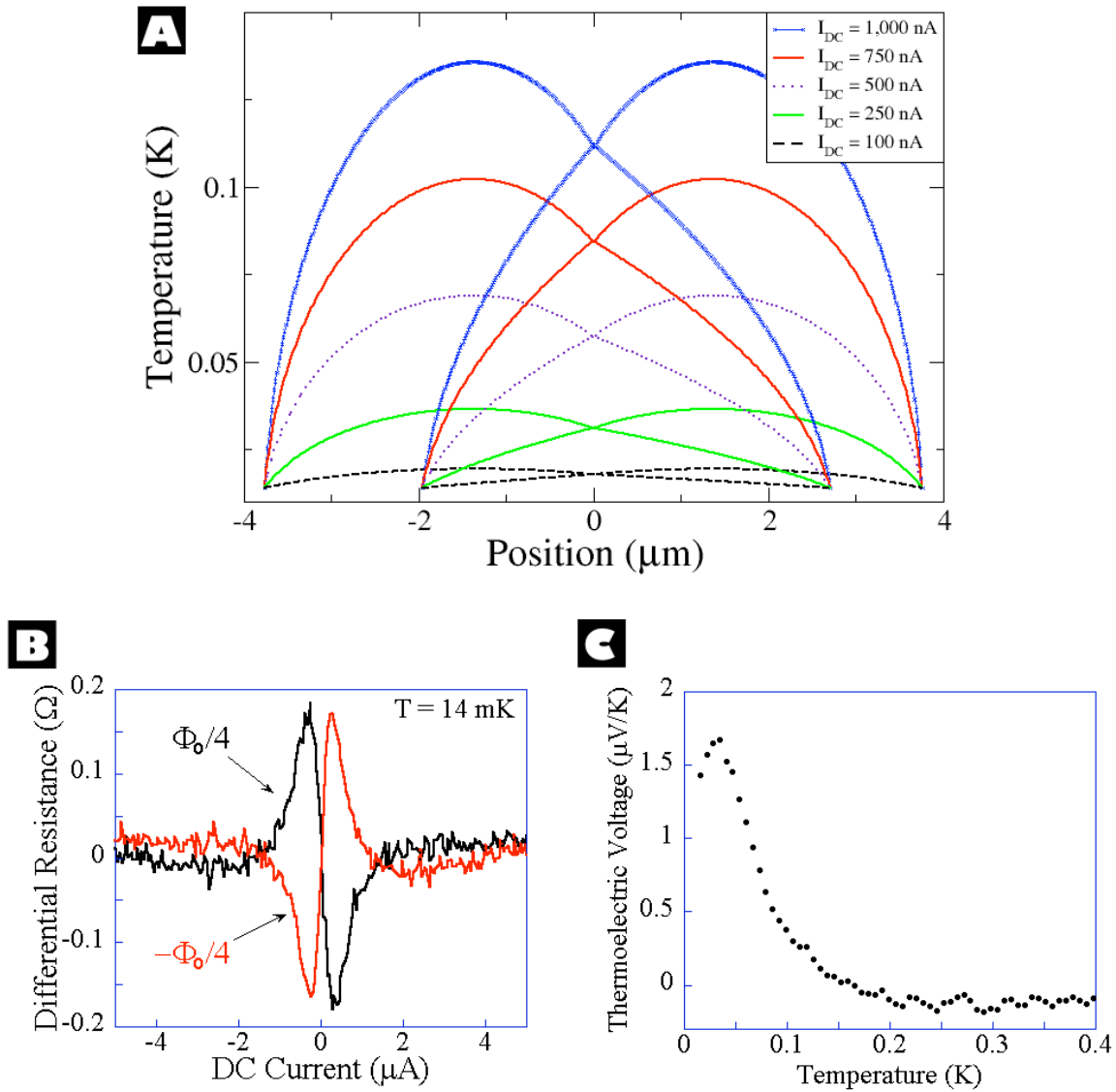


Figure 5.17. (A) Theoretical temperature profile of the Au leads on the multiple-lead nonlocal coherence sample for different DC heating currents. The upper part of each curve is the profile of the current path leads and the lower part is the profile of the normal metal section of the loop. 0 position corresponds to the intersection of these leads. (B) Differential resistance of the V_C^T lead when biased at $\pm\Phi_0/4$ flux. The trace shows the DC current dependence of the amplitude of the thermoelectric oscillations. (C) Using the theoretical temperature vs. current curves of (A) and amplitude vs. current curves of (B) a plot of the thermoelectric oscillation signal vs. temperature can be constructed. The amplitude peaks at 30 mK, identical to the temperature scale set by the Thouless energy.

of their measured wires is almost identical to ours, we use their value of Γ in Eq. 5.3. In modeling T_e along the wires, we have ignored corrections due to incomplete thermalization of the electrons in our wires [109]. We address this possibility below.

Simulations of the temperature profiles of the heating leads and normal section of the loop for different DC heating currents are shown in Fig. 5.17(A). The profile is numerically calculated with the relaxation method and a Newtonian minimization routine in the IDL programming language [108]. There is a slight asymmetry in the curves due to the different distances at which the 80 nm wires widen to the 500 nm reservoirs. Using the calculated temperature at the center of the normal section of the loop we can construct a theoretical $T(I)$ curve, numerically differentiate it, and use the relation [98]

$$(5.4) \quad \frac{dV}{dT}(I) = \left(\frac{dV}{dI}(I) \right) / \left(\frac{dT}{dI}(I) \right)$$

to convert our differential resistance (dV/dI) measurements into the units of thermoelectric voltage per unit temperature. The results of this conversion are shown on the right-hand ordinates of the magnetoresistance oscillations in Fig. 5.14 and 5.15.

We can also use this conversion to plot the amplitude of the thermoelectric oscillations as a function of temperature. Making a measurement similar to that of Fig. 5.12(B) for the single-lead sample, we can bias the flux at $\pm\Phi_0/4$, where the oscillations are at their extrema, and trace out the amplitude of the oscillations as a function of DC bias current. Shown in Fig. 5.17(B), this measurement differs from the one performed on the single-lead sample in two ways. First, we use the corner V_C^T lead rather than a nonlocal lead to get a larger signal. Second, since the heating leads are used, there is no current across an NS interface, and hence, no charge imbalance background. From our

heat flow model and Eq. 5.4 we convert the differential resistance vs. current curve for the $\Phi_0/4$ trace into a thermoelectric voltage vs. temperature trace (Fig. 5.17(C)). This trace reveals that the coherent oscillations experience a maximum at 30 mK, identical to our calculated correlation energy. Our current-temperature conversion model has thus enabled us to establish that the $\sim \pm 1 \mu\text{A}$ current range over which the oscillations are robust corresponds to the energy range set by E_c .

The thermoelectric oscillation amplitude measured and calculated on the corner leads is comparable in magnitude to the $4 \mu\text{V/K}$ values found for the thermopower of Andreev interferometers measured and calculated by Eom *et. al.* [97]. As noted in [98], where Andreev interferometer thermopower is measured more directly using on-chip thermometers, this magnitude may be somewhat high due to the simplicity of the heat flow model employed. However, given that the same model employed here is used by Eom *et. al.*, the similarity in magnitude between the Andreev interferometer thermopower values of this reference and the thermoelectric signal we see here, coupled with the similarity between the antisymmetric nature of the phase coherent oscillations, lends credence to the idea that the same physical mechanisms account for both effects. We can then hope that theoretical explanations of this earlier work might be applied to our observations.

The closest configuration to a pure thermopower measurement possible with our device is shown in Fig. 5.16 g). In a thermopower measurement, the same voltage leads would be used, but the current heating leads on the normal metal wire would be outside the interferometer rather at its center. This fact leads to great difficulties in applying theoretical studies of Andreev interferometer thermopower to the signals we observe here. Past works [110, 111, 112, 113, 114, 14, 115] which attempt to model the thermopower results, all

rely on an *asymmetric* temperature profile in the measurement to derive antisymmetric oscillations, while we observe similar antisymmetric oscillations with a *symmetric* temperature profile. Moreover, as noted above when discussing the b) and e) configurations of Fig. 5.16, it appears that even when an asymmetric temperature profile is produced the polarity of the oscillations are unchanged if the profile is reversed, in contradiction to the theoretical models. Rather than using the theoretical understanding of Andreev interferometers to clarify our measurements, our measurements have served to confuse the theoretical understanding.

5.5. Coexistence of Normal and Superconducting Current

There is, however, one apparent mystery regarding our measurement of nonlocal coherent oscillations, that we can shed some light on. Namely, why, if our Andreev interferometer is supposedly supporting a circulating Josephson current, does the interferometer have a finite resistance? The answer lies in the observation that we have sent a normal-metal quasiparticle current into the normal section of the interferometer to measure its resistance. Even though a supercurrent can travel through this normal section without resistance, a quasiparticle current sent into this section will experience resistance until it converts to a supercurrent at the NS interfaces.

To experimentally confirm this claim, we fabricate a plain SNS Josephson junction that enables 4-terminal measurements of both the entire junction (using superconducting probes) and part of its normal section (using normal metal probes). Shown in Fig. 5.18(A) the junction is a 120 nm wide wire with the normal section $1\mu\text{m}$ in length. By using two different 20 nA AC measurement currents with frequencies of 37 and 85 Hz, we can

simultaneously measure the resistance of the whole wire and its normal part as a function of temperature (Fig. 5.18(B)). Examining the resistance of the whole wire, we note that just under 0.8 K there is an inflection point signaling the onset of a Josephson current. As the temperature is lowered the critical value of this current increases until it exceeds our measurement current at 0.6 K and the resistance falls to 0Ω . The measurement of the normal section, though, remains finite down to base temperature – a direct demonstration that a quasiparticle current and Josephson current can coexist in the same normal metal.

The R vs. T curve for the normal metal section, while always presenting a finite resistance, does show a dramatic change in the measured resistance over the same temperature range that the Josephson current develops in the device. Analogous resistance changes, predicted by S. Guéron [117], have been observed in other SNS Josephson junctions which have an additional normal wire (a “dangling arm”) used to inject quasiparticle current into the normal junction [116, 15]. In these devices the resistance of the dangling arm in series with part of the normal junction undergoes an apparent drop when the Josephson current appears. The origin of this effect can be understood using a simple phenomenological model first presented in [117], which we adopt to explain the measured resistance drop of our normal segment.

Considering only the normal metal I+ and I- leads used to inject quasiparticles, we first note that, since the normal metal has some finite quasiparticle resistance, there is a potential drop between these two leads. We next note that if there is a Josephson current between them, the potential of the two superconductors must be the same, though their phases may be different. This leads to the following question: what is the relation

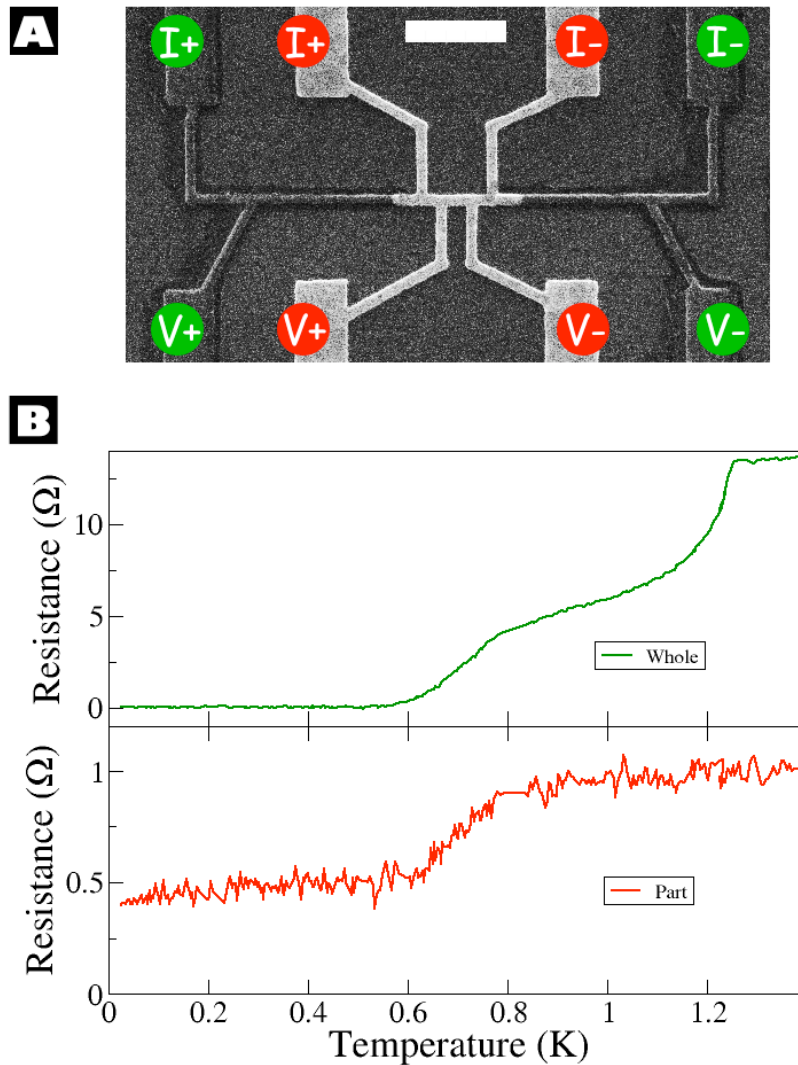
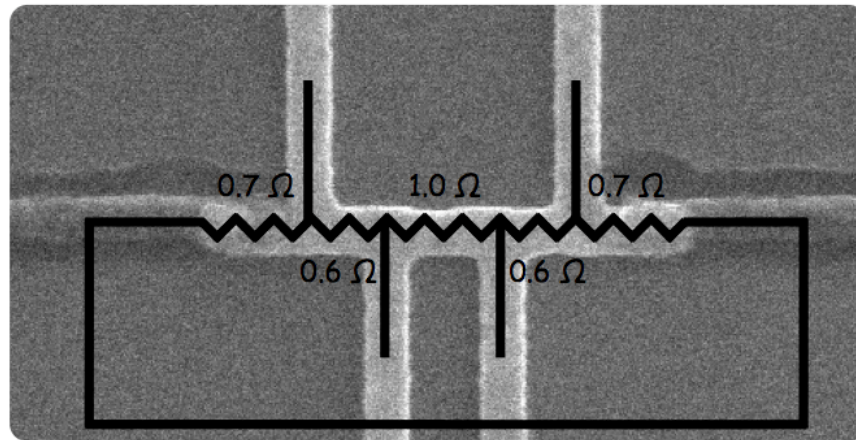


Figure 5.18. (A) Scanning electron micrograph of a superconductor-normal metal-superconductor wire; the size bar is $1 \mu\text{m}$. Using the outer, superconducting leads, the 4-terminal resistance of the entire wire can be measured. Simultaneously, with a different AC measurement frequency, the resistance of part of the middle normal section can be made using the inner, normal leads. (B) Resistance vs. temperature for the whole wire (top) and the normal part (bottom). Just below 0.8 K a Josephson current begins to appear between the two superconductors, eventually reaching a magnitude larger than the 20 nA measurement current at 0.6 K where the resistance of the entire wire goes to zero. Over this same range the measured resistance of the part of the middle normal segment drops by half.

between the superconductor potential and the potentials at I+ and I-? If the superconductor potential is higher than these potentials there will be a net current from both superconductors into the central normal section. If the superconductor potential is lower than these potentials there will be a net current out of the central normal section into the two superconductors. Since the measurement setup does not allow the superconductors to act as either a current source or sink, we can rule out these possibilities and conclude that the superconductor potential is between the potential at I+ and I-.

In this case, current entering from the I+ lead can flow to a lower potential by traveling either to the right or the left. Similarly, current flowing into the I- lead can enter from either the right or the left. The net result of these current paths is a charge flow into the left superconductor and out of the right superconductor. As there can be no net charge flow into or out of these superconductors, there must be a compensating Josephson current flowing from the left superconductor to the right one. This current flow path can be described more suggestively as follows: current flowing in from the I+ lead can either travel the conventional quasiparticle path along the normal metal, or can travel toward the left superconductor, convert to a supercurrent, travel as a Josephson current to the right superconductor, travel to the left again into the normal metal while converting back to a quasiparticle current, and exit through the I- lead. The actual resistance of the normal section may not change, but since only a fraction of the measurement current actually traverses the voltage probes as a quasiparticle current, measured resistances can be dramatically different.

We can make a simple model accounting for these current paths by representing the normal section of the SNS wire as a resistor with its ends shorted together by the Josephson



	<u>Model</u> (mΩ)	<u>Measured</u> T = 20 mK = 200 mK					
	389	372	445		-136	-222	-294
	194	170	219		-253	-349	-447
	194	201	220		-447	-555	-668
	289	314	383		-447	-551	
	289	316	369		-217	-213	
	389	382	442		-136	-229	-302

Figure 5.19. When a Josephson current is present, measurements of the normal section can be approximated by representing the normal section as a resistor with the ends shorted together. The values of the resistances are estimated from measurements of a co-fabricated Au wire and NS interface. The measured and predicted values of twelve different configurations are shown below. For configurations where both V+ and V- leads are normal, the predicted value is quite accurate at 20 mK. For higher temperatures and other configurations, the model predicts the correct sign, but gives too small a magnitude.

current path. Shown in Fig. 5.19, the resistance values of the different parts of the normal section are calculated using the geometry of the device along with measurements of a simultaneously fabricated normal wire and an NS interface. Using this model, the measurement of the central part of the normal section recorded in Fig. 5.18(B) should be 1Ω when there is no Josephson current in the device and $390\text{ m}\Omega$ when there is. These values correspond almost exactly with the measured high and low temperature limits.

Though Fig. 5.19 shows that the simple resistor model is quite accurate for a variety of measurement configurations used at 20 mK, the measured and predicted values start to diverge as the temperature is increased. While it is not surprising that such a simple model fails, what is surprising is the way in which it fails. We would expect that the resistance of the normal section should undergo changes due to processes such as the proximity effect as the sample is cooled. Indeed, aside from the large drop in the 0.6-0.8 K range, there is a gradual decrease in the measured resistance with temperature. What is unexpected is that in the low temperature limit, where the proximity effect would be robust, the model using the plain normal state resistance would be most accurate. It is possible that re-entrance effects previously observed in proximity coupled normal metals could exactly compensate the changes to the normal metal resistance at the lowest temperatures, though typically a return to the high temperature resistance is not observed [118, 13, 119]. A second discrepancy between the resistor model and experiment evident in Fig. 5.19 is that when one of the voltage probes is on the superconductor, the model fails by a significant amount even at the lowest temperatures.

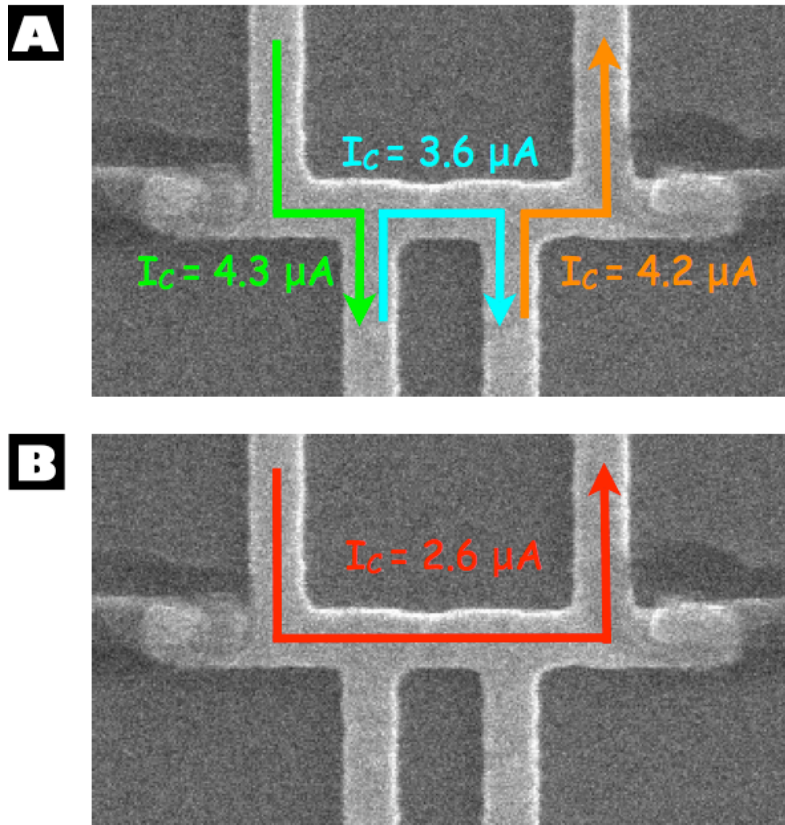


Figure 5.20. SNS critical current paradox. The Josephson current between the superconductors can be suppressed by sending a DC current through parts of the normal section. **(A)** When sent through three different segments of the normal section this critical current exceeds $3.6 \mu\text{A}$. **(B)** However, when the current path is the sum of these three sections, the critical current is only $2.6 \mu\text{A}$.

Data from the dangling arm experiments also showed discrepancies with phenomenological models similar to the resistor model discussed here [116, 15]. For these experiments, current sent along the dangling arm into one of the superconductors was found to suppress the Josephson current at some critical value. Following [15], we designate this current by I_c^{NS} , use I_c^{SNS} for the critical current found when current is sent from one superconductor to the other, and introduce I_c^{NN} to designate the critical current when

the current travels from one normal lead to another. The suppression of the Josephson current using current injected from a normal lead can be partially accounted for by noting that some fraction of the injected current will always follow the Josephson path of our resistor model. When this fraction of the injected current reaches I_c^{SNS} the coupling between the two superconductors is halted. This suppression through the Josephson path can qualitatively explain the paradox shown in Fig. 5.20, where the observed I_c^{NN} critical current for three normal segments is larger than the I_c^{NN} for the three segments put together. Qualitatively, the exact values of the measured I_c^{NN} are smaller than one would predict if Josephson path suppression were the only explanation. Both [116] and [15], noted similar failures using their phenomenological models to predict measured values for I_c^{NS} in the dangling arm devices and posited the existence of additional mechanisms by which the quasiparticle current suppresses the Josephson current.

We can separate out the critical current effects due to the Josephson path and any additional quasiparticle suppression by measuring the I-V curves for the entire SNS junction while injecting additional quasiparticle current from the normal leads (Fig. 5.21). To do so we use the measurement set-up of Fig. 4.8. Injected current that follows the Josephson path will cause a shift in these IV curves, while suppression due to the quasiparticle current will reduce the width of the superconducting plateaus. The shifts in these curves are in reasonable agreement with what one would anticipate from the resistor model, with larger shifts corresponding to a longer ostensible current path on the normal metal. What is unusual is the amount of suppression that occurs for the different injected current routes. The smaller suppression of (Fig. 5.21)(A) compared with (B) and (C) might be explained by noting that for a given injected current, very little quasiparticle current travels the

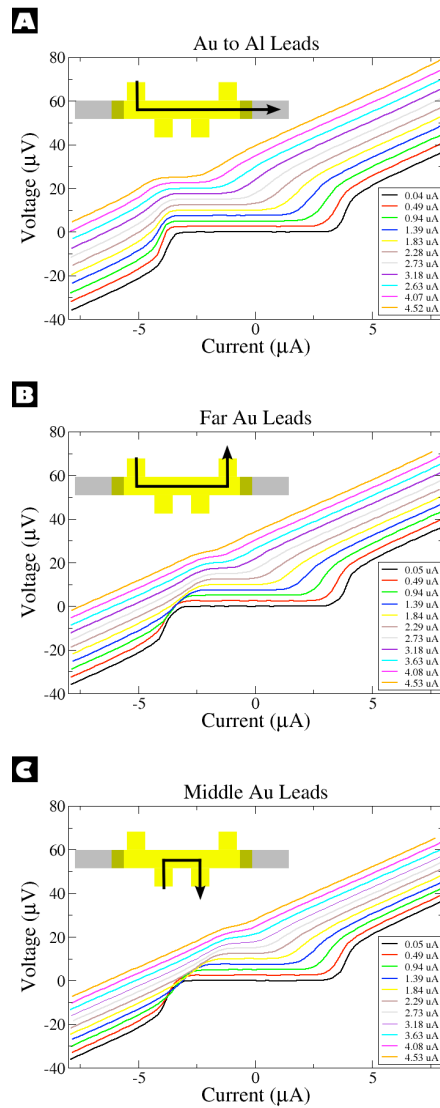


Figure 5.21. IV curves of the entire SNS wire with different additional DC currents injected into the wire. The measurement configuration is shown in Fig. 4.8. The curves are offset for clarity. **(A)** When current is injected along most of the length of the normal section, the bulk of it travels along the Josephson path leading to large shifts in the IV curves as the injection current is increased. **(B)** The offsets are reduced, but still large when the injection path is sent between the outside normal leads. **(C)** When the injected current is sent between the two middle leads, most of this current travels along the direct path, and the shifts in the IV curves are small.

length of the normal section, rather most of it flows along its leftmost segment. If we were to suppose that the quasiparticle current is most efficacious in suppressing the Josephson coupling when traversing the coupling's weakest point at the center of the normal section (e. g. due to heating), the configurations of (B) and (C) would show a greater suppression for a given injection current. However, using this reasoning, the suppression seen in (B) should be about half that of (C), while the data show it to be nearly equal.

An obvious mechanism for this suppression is the fact that the dissipationless Josephson current and dissipative quasiparticle current have to compete for use of the same electronic states within the normal metal. Increasing the quasiparticle current reduces the number of channels available for supercurrent conduction and lowers the critical current. Another version of this channel competition was used to alter the direction of the Josephson current in the dangling arm experiments [120, 121, 116]. These experiments exploited a corollary of the charge imbalance effect, namely that as the quasiparticle excitations become imbalanced, the states remaining to compose the condensate are also altered. It can be shown [122] that the transverse distribution function $f_-(E)$ of Section 2.3 is related not only to the charge imbalance, but to the behavior of the Josephson current in an SNS system. A nonequilibrium occupation of the quasiparticle states in the normal metal can lead to the Josephson current being suppressed and even reversing directions. It should be emphasized that this nonequilibrium quasiparticle distribution differs from the charge imbalance created in superconductors in that it is produced in normal metals which may be coupled to superconductors.

A nonequilibrium quasiparticle distribution can be established in normal metals by using the fact that charge carriers traveling along a normal wire shorter than the material's

coherence length l_ϕ are not fully equilibrated over the length of the wire. If the wire terminates at reservoirs with two different temperatures or chemical potentials the energy distribution in the wire will be a nonequilibrium mix of the two equilibrium reservoirs. This phenomenon was demonstrated directly by Pothier *et. al.* [109] who used tunnel probes to reveal a double-step Fermi distribution for a wire between two reservoirs at different chemical potentials. It is precisely this nonequilibrium distribution that is used in the dangling arm experiments to alter the character of the Josephson current.

These prior experiments lead to a question which is pertinent to understanding not only our SNS wire, but the nonlocal coherence experiments as well: When current is sent into or along our normal wires, is the quasiparticle distribution far from equilibrium? The wires attached to the normal section of the SNS junction are similar to the heating wires of the nonlocal coherence experiment in that after traversing a few μm they widen out to 500 nm. The length of the ~ 100 nm wide part of these wires is only 4 μm for the SNS experiment, while it is close to 8 μm for the heating wires of the nonlocal experiment, both lengths that are of the same order of magnitude as l_ϕ . The fact that when using an identical I_{NS} current path as the dangling arm experiments we do not observe the reversal in the Josephson current previously reported implies that the distribution in this wire is not highly nonequilibrium. As the narrow part of this wire and the others are $\lesssim l_\phi$, such a distribution would indicate that the 500 nm parts of these wires are not acting as true reservoirs. In this case, our heat flow model, which treated them as such, would have underestimated the magnitudes of the thermoelectric voltages, though their qualitative character would be unchanged.

The absence of an observed supercurrent reversal does not entirely rule out the possibility of nonequilibrium effects in our experiments. Particularly in the nonlocal coherence experiments, where the origin of the thermoelectric oscillations remains ill-understood, all possible contributing mechanisms should be considered. The apparent independence of the oscillations' polarity to the direction of the thermal gradients is an observation that is consistent with a theory attributing their origin to a nonequilibrium quasiparticle distribution in the normal section. We conclude by noting a certain symmetry between these oscillations and the dangling arm experiments. In these previous experiments quasiparticle voltages were used to alter the properties of the supercurrent. In our experiments a supercurrent is used to alter the properties of quasiparticle voltages.

CHAPTER 6

Conclusion and Future Directions

We have presented evidence in two different types of experiments for effects that occur when a superconductor is probed on its coherence length scale ξ_S . In the first set of experiments, involving linear or incoherent samples, current injected from one normal metal probe on a superconductor created a nonlocal voltage on a second probe placed a distance $\sim \xi_S$ from the first. This signal could be distinguished from the charge imbalance background through its temperature, current, and distance dependence. The sign of the signal and its decay length were consistent with recent theories of the EC and CAR processes [66, 67]. In the second set of experiments, thermoelectric oscillations were produced in a normal metal probe on a hybrid normal metal-superconductor interferometer. These oscillations could also be picked up on a nonlocal normal metal probe located $\sim \xi_S$ from the first. While the mechanism creating these oscillations is not well understood, the nonlocal signal was both phase coherent and rapidly attenuated on scales comparable to ξ_S , each properties consistent with EC and CAR.

The first set of experiments is similar to the previous work of Beckmann *et. al.* in working in the transparent contact regime with diffusive materials. His use of ferromagnetic probes has the advantage of potentially distinguishing EC from CAR. Our work has the advantage that the non-charge imbalance nonlocal signal is at least an order of magnitude larger when working with normal probes. It would be useful to try to combine the advantages of each set-up by employing ferromagnetic lines that can inject spin-polarized

current into paramagnetic normal probe contacts placed on a superconductor. Such an arrangement might help to minimize some of the potential complications, discussed in Section 5.1, that can occur when using ferromagnetic probes. An entirely different measurement approach to search for EC and CAR in a linear sample was proposed by G. Bignon *et. al.* [123], who considered monitoring current-current correlations between the two probes. Attempts to perform these noise measurements are underway.

The coherent loop experiments resulted in a number of questions, some of which can be answered empirically. First, is the implication that the thermal current direction is not determinative of the polarity of the oscillations correct? This question could be answered by returning to a measurement of Andreev interferometer thermopower in which the direction of the thermal gradient can be reversed. Second, is the magnitude and direction of the Josephson current determinative of the magnitude and polarity of the oscillations? This question could be answered by fabricating a sample where the supercurrent can be directly controlled with an external current source rather than a magnetic field. Fabrication of such samples in the Mesoscopic Group have already started. If there is convincing theoretical or experimental evidence that the thermoelectric oscillations are proportional to the Josephson currents, the nonlocal loop measurements show a method for observing persistent currents using only transport techniques. This method could be useful for examining the predicted crossover from $h/2e$ flux-periodic currents to h/e flux-periodic currents in hybrid normal metal-superconductor loops [103, 104].

Finally, there is the option of using other materials in searching for transport behavior due to EC and CAR. J. Cayssol [124] has recently suggested using graphene probes on a superconductor to search for such effects. Due to the novel band structure of graphene,

one may be able to isolate the two different processes by independently gating the probes, one to the hole side, one to the electron side. While the recent isolation of graphene has produced prodigious speculation on possible devices, such a proposal is not without merit.

References

- [1] P. G. de Gennes, *Superconductivity of Metals and Alloys* (Addison-Wesley, Redwood City, CA, 1966).
- [2] M. Tinkham, *Introduction to Superconductivity* (Second Edition, Dover, Mineola, NY, 1996).
- [3] J. B. Ketterson and S. N. Song, *Superconductivity* (Cambridge University, Cambridge, UK, 1999).
- [4] Y. Imry, *Introduction to Mesoscopic Physics* (Oxford University, Oxford, UK, 1997).
- [5] E. Akkermans and G. Montambaux, *Mesoscopic Physics of Electrons and Photons* (Cambridge University, Cambridge, UK, 2007).
- [6] H. Kamerlingh Onnes, *Leiden Comm.* **120b**, **122b**, **124c** (1911).
- [7] M. R. Schafroth, *Phys. Rev.* **100**, 463 (1955).
- [8] L. N. Cooper, *Origins of the Theory of Superconductivity*, (BCS@50 Conference, Urbana, IL, 2007).
- [9] L. N. Cooper, *Phys. Rev.* **104**, 1189 (1956).
- [10] J. Bardeen, L. N. Cooper, and J. R. Schrieffer, *Phys. Rev.* **106**, 162 (1957).
- [11] J. Bardeen, L. N. Cooper, and J. R. Schrieffer, *Phys. Rev.* **108**, 1175 (1957).
- [12] N. W. Ashcroft and N. D. Mermin, *Solid State Physics* (Sauders College, Philadelphia, 1976).
- [13] H. Courtois, P. Charlat, Ph. Gandit, D. Mailly, and B. Pannetier, *J. Low Temp. Phys.* **116**, 187 (1999).
- [14] A. F. Volkov and V. V. Pavlovskii, *Phys. Rev. B* **72**, 014529 (2005).

- [15] M. S. Crosser, J. Huang, F. Pierre, P. Virtanen, T. T. Heikkilä, F. K. Wilhelm, and N. O. Birge, *Phys. Rev. B* **77**, 014528 (2008).
- [16] J. Clarke, *Phys. Rev. Lett.* **28**, 1363 (1972).
- [17] M. Tinkham and J. Clarke, *Phys. Rev. Lett.* **28**, 1366 (1972).
- [18] M. L. Yu and J. E. Mercereau, *Phys. Rev. B* **12**, 4909 (1975).
- [19] G. J. Dolan and L. D. Jackel, *Phys. Rev. Lett.* **39**, 1628 (1977).
- [20] C. C. Chi and J. Clarke, *Phys. Rev. B* **19**, 4495 (1979).
- [21] T. Y. Hsiang and John Clarke, *Phys. Rev. B* **21**, 945 (1980).
- [22] D. J. Van Harlingen, *J. Low Temp. Phys.* **44**, 163 (1981).
- [23] T. R. Lemberger and J. Clarke, *Phys. Rev. B* **23**, 1088 (1981).
- [24] H. J. Mamin, J. Clarke and D. J. Van Harlingen, *Phys. Rev. B* **29**, 3881 (1984).
- [25] C.-J. Chien, Ph.D. Thesis, Northwestern University (1998).
- [26] C.-J. Chien and V. Chandrasekhar, *Phys. Rev. B* **60**, 3655 (1999).
- [27] A. Schmid and G. Schön, *J. Low Temp. Phys.* **20**, 207 (1975).
- [28] C. J. Pethick and H. Smith, *Ann. Phys. (N.Y.)* **119**, 133 (1979).
- [29] P. W. Anderson, in *Progress in Low Temperature Physics vol. 5*, edited by C. J. Gorter (Wiley, New York, 1967).
- [30] B. D. Josephson, *Phys. Lett.* **1**, 251 (1962).
- [31] P. W. Anderson and J. M. Rowell, *Phys. Rev. Lett.* **10**, 230 (1963).
- [32] D. J. Thouless, *Phys. Rev. Lett.* **39**, 1167 (1977).
- [33] A. A. Golubov, M. Y. Kupriyanov, and E. Il'ichev, *Rev. Mod. Phys.* **76**, 411 (2004).
- [34] M. Yu. Kupriyanov, and V. F. Lukichev, *Fiz. Nizk. Temp.* **8**, 1045 (1982) [*Sov. J. Low Temp. Phys.* **8**, 526 (1982)].
- [35] J. W. Wilkins, ch. 24 in *Tunneling Phenomena in Solids* (Plenum, New York, 1969).

- [36] A.F. Andreev, *Zh. Eksp. Teor. Fiz.* **46**, 1823 (1964) [*Sov. Phys. JETP* **19**, 1228 (1964)].
- [37] N. N. Bogoliubov, *Zh. Eksp. Teor. Fiz.* **34**, 58, 73 (1958); [*Sov. Phys. JETP* **7**, 41, 51 (1958)].
- [38] G. Deutscher and P. G. de Gennes, in *Superconductivity*, edited by R. D. Parks (Marcel Dekker, New York, 1969).
- [39] A. W. Kleinsasser, T. N. Jackson, D. McInturff, F. Rammo, G. D. Pettit, and J. M. Woodall, *Appl. Phys. Lett.* **57**, 1811 (1990).
- [40] A. Kastalsky, A. W. Kleinsasser, L. H. Greene, R. Bhat, F. P. Milliken, and J. P. Harbison, *Phys. Rev. Lett.* **67**, 1326 (1991).
- [41] B. J. van Wees, P. de Vries, P. Magnée, and T. M. Klapwijk, *Phys. Rev. Lett.* **69**, 510 (1992).
- [42] C. W. J. Beenakker, *Phys. Rev. B* **46**, 12841 (1992).
- [43] G. E. Blonder, M. Tinkham, and T. M. Klapwijk, *Phys. Rev. B* **25**, 4515 (1981).
- [44] A. A. Abrikosov, L.P. Gor'kov, and I. E. Dzyaloshinski, *Methods of Quantum Field Theory in Statistical Physics* (Dover, Mineola, 1963).
- [45] A. L. Fetter and J. D. Walecka *Quantum Theory of Many Particle Systems* (Dover, Mineola, 1971)
- [46] L. P. Gor'kov, *Zh. Eksp. Teor. Fiz.* **34**, 735 (1958); [*Sov. Phys. JETP* **7**, 505 (1958)].
- [47] L. V. Keldysh, *Zh. Eksp. Teor. Fiz.* **47**, 1515 (1964); [*Sov. Phys. JETP* **20**, 1018 (1965)].
- [48] T. Matsubara, *Prog. Theor. Phys.* **14**, 351 (1955).
- [49] N. B. Kopnin *Theory of Nonequilibrium Superconductivity* (Oxford University, Oxford, UK, 2001).
- [50] G. Eilenberger *Z. Phys.* **214**, 195 (1968).
- [51] K. D. Usadel *Phys. Rev. Lett.* **25**, 507 (1970).
- [52] J.M. Byers and M.E. Flatté, *Phys. Rev. Lett.* **74**, 306 (1995).

- [53] G. Deutscher and D. Feinberg, *Appl. Phys. Lett.* **76**, 487 (2000).
- [54] R. Mélin, *J. Phys.: Condens. Matter* **13**, 6445 (2001).
- [55] T. Yamashita, S. Takahashi, and S. Maekawa, *Phys. Rev. B* **68**, 174504 (2003).
- [56] D. Sanchez, R. Lopez, P. Samuelsson, and M. Buttiker, *Phys. Rev. B* **68**, 214501 (2003).
- [57] F. Giazotto, F. Taddei, R. Fazio, and F. Beltram, *Phys. Rev. Lett.* **97**, 087001 (2006).
- [58] G. Falci, D. Feinberg, and F. W. J. Hekking, *Europhys. Lett.* **54**, 255 (2001).
- [59] R. Mélin and D. Feinberg, *Eur. Phys. Jour. B* **26**, 101 (2002).
- [60] D. Feinberg, *Eur. Phys. Jour. B* **36**, 419 (2003).
- [61] N. M. Chtchelkatchev, *Zh. Eksp. Teor. Fiz.* **78**, 265 (2003); [*Sov. Phys. JETP* **78**, 230 (2003)].
- [62] D. Beckmann, H. B. Weber, and H. v. Löhneysen, *Phys. Rev. Lett.* **93**, 197003 (2004).
- [63] F. J. Jedema, A. T. Filip, and B. J. van Wees, *Nature* **410**, 345 (2001).
- [64] Y. Ji, A. Hoffmann, J. S. Jiang, and S. D. Bader, *Appl. Phys. Lett.* **85**, 6218 (2004).
- [65] S. Russo, M. Kroug, T. M. Klapwijk, and A. F. Morpurgo, *Phys. Rev. Lett.* **95**, 027002 (2005).
- [66] R. Mélin and D. Feinberg, *Phys. Rev. B* **70**, 174509 (2004).
- [67] J.P. Morten, A. Brataas, and W. Belzig, *Phys. Rev. B* **74**, 214510 (2006).
- [68] Y. V. Nazarov, *Phys. Rev. Lett.* **73**, 1420 (1994).
- [69] A. Levy Yeyati, F. S. Bergeret, A. Martín-Rodero, and T. M. Klapwijk, *Nature Physics* **3**, 455 (2007).
- [70] M. Stuivinga, J. E. Mooij, and T. M. Klapwijk, *Physica* **108B + C**, 1023 (1981).
- [71] C. Strunk, V. Bruyndoncx, C. Van Haesendonck, V. V. Moshchalkov, Y. Bruynseraede, C. J. Chien, B. Burk, and V. Chandrasekhar, *Phys. Rev. B* **57**, 10 854 (1998).

- [72] J. Eom, Ph.D. Thesis, Northwestern University (1998).
- [73] J. Aumentado, Ph.D. Thesis, Northwestern University (2000).
- [74] Z. Jiang, Ph.D. Thesis, Northwestern University (2005).
- [75] Z. Zhang, Ph.D. Thesis, Northwestern University (2006).
- [76] H.-S. Chang, J. P. Pon, K.-C. Hsieh, and C. C. Chen, *J. Electron. Mater.* **30**, 1171 (2001).
- [77] P. M. Berglund, H. K. Collan, G. J. Ehnholm, R. G. Gylling, and O. V. Lounasmaa, *J. Low Temp. Phys.* **6**, 357 (1972).
- [78] J. G. Adler and J. E. Jackson, *Rev. Sci. Inst.* **37**, 1049 (1966).
- [79] G. J. Strijkers, Y. Ji, F. Y. Yang, C. L. Chien, and J. M. Byers, *Phys. Rev. B* **63**, 104510 (2001).
- [80] R. J. Soulen, J. M. Byers, M. S. Osofsky, B. Nadgorny, T. Ambrose, S. F. Cheng, P. R. Broussard, C. T. Tanaka, J. Nowak, J. S. Moodera, A. Barry, and J. M. D. Coey, *Science* **282**, 85 (1998).
- [81] N. Poli, J. P. Morten, M. Urech, Arne Brataas, D. B. Haviland, and V. Korenivski, *Phys. Rev. Lett.* **100**, 136601 (2008).
- [82] F. S. Bergeret, A. F. Volkov, and K. B. Efetov, *Phys. Rev. Lett.* **86**, 4096 (2001).
- [83] Yu. V. Sharvin, *Zh. Eksp. Teor. Fiz.* **48**, 984 (1965) [*Sov. Phys. JETP* **27**, 655 (1965)].
- [84] H. le Sueur, P. Joyez, H. Pothier, C. Urbina, and D. Esteve, *Phys. Rev. Lett.* **100**, 197002 (2008).
- [85] B. I. Ivlev and N. B. Kopnin, *Adv. Phys.* **33**, 47 (1984).
- [86] Y. Aharonov and D. Bohm, *Phys. Rev.* **115**, 485 (1959).
- [87] R. A. Webb, S. Washburn, C. P. Umbach, and R. B. Laibowitz, *Phys. Rev. Lett.* **54**, 2696 (1985).
- [88] C. P. Umbach, P. Santhanam, C. van Haesendonck, and R. A. Webb, *Appl. Phys. Lett.* **50**, 1289 (1987).

- [89] N. E. Israeloff, F. Yu, and A. M. Goldman, *Phys. Rev. Lett.* **71**, 2130 (1993).
- [90] H. Nakano and H. Takayanagi, *Phys. Rev. B* **47**, 7986 (1993).
- [91] P. G. N. de Vegvar, T. A. Fulton, W. H. Mallison, and R. E. Miller, *Phys. Rev. Lett.* **73**, 1416 (1994).
- [92] G. Bergmann, *Phys. Rep.* **107**, 1 (1984).
- [93] B.L. Altshuler and A.G. Aronov, *Pis'ma Zh. Eksp. Teor. Fiz.* **33**, 515 (1981). [*JETP Lett.* **33**, 499 (1981).]
- [94] F. Pierre, A.B. Gougam, A. Anthore, H. Pothier, D. Esteve, and N.O. Birge, *Phys. Rev. B* **68**, 085413 (2003).
- [95] V. T. Petrashov, V. N. Antonov, P. Delsing, and T. Claeson, *Phys. Rev. Lett.* **74**, 5268 (1995).
- [96] W. Belzig, R. Shaikhaidarov, V. V. Petrashov, and Yu. V. Nazarov, *Phys. Rev. B* **66**, 220505(R) (2002).
- [97] J. Eom, C.-J. Chien, V. Chandrasekhar, *Phys. Rev. Lett.* **81**, 437 (1998).
- [98] D.A. Dikin, S. Jung, and V. Chandrasekhar, *Europhys. Lett.* **57**, 564 (2002).
- [99] Z. Jiang and V. Chandrasekhar, *Chinese J. Phys.* **43**, 693 (2005).
- [100] P. Cadden-Zimansky, Z. Jiang, and V. Chandrasekhar, *Physica E* **40**, 155 (2007).
- [101] A. Parsons, I. Sosnin, and V. T. Petrashov, *Phys. Rev. B* **67**, 140502 (2003).
- [102] A. Parsons, I. Sosnin, and V. T. Petrashov, *Physica E* **18**, 316 (2003).
- [103] M. Büttiker, T. M. and Klapwijk, *Phys. Rev. B* **33**, 5114 (1986).
- [104] J. Cayssol, T. Kontos, and G. Montambaux, *Phys. Rev. B* **67**, 184508 (2003).
- [105] E. M. Lifshitz and L. P. Pitaevskii, *Physical Kinetics* (Pergamon Press, Elmsford, NY, 1981).
- [106] K.E. Nagaev, *Phys. Rev. B* **52**, 4740 (1995).
- [107] M. Henny, H. Birk, R. Huber, C. Strunk, A. Bachtold, M. Krüger, and C. Schönenberger, *Appl. Phys. Lett.* **71**, 773 (1997).

- [108] W. H. Press, S. A. Teukolsky, W. T. Vetterling, and B. P. Flannery *Numerical recipes in C: The Art of Scientific Computing* (Second Edition, Cambridge University Press, Cambridge, UK, 1992).
- [109] H. Pothier, S. Gueron, N. O. Birge, D. Esteve, and M. H. Devoret, *Phys. Rev. Lett.* **79**, 3490 (1997).
- [110] R. Seviour and A. F. Volkov, *Phys. Rev. B* **62**, R6116 (2000).
- [111] V. R. Kogan, V. V. Pavlovskii, and A. F. Volkov, *Europhys. Lett.* **59**, 875 (2002).
- [112] T. T. Heikkilä, M. P. Stenberga, M. M. Salomaa, and C. J. Lambert, *Physica B* **284**, 1862 (2004).
- [113] P. Virtanen and T. T. Heikkilä, *Phys. Rev. Lett.* **92**, 177004 (2004).
- [114] P. Virtanen and T. T. Heikkilä, *J. Low Temp. Phys.* **136**, 401 (2004).
- [115] P. Virtanen and T. T. Heikkilä, *Appl. Phys. A* **89**, 625 (2007).
- [116] R. Shaikhaidarov, A. F. Volkov, H. Takayanagi, V. T. Petrashov, and P. Delsing, *Phys. Rev. B* **62**, R14649 (2000).
- [117] S. Guéron, Ph.D. Thesis, CEA-Saclay (1997).
- [118] P. Charlat, H. Courtois, Ph. Gandit, D. Mailly, A. F. Volkov, and B. Pannetier, *Phys. Rev. Lett.* **77**, 4950 (1996).
- [119] M. J. Black and V. Chandrasekhar, *Europhys. Lett.* **50**, 257 (2000).
- [120] J. J. A. Baselmans, A. F. Morpurgo, B. J. van Wees, and T. M. Klapwijk, *Nature* **397**, 43 (1999).
- [121] J. Huang, F. Pierre, T. T. Heikkilä, F. K. Wilhelm, and N. O. Birge, *Phys. Rev. B* **66**, 020507(R) (2002).
- [122] Frank K. Wilhelm, Gerd Schön, and Andrei D. Zaikin, *Phys. Rev. Lett.* **81**, 1682 (1998).
- [123] G. Bignon, M. Houzet, F. Pistolesi, and F. W. J. Hekking, *Europhys. Lett.* **67** 110 (2004).
- [124] J. Cayssol, *Phys. Rev. Lett.* **100**, 147001 (2008).